FACULTY OF ENGINEERING
AND ARCHITECTURE

mmWave-over-fiber Distributed Antenna Systems for Next-Generation Wireless Applications

Arno Moerman

Dissertation submitted to obtain the academic degree of
Doctor of Electrical Engineering

Supervisors
Prof. Sam Lemey, PhD
Prof. Patrick Van Torre, PhD

Department of Information Technology
Faculty of Engineering and Architecture, Ghent University

February 2025

GHENT
UNIVERSITY

Members of the Examination Board

Chair

Prof. Em. Daniel De Zutter, PhD	Ghent University

Other members entitled to vote

Prof. Jan Doutreloigne, PhD	Ghent University
Prof. Jeroen Famaey, PhD	Antwerp University
Prof. Ulf Johannsen, PhD	Eindhoven University of Technology
Prof. Hendrik Rogier, PhD	Ghent University

Supervisors

Prof. Sam Lemey, PhD	Ghent University
Prof. Patrick Van Torre, PhD	Ghent University

Dankwoord

Mijn ouders hebben me altijd geleerd om stevig met beide voeten op de grond te blijven staan. Een gouden raad die ik mijn hele leven trouw heb opgevolgd. Als *overachiever* kon ik het echter niet laten om dat stapje verder te gaan. In de afgelopen vijf en een half jaar heb ik niet alleen beide voeten op de grond gehouden, maar ben ik er ook een paar keer vol met mijn gezicht tegen geknald. Mijn doctoraatsthesis was een rollercoaster met pieken en dalen. De hoogtes waren dagen waarop ik een meting met simulatie vergeleek en die nagenoeg op elkaar lagen (en aan het einde van een doctoraatstraject maakt dit je dag, of zelfs je week). Een laagte was mijn eerste ontmoeting met *imposter syndrome*, die ik nét genoeg kon negeren zodat hij mij het volledige traject op de hielen zat. Toch kijk ik met dankbaarheid terug op deze jaren. Het is een unieke ervaring om de tijd, ruimte en steun te krijgen om onderzoek te doen, dagelijks omringd te zijn door knappe koppen en met hen (filosofische) discussies te voeren. Met de hand op het hart zou ik dan ook iedereen aanraden om, als de kans zich voordoet, een doctoraatsthesis met beide handen aan te grijpen. Neem misschien alleen een valhelm mee.

Hoewel ik spreek van *mijn* doctoraatsthesis, is onderzoek een *team effort*. Daardoor zou ik graag een heleboel mensen bedanken. Eerst en vooral mijn twee promotoren Sam en Patrick om mij dag in dag uit te ondersteunen waar nodig. Sam, bedankt om altijd klaar te staan wanneer ik (veel te laat) vraag iets na te kijken en om mee te denken bij nieuwe ideeën. Je hielp de focus te bewaren in mijn warhoofd wanneer nodig. Ik hoop dat ik geen al te grote lastpak was de voorbije jaren. Patrick, bedankt om jouw kennis te delen met mij. Ik denk dat er weinig mensen zijn met een kennis die zo breed rijkt als de uwe. Hoewel ik me er zelf niet aan durfde wagen, bracht je mij op de hoogte van de radio-amateur wereld, die mijn interesse in en blik op het toegepast electromagnetisme verder verruimde.

Verder zou ik ook graag Hendrik en Dries bedanken om tijdens de opleiding mijn interesse te wekken voor het vakgebied en om mij aan te nemen als doctoraatsstudent. Tijdens mijn doctoraat kon ik altijd bij jullie aankloppen om beroep te doen op jullie inzicht in het vakgebied.

Olivier, bedankt om avonden lang met mij in het labo te spenderen tijdens meetcampagnes, voor de vele gesprekken en om jouw kennis en passie voor

het labo en het vakgebied met mij te delen. Jij hebt een groot aandeel in mijn groei de afgelopen jaren. Martijn, bedankt om jouw nuchtere kijk te delen in de vele gesprekken 's ochtends en om mij als 'peter' op de werkvloer wegwijs te maken in het kluwen van de administratie en printers. *Kamil, thank you for inspiring me with your unwavering dedication for the craft. It motivated me throughout the past years.* Ik wens jullie alle drie een succesvolle carrière toe.

De afgelopen jaren heb ik ook mensen ontmoet waar ik altijd nét iets meer kon op rekenen. Bedankt Joryan om af en toe samen alles te relativeren. Laat me gerust weten wanneer je nog eens samen naar Graspop wilt. Bedankt Laura om altijd helemaal jezelf te zijn en jouw enthousiasme op de groep over te brengen. Mijn *partners in crime*, Dennis en Nicolas, zou ik graag bedanken voor de vele babbels en leuke momenten tijdens onze studentenjaren, in het thesislokaal en later in onze bureaus.

Als vreemde eend in de bijt en grootste stoorzender van onze bureau wil ik me graag excuseren tegenover Emile, Jul, Maxim, Tim en Nathan. Bij deze wil ik jullie allemaal bedanken om een trage werkdag sneller te doen verlopen en terloops vergeef ik jullie alle *side-eyes* wanneer ik een vergadering vanuit de bureau deed. De laatste tijd werd ik tijdens de lunchpauzes door de huidige inwoners van het andere bureau afgeschilderd als de cynische collega die enkel grove opmerkingen kon maken. Om de daad bij het woord te voegen speelde ik daarom eventjes met het idee om een *roast* te schrijven voor jullie. Niet veel later liet ik dit idee weer varen omdat ik het mezelf niet té makkelijk wou maken. Bedankt Jelle, Bramuel (Bram & Samuel), Victor, Ruben, Sofie, Sander en Arne voor de vele babbels en ik wens jullie alle succes toe met het afronden van jullie doctoraat. Hopelijk kijken jullie later even positief terug naar deze periode als mij. In een omgeving waar alle collega's komen en gaan, zou ik ook graag Gert-Jan, Dries, Pieter, Duygu, Seppe en Igor willen bedanken voor hun inspirerende voorbeeld, hun behulpzaamheid en de aangename sfeer op verdieping +11 door te geven.

Daarnaast zijn er enkele mensen die niet per se onder de eerder genoemde groepen vallen, maar die zonder twijfel een waardevolle bijdrage hebben geleverd aan dit werk en mijn groei. Laurens Bogaert, bedankt voor het leggen van de basis van dit onderzoek en voor je bereidheid om steeds mijn vragen te beantwoorden. Joris Van Kerrebrouck, dankjewel voor alle hulp en om mij de nodige kennis en inzichten bij te brengen. Ook een welgemeende dank aan iedereen die ik tijdens verschillende projecten heb mogen ontmoeten. Bjorn, Frederick, de andere *Smart Diapers*-partners, Tinus, Cédric, Tom, Margot, Ewoud en Bart – dankjewel voor de fijne samenwerking en voor het verbreden

van mijn kennis in domeinen waarmee ik minder vertrouwd was. *Last, but certainly not least*, bedankt Sabrina voor de sporadische ochtendgesprekken om 6u30 en om de werkomgeving werkbaar te houden – geen eenvoudige taak met 'ordelijke' mensen zoals mij in de buurt.

Ik was natuurlijk niet 24/7 aan mijn bureau of in het labo te vinden. Voor alle broodnodige momenten van ontspanning de afgelopen jaren, zou ik graag de ruime vriendengroep bedanken. Grote kans dat je hierbij hoort als we de afgelopen jaren samen een aperitief hebben gedronken of samen naar een concert zijn geweest. Ik ga me niet verbranden door een reeks namen te noemen, waarvan ik er zeker enkele zou vergeten. Jullie weten wie jullie zijn en jullie kunnen ook altijd op mij rekenen.

Mijn doctoraat werd natuurlijk ook overschaduwd door de COVID-periode en hier zou ik graag Dirk, Ingrid en Florian bedanken om mij vijf jaar geleden tijdens de eerste golf in huis te nemen zodat Elisa en ik elkaar konden blijven zien. Ik besef dat het geen evidentie is om een schoonzoon/-broer in huis te nemen. Bedankt hiervoor en voor alle steun. PS: Florian, ik ging hier eerst mijn excuses aanbieden om al jouw eten op te eten in die periode, maar misschien moet jij mij wel bedanken en ben ik de reden waarom je momenteel zo scherp staat.

Mama en papa, bedankt om een veilige en ruimdenkende thuisomgeving te creëren voor Eva en mezelf. Weinig mensen doen het jullie na om zo hard te werken om ons alle kansen te geven die we wensten. Ik ben hiervoor tegelijk ontzettend dankbaar en trots op jullie. Bedankt meme om ons talloze weekenden en schoolvakanties op te vangen en voor de vele borden kip-kaashamburgers met rode bieten. Bedankt Eva voor alle steun, je bent niet alleen een top-zus, maar ook een top-meter voor Julien. Hoewel ik als grote broer jou het voorbeeld zou moeten geven, kan ik nog veel van jou leren.

Woorden schieten te kort voor het makkelijkste deel uit mijn dankwoord. Bedankt Elisa om mij altijd voor de volle 100 % te steunen in alles wat ik doe. Jij bent de grootste reden dat ik hier vandaag sta. Lieve, kleine Julien, hoewel je het zwoegen de voorbije jaren niet meemaakte, helpte je des te meer bij de laatste loodjes. Jouw kleine glimlachjes veranderden mijn kijk op het leven en gaven me de laatste, nodige duwtjes in de rug om dit proefschrift af te werken. Ik zie jullie graag en ik kijk uit naar het fantastische leven dat ons tegemoet komt.

Deinze, 14 februari 2025
Arno Moerman

I need to be myself because it's so lonely in the eyes of someone else.

Stick To Your Guns - Diamond

Contents

Samenvatting

De volgende generatie draadloze netwerken staat op het punt om het internet der alles (Engels: *Internet of Everything*, IoE) te ondersteunen. Het is een paradigma dat een sterk verbonden wereld voor ogen heeft waarin een veelheid van mensen, apparaten en systemen naadloos met elkaar communiceren. De netwerken die dit zullen verwezenlijken moeten verschillende gebruikers gelijktijdig voorzien van datasnelheden van verschillende gigabits per seconde (Gbps). Dit alles terwijl er strikte vereisten zijn voor de betrouwbaarheid van de draadloze connectie en de vertraging die deze met zich meebrengt. Het doel van IoE is om een datageoriënteerde samenleving te bevorderen, waarmee revolutionaire toepassingen zoals de integratie van aangevulde realiteit (Engels: *augmented reality*, AR) en virtuele werkelijkheid (Engels: *virtual reality*, VR) in het dagelijks leven mogelijk worden gemaakt. Daarnaast streeft IoE er ook naar om uitgebreide realiteit (Engels: *extended reality*, XR) te verwezenlijken. Hier worden multizintuiglijke elementen geïntegreerd om innovaties zoals holografische aanwezigheid, robotchirurgie op afstand en slimme fabrieken mogelijk te maken.

Om het volledige potentieel van de vijfde generatie (Engels: *fifth-generation*, 5G) netwerk te benutten en de weg vrij te maken voor technologieën voorbij 5G (Engels: *beyond 5G*, B5G) zijn essentiële innovatieve doorbraken nodig. Een van de belangrijkste daarvan is het gebruik van nieuwe, ongebruikte frequentiebanden zoals de 5G FR2 frequentiebanden (24.25 GHz–71 GHz) en de andere millimetergolf (Engels: *millimeterwave*, mmWave) banden (30 GHz–300 GHz) om toegang te krijgen tot een overvloed aan bandbreedte. Naast dit nieuwe spectrum is de grootschalige uitrol van gedistribueerde meerdere in, meerdere uit (Engels: *distributed multiple-input mulitple-output*, DMIMO) draadloze systemen van cruciaal belang om de betrouwbaarheid en doorvoersnelheid van draadloze netwerken te verbeteren. Dit staat tegenover de huidige trend van celverdichting, die zijn limiet heeft bereikt qua doorvoersnelheid en interferentie tussen gebruikers.

Dit proefschrift overbrugt de kloof tussen de overvloed aan theoretische studies over celloze MIMO en DMIMO, waarin de gunstige communicatie- en radareigenschappen van deze systemen worden belicht, en het gebrek aan praktisch geïmplementeerde millimetergolf DMIMO-systemen.

Hoofdstuk 2 stelt het eerste realistische millimetergolf-over-glasvezeltechnologie gedistribueerd antennesysteem (Engels: *distributed antenna system*, DAS) voor dat in staat is om razendsnelle datasnelheden te leveren en daarmee de weg vrijmaakt voor de grootschalige uitrol van gedistribueerde millimetergolf draadloze communicatiesystemen in realistische omgevingen. Het DAS maakt gebruik van een fotonisch ondersteunde architectuur bestaande uit een centraal hoofdkantoor (Engels: *central office*, CO) en meerdere gedistribueerde antenne-eenheden (Engels: *remote antenna unit*, RAU). De RAU's zijn verwezenlijkt met behulp van luchtgevulde substraatgeïntegreerde golfgeleidertechnologie (Engels: *air-filled substrate-integrated-waveguide*, AFSIW) dewelke kosteneffectieve en efficiënte grootschalige implementaties mogelijk maakt. Een enkele optische vezel ondersteunt zowel uplink- als downlinkcommunicatie via een half-duplex methode waardoor een laser in de RAU overbodig wordt en de totale architectuur verder wordt vereenvoudigd. De inherente frequentiesynchronisatie van de millimetergolf-over-glasvezel architectuur maakt de ondersteuning van DMIMO mogelijk om de betrouwbaarheid verder te verhogen en draadloze datasnelheden te verbeteren. Om deze bevindingen te staven zijn experimenten uitgevoerd, in zowel een anechoïsche kamer als in een realistische, industriële omgeving. Het distribueren van vier RAU's in de omgeving van de gebruikersapparatuur (Engels: *user equipment*, UE) en vier antennes op het robotintegratieplatform lost alle blokkageproblemen op door over te schakelen naar het RAU-UE antennepaar met de beste verbinding, wat een datasnelheid van 24 Gbps garandeert. Met behulp van DMIMO kan het voorgestelde systeem datasnelheden tot 48 Gbps ondersteunen tussen het CO en de UE via twee actieve RAU's en vier UE antennes in een realistische industriële omgeving.

Hoofdstuk 3 richt zich op de mogelijkheden van een enkele mmWave draadloze verbinding over glasvezel tussen het CO en de UE om de signaalkwaliteit te verbeteren door gebruik te maken van *Selection Combining* (SC) en *Maximum Ratio Combining* (MRC) technieken in overdrachtsgebieden, waar de signaalverbinding tot een van de eindgebruiker antennes wegvalt door zelfblokkering tijdens rotatie. Door middel van systeemanalyse wordt de totale doorvoersnelheid geoptimaliseerd in deze overgangsgebieden binnen een anechoïsche kamer, waarbij een datasnelheid van 24 Gbps wordt bereikt met een symboolsnelheid van 6 Gbaud, gebruikmakend van kwadratuur-amplitudemodulatie (Engels: *quadrature amplitude modulation*, QAM) schema's. De verdeling van vier antennes op de UE verbetert de betrouwbaarheid en robuustheid tegen zelfblokkage aanzienlijk. Door

gebruik te maken van SC, waarbij het systeem overschakelt naar het UE-antennepaar met de beste signaalkwaliteit, worden zelfblokkageproblemen geminimaliseerd tijdens een rotatie van de eindgebruiker met 360 graden, behalve in overdrachtsgebieden waar de signaalkwaliteit afneemt. Indien de signalen van alle UE-antennes optimaal worden gecombineerd in MRC, worden aanzienlijke verbeteringen in signaalkwaliteit bereikt in overdrachtsgebieden, wat het probleem van zelfblokkering oplost.

Hoofdstuk 4 presenteert een simulatieraamwerk dat is ontworpen om de nauwkeurige optimalisatie van millimetergolf-over-glasvezelgebaseerde gedistribueerde antennesystemen te vereenvoudigen en versnellen. Dit omdat het opzetten van praktische millimetergolf draadloze verbindingen over glasvezel behoorlijk tijdsintensief kunnen zijn. Dit raamwerk integreert verschillende commerciële softwarepakketten met zelfontwikkelde code, waarbij rekening wordt gehouden met imperfecties van realistische actieve componenten (niet-lineaire signaalvervormingen, ruis, frequentieafhankelijke versterking), antennesystemen (vermogenreflecties, frequentieafhankelijke versterking), optische componenten (niet-lineaire signaalvervormingen, ruis, frequentieafhankelijke versterking) en propagatiekanalen. De geldigheid van het raamwerk wordt bevestigd door verschillende meetcampagnes die een goede overeenstemming aantonen tussen gesimuleerde en gemeten signaalkwaliteit en aantonen dat de elektrische, opto-elektrische en optische componenten goed gemodelleerd zijn en efficiënt met elkaar samenwerken. Daarnaast voorspelt de simulatiesuite nauwkeurig de signaalkwaliteit op verschillende UE-posities, dewelke goed overeenkomt met metingen in een anechoïsche omgeving. Bovendien kunnen andere kanaalmodellen in het pakket worden opgenomen. Dit wordt geïllustreerd door een opstelling in een half-anechoïsche omgeving, waarbij gebruik wordt gemaakt van een analytisch twee-straal kanaalmodel om de signaalkwaliteit met hoge nauwkeurigheid te simuleren. Tot slot is het raamwerk in staat om de impact van interferentie tussen gebruikers te analyseren in een scenario met meerdere gelijktijdige gebruikers, waarbij verschillende UE's worden bediend door dezelfde RAU met meerdere stralingsbundels. De praktische implementatie wordt gerealiseerd met behulp van een Butlermatrix en de metingen voorspellen correct de interferentie tussen gebruikers.

Hoofdstuk 5 onderzoekt het potentieel van gedistribueerde antennesystemen om te gebruiken voor interactieve AR- en VR-toepassingen waarbij UE's op het hoofd worden gemonteerd en benadert dit vanuit een bio-elektromagnetisch perspectief. Dit houdt in dat de achtergrondstraling van een gedistribueerde antennesysteem zal bekeken worden en dat

de geabsorbeerde elektromagnetische velden zullen bestudeerd worden van millimetergolfantennes die dicht bij het menselijk lichaam worden geplaatst. Het gebruik in deze toepassing blijkt ook uitdagend vanuit een communicatieperspectief door het aantal bewingsvrijheidsgraden van het lichaam. Door middel van een literatuuronderzoek wordt eerst de ernst van blokkageverlies in mmWave draadloze verbindingen onderzocht wanneer één of meer menselijke blokkades het zichtlijnpad belemmeren in een binnenomgeving. Er wordt vastgesteld dat het extra blokkageverlies kan oplopen tot 40 dB. Gedistribueerde antennesystemen lossen deze hoge blokkageverliezen op door altijd een zichtlijnpad over te houden tot een gebruikersantenne. Bij het inzetten van gedistribueerde systemen blijkt dat ze een lage achtergrondblootstelling behouden, terwijl hun hotspots veel compacter zijn ten opzichte van traditionele bij elkaar geplaatste MIMO-roosters. Vervolgens worden gedistribueerde antennesystemen die DMIMO implementeren ook vergeleken met andere opkomende technologieën, zoals herconfigureerbare intelligente oppervlakken (Engels: *reconfigurable intelligent surfaces*, RIS) en grote intelligente oppervlakken (Engels: *large intelligent surfaces*, LIS) wat betreft blootstelling en signaalkwaliteit. Met hun gunstige blootstellingsomstandigheden en hun superieure spectrale efficiëntie worden hogere datasnelheden en een efficiënter energiegebruik gerealiseerd. Ze verminderen ook de aanzienlijke blokkageverliezen die optreden bij millimetergolffrequenties door obstakels en andere omgevingsfactoren. Daarnaast worden twee AFSIW millimetergolf antennetopologieën vergeleken met een patchantenne en een dipoolantenne vanuit zowel een bio-elektromagnetisch als systeemontwerpperspectief. Dit leidt tot het voorstel van een nieuwe metriek die deze criteria met elkaar verbindt. AFSIW-topologieën worden geïdentificeerd als het meest voordelig doordat ze een hoge platformonafhankelijkheid en lage geabsorbeerde vermogensdichtheid (Engels: *absorbed power density*) bieden bij werking nabij het menselijk lichaam. Daarbovenop bieden ze ook aanzienlijke voordelen vanuit een antennesysteem perspectief bij de realisatie van antenneroosters. Tot slot worden metingen uitgevoerd in een anechoïsche omgeving met behulp van een antropomorf hoofdmodel dat is uitgerust met een op het hoofd gemonteerde UE om XR-toepassingsscenario's te simuleren. Het gebruik van gedistribueerde antennesystemen in combinatie met AFSIW-antennetopologieën maakt de implementatie mogelijk van een draadloos communicatiesysteem met hoge datasnelheid met een doorvoer van 12 Gbps in de n257-frequentieband (26.5 GHz–29.5 GHz) onder volledige beweging van het hoofd van de eindgebruiker. Ruimtelijke diversiteit zorgt voor betrouwbare signaalkwaliteit wanneer de gebruiker draait, terwijl de

implementatie van polarisatiediversiteit zorgt voor robuuste prestaties bij het kantelen van het hoofd.

Summary

The next generation of wireless networks is poised to support the Internet of Everything (IoE), a paradigm that envisions a highly interconnected world where a multitude of devices and systems communicate seamlessly. These networks must meet the demands of simultaneous multi-Gbps data speeds while adhering to stringent requirements for reliability and latency. IoE aims to foster a data-centric society, enabling revolutionary applications such as the integration of augmented reality (AR) and virtual reality (VR) into daily life. Furthermore, IoE aspires to realize extended reality (XR), which will incorporate multi-sensory elements to facilitate innovations such as holographic telepresence, remote surgery, and smart factories within the Industry 5.0 evolution.

To fully realize the potential of fifth-generation (5G) networks and pave the way for beyond-5G (B5G) technologies, key-enabling innovations are required. Foremost among these is the utilization of new, unoccupied spectrum bands, such as the 5G New Radio FR2 frequency bands (24.25 GHz–71 GHz) and the other millimeter-wave (mmWave) bands (30 GHz–300 GHz), to access abundant bandwidth. Alongside this new spectrum, the widespread deployment of distributed multiple-input multiple-output (DMIMO) or cell-free massive MIMO wireless systems is critical for enhancing wireless reliability and throughput, breaking away from the current trend of cell densification, which has reached its limit in terms of throughput and inter-user interference.

This PhD dissertation bridges the gap between the abundance of theoretical studies on cell-free MIMO and DMIMO, highlighting the beneficial communication and sensing properties of these systems, and the scarcity of practically implemented millimeter-wave DMIMO systems.

Chapter 2 proposes the first realistic mmWave-over-fiber distributed antenna system (DAS) capable of delivering multi-Gbps data rates, thereby paving the way towards deploying a wireless communication system for mass adoption in real-world environments. This DAS employs a photonically enabled architecture comprising a central office (CO) and multiple distributed remote antenna units (RAUs). The RAUs are constructed using air-filled substrate-integrated-waveguide (AFSIW) technology, facilitating cost-effective

and efficient large-scale deployments. A single optical fiber supports both uplink and downlink communication via a time-division duplex (TDD) method, eliminating the need for a laser in the RAU and thereby further simplifying the overall architecture. The inherent frequency synchronization of the mmWave-over-fiber architecture enables the support of DMIMO to further enhance reliability and boost wireless data rates. Experiments were conducted both in an anechoic chamber and in a realistic Industry 5.0 environment. Distributing four RAUs in the UE's environment and four antennas on the robotic integration platform mitigates all blockage issues by switching to the RAU-UE antenna pair with the best link, ensuring a data throughput of 24 Gbps. When deployed in the industrial scene, the mmWave DAS establishes a 48 Gbps link between the CO and user equipment (UE) across two active RAUs and four UE antennas using DMIMO.

Chapter 3 focuses on the capabilities of a single mmWave fiber-wireless link between the CO and UE to improve signal quality in the handover regions. Through system-level analysis, the total throughput of a single fiber-wireless link is optimized within an anechoic chamber, achieving a data rate of 24 Gbps with a symbol rate of 6 GBaud using quadrature amplitude modulation schemes (QAM). The distribution of four antennas on the UE significantly enhances reliability and robustness against self-blockage. By employing selection combining (SC), where the system switches to the UE antenna with the best link quality, self-blockage issues are mitigated over a 360-degree rotation, except within handover regions where signal quality declines. Alternatively, by using Maximum Ratio Combining (MRC), which optimally combines signals from all UE antennas, substantial improvements in link quality are achieved within handover regions, both in anechoic and realistic Industry 5.0 settings.

Chapter 4 presents a system-level framework designed to facilitate accurate and time-efficient optimization of mmWave-over-fiber distributed antenna systems since setting up practical mmWave fiber-wireless links is quite effortful. This framework integrates several commercial software packages with in-house developed code, accounting for imperfections of realistic active components (non-linear distortion, noise, frequency-dependent gain), antenna system (mismatches, frequency-dependent gain), optical components (non-linear distortion, noise, frequency-dependent gain), and propagation channel. The framework's validity is confirmed by various measurement campaigns, yielding good agreement between simulated and measured signal quality and demonstrating that the electrical, opto-electrical, and optical components are well-modeled and interact effectively. Additionally, the simulation suite

accurately predicts the signal quality at different UE positions, aligning well with measurements in an anechoic environment. Moreover, other channel models can be incorporated into the suite. This is illustrated by a half-anechoic environment set-up, using an analytical two-ray channel model to simulate the signal quality with high fidelity. Finally, the framework is able to analyze the impact of inter-user interference in a multi-user scenario, where different UEs are served by the same multi-beam front end. The practical implementation is realized using a Butler matrix, and the measurements successfully predict the inter-user interference.

Chapter 5 examines the deployment of distributed antenna systems from a bio-electromagnetic perspective, particularly for interactive AR and VR applications involving head-mounted UEs. This work expands on the first two chapters as a head-mounted device on a human user has more freedom in direction in its movements as it can also tilt on top of turning. A concise literature review is conducted to assess the severity of blockage loss in indoor mmWave wireless links when one or more human blockers obstruct the line-of-sight path. It is found that excess blockage loss can surge to 30 dB. When deploying distributed systems, it is found that they maintain low background exposure while their hotspots are much more confined when compared to more traditional co-located MIMO arrays. Subsequently, distributed antenna systems implementing DMIMO are also compared with other emerging technologies, such as reconfigurable intelligent surfaces (RIS) and large intelligent surfaces (LIS), in terms of exposure and link quality. With their favorable exposure conditions while offering superior spectral efficiency, higher data rates, and more efficient energy usage is achieved. They also mitigate the significant blockage losses that occur at mmWave frequencies due to obstacles and other environmental factors. Furthermore, two AFSIW mmWave antenna topologies are compared with an inset-fed patch and a dipole antenna from both a bio-electromagnetic and system design perspective, leading to the proposal of a new metric that links these criteria. AFSIW topologies are identified as the most advantageous, offering high platform independence and low absorbed power density when operating near the human body, while also providing significant advantages from an antenna system engineering perspective, particularly in the realization of antenna arrays. Finally, measurements are conducted in an anechoic environment using an anthropomorphic head phantom equipped with a head-mounted UE to simulate XR application scenarios. The use of distributed antenna systems in combination with AFSIW antenna topologies enables the establishment of a high-data-rate wireless communication system with a throughput of 12 Gbps

in the n257 frequency band (26.5 GHz–29.5 GHz) under full movement of the HMD. Spatial diversity ensures reliable link quality when the user turns, while the deployment of polarization diversity ensures robust performance when tilting the head.

List of Publications

Articles in international journals

- **A. Moerman**, J. Van Kerrebrouck, O. Caytan, I. Lima de Paula, L. Bogaert, G. Torfs, P. Demeester, H. Rogier, and S. Lemey, "Beyond 5G Without Obstacles: mmWave-over-Fiber Distributed Antenna Systems", *IEEE Communications Magazine*, vol. 60, no. 1, pp. 27–33, 2022
- I. Lima de Paula, L. Bogaert, O. Caytan, J. Van Kerrebrouck, **A. Moerman**, M. Muneeb, Q. Van den Brande, G. Torfs, J. Bauwelinck, H. Rogier, P. Demeester, G. Roelkens, and S. Lemey, "Air-Filled SIW Remote Antenna Unit With True Time Delay Optical Beamforming for mmWave-Over-Fiber Systems", *Journal of Lightwave Technology*, vol. 40, no. 20, pp. 6961–6975, 2022
- L. Van Messem, **A. Moerman**, O. Caytan, I. Lima de Paula, B. Hoflack, B. Stroobandt, S. Lemey, M. Moeneclaey, and H. Rogier, "A 4 × 4 Millimeterwave-Frequency Butler Matrix in Grounded Co-Planar Waveguide Technology for Compact Integration With 5G Antenna Arrays", *IEEE Transactions on Microwave Theory and Techniques*, vol. 71, no. 1, pp. 122–134, 2023
- **A. Moerman**, O. Caytan, L. Van Messem, J. Van Kerrebrouck, G. Torfs, P. Demeester, H. Rogier, and S. Lemey, "System-Level Simulation Suite for the Design of mmWave-Over-Fiber-Based Distributed Antenna Systems", *IEEE Transactions on Microwave Theory and Techniques*, vol. 71, no. 12, pp. 5082–5094, 2023
- T. Vanackere, T. Vandekerckhove, L. Bogaert, M. Billet, S. Poelman, S. Cuyvers., J. Van Kerrebrouck, **A. Moerman**, O. Caytan, N. Singh, S. Lemey, G. Torfs, P. Ossieur, G. Roelkens, S. Clemmen, and B. Kuyken, "Heterogeneous Integration of a High-Speed Lithium Niobate Modulator on Silicon Nitride Using Micro-Transfer Printing", *APL Photonics*, vol. 8, no. 8, p. 086 102, Aug. 2023
- L. Van Messem, **A. Moerman**, O. Caytan, H. Rogier, and S. Lemey, "Compact Self-Shielding Components for Beamforming Networks

Implemented in Substrate Integrated Coaxial Line Technology", *IEEE Transactions on Components, Packaging and Manufacturing Technology*, pp. 1–1, 2024

- J. Sennesael, **A. Moerman**, F. Bossuyt, B. Vandecasteele, C. Raepsaet, D. Beeckman, H. Rogier, and P. Van Torre, "An Environmentally Friendly Carbon-Printed Contactless Smart Diaper", pp. 1–1, 2024

- **A. Moerman**, O. Caytan, H. Rogier, and S. Lemey, "mmWave Distributed Antenna Systems for Interactive VR: Resolving Blockage Loss, Reducing Exposure, Antenna System Design", in *Antennas & Propagation Magazine: Bioelectromagnetics column*, submitted August 2024

Articles in conference proceedings

- L. Van Messem, **A. Moerman**, O. Caytan, I. Lima De Paula, B. Hoflack, B. Stroobandt, S. Lemey, and H. Rogier, "Substrate Integrated Components for Passive Millimeterwave-Frequency Beamforming Networks", in *2021 IEEE MTT-S International Microwave Workshop Series on Advanced Materials and Processes for RF and THz Applications (IMWS-AMP)*, 2021, pp. 272–274

- M. Huynen, D. Bosman, **A. Moerman**, and D. Vande Ginste, "Accurate Characterization of Radiation from Interconnects on Interposer at mmWave Frequencies", in *2022 IEEE 26th Workshop on Signal and Power Integrity (SPI)*, 2022, pp. 1–4

- **A. Moerman**, J. Van Kerrebrouck, O. Caytan, I. Lima de Paula, L. Bogaert, G. Torfs, P. Demeester, M. Moeneclaey, H. Rogier, and S. Lemey, "mmWave-over-Fiber Distributed Antenna Systems for Reliable multi-Gbps Wireless Communication", in *2022 3rd URSI Atlantic and Asia Pacific Radio Science Meeting (AT-AP-RASC)*, 2022, pp. 1–4

- **A. Moerman**, O. Caytan, L. Van Messem, I. Lima de Paula, J. Van Kerrebrouck, G. Torfs, P. Demeester, H. Rogier, and S. Lemey, "System-Level Model for mmWave-over-Fiber Distributed Antenna Systems", in *2022 IEEE International Symposium on Phased Array Systems & Technology (PAST)*, 2022, pp. 1–4

- L. Van Messem, **A. Moerman**, O. Caytan, H. Rogier, and S. Lemey, "Substrate Integrated Coaxial Line Millimeterwave Components Manufactured in Standard PCB", in *2023 IEEE 32nd Conference on Electrical Performance of Electronic Packaging and Systems (EPEPS)*, 2023, pp. 1–3

- O. Caytan, I. Lima De Paula, L. Bogaert, J. Van Kerrebrouck, **A. Moerman**, M. Muneeb, G. Torfs, J. Bauwelinck, P. Demeester, G. Roelkens, S. Lemey, and H. Rogier, "Co-Design Strategies for AFSIW-Based Remote Antenna Units for RFoF", in *2023 17th European Conference on Antennas and Propagation (EuCAP)*, 2023, pp. 1–5

- T. Vanackere, T. Vandekerckhove, L. Bogaert, M. Billet, S. Poelman, S. Cuyvers, J. Van Kerrebrouck, **A. Moerman**, O. Caytan, S. Lemey, G. Torfs, G. Roelkens, S. Clemmen, and B. Kuyken, "High-Speed Lithium Niobate Modulator on Silicon Nitride using Micro-Transfer Printing", in *CLEO 2023*, Optica Publishing Group, 2023, STh1R.1

- O. Caytan, **A. Moerman**, L. Van Messem, K. Yavuz Kapusuz, B. Hoflack, I. Lima de Paula, J. Van Kerrebrouck, G. Torfs, P. Demeester, S. Lemey, and H. Rogier, "Cost-Effective and Power-Efficient Beamforming Remote Antenna Units for Millimeterwave Distributed Antenna Systems", in *2023 XXXVth General Assembly and Scientific Symposium of the International Union of Radio Science (URSI GASS)*, 2023, pp. 1–4

- L. Van Messem, **A. Moerman**, O. Caytan, D. V. Ginste, H. Rogier, and S. Lemey, "Packaged Cost-Effective Millimeterwave Air-Filled SIW Components for Array Feed Networks", in *2023 IEEE Electrical Design of Advanced Packaging and Systems (EDAPS)*, 2023, pp. 1–3

- R. Wydaeghe, **A. Moerman**, O. Caytan, S. Shikhantsov, E. Tanghe, G. Vermeeren, H. Rogier, S. Lemey, P. Demeester, and W. Joseph, "New Hybrid Ray-Tracing/FDTD for EMF Exposure in 6G Networks Using Semantically Classified Google Earth Photogrammetry with Measurement Validation", in *2024 EUCAP*, accepted, not published yet

- T. Pattyn, **A. Moerman**, M. Huynen, and D. Vande Ginste, "Differential Interconnects with Integrated Equalization and Common-Mode Filtering for Broadband Signal Integrity Enhancement in High-Speed PAM-4 Signaling", in *2024 IEEE 28th Workshop on Signal and Power Integrity (SPI)*, 2024, pp. 1–4

- S. Shikhantsov, O. Caytan, **A. Moerman**, G. Torfs, P. Demeester, L. Martens, and W. Joseph, “Design, Construction and Evaluation of a Non-Metallic Numerically-Controlled Cartesian Positioning Platform for Low-Interference EMF Measurements in 6G and Beyond”, in *2024 IEEE INC-USNC-URSI Radio Science Meeting (Joint with AP-S Symposium)*, 2024, pp. 351–351
- J. Sennesael, **A. Moerman**, H. Rogier, and P. Van Torre, “Carbon-Ink Sensing Patterns for a Contactless Smart Diaper System”, in *2024 IEEE International Conference on Flexible and Printable Sensors and Systems (FLEPS)*, 2024, pp. 1–4

Patents filed

- P. Van Torre and **A. Moerman**, "System Comprising Diaper with a Sensor for Sensing Diaper Content", European patent WO2022136295A1, Jun. 30, 2022; US patent 20240293266, Sep. 5, 2024

List of Awards

- Huawei TechArena finalist 2022: **Arno Moerman**, Joris Van Kerrebrouck, Olivier Caytan, Igor Lima de Paula, Laurens Bogaert, Guy Torfs, Piet Demeester, Hendrik Rogier and Sam Lemey, “Beyond 5G Without Obstacles: mmWave-over-fiber Distributed Antenna Systems”
- Best Student Paper Award - 1st place at SPI 2024: Tim Pattyn, **Arno Moerman**, Martijn Huynen, and Dries Vande Ginste, “Differential Interconnects with Integrated Equalization and Common-Mode Filtering for Broadband Signal Integrity Enhancements in High-Speed PAM-4 Signaling”
- Best Student Paper Award - 2nd place at FLEPS 2024: Joryan Sennesael, **Arno Moerman**, Hendrik Rogier, and Patrick Van Torre, “Carbon-Ink Sensing Patterns for a Contactless Smart Diaper System”

List of Abbreviations

5G NR	fifth-generation new radio
5G	fifth generation, fifth-generation
6G	sixth generation, sixth-generation
ADC	analog-to-digital converter
AFSIW	air-filled substrate-integrated-waveguide
AI	artificial intelligence
AR	augmented reality
ARoF	analog radio-over-fiber
AWG	arbitrary waveform generator
AWGN	added white gaussian noise
B5G	beyond fifth generation
BFN	beamforming network
BPF	bandpass filter
BS	base station
C-JT	coherent joint transmission
CO	central office
CoMP	coordinated multipoint
CPRI	Common Public Radio Interface
DAC	digital-to-analog converter
DAS	distributed antenna system
DES	deserializer
DMIMO	distributed multiple-input multiple-output
DMLS	direct metal laser sintering
DRoF	digitized-radio-over-fiber
DSB	double sideband
E/O	electro-optical

EIRP	effective isotropic radiated power
eMBB	enhanced mobile broadband
EMF	electromagnetic fields
EMI	electromagnetic interference
ESIW	empty substrate-integrated-waveguide
EVM	error vector magnitude
FiWi	fiber-wireless
FR2	frequency range 2
FR3	frequency range 3
FTBR	front-to-back ratio
Gbps	gigabit per second
GCPW	grounded coplanar waveguide
HMD	headmount device
HPBW	half-power beamwidth
IC	integrated circuit
ICNIRP	international commission on non-ionizing radiation protection
IFoF	intermediate-frequency-over-fiber
IoE	internet of everything
IRS	intelligent reflective surface
LIS	large intelligent surface
LNA	low-noise amplifier
LO	local oscillator
LoS	line-of-sight
LTCC	low-temperature cofired ceramics
LTE	long term evolution
MIMO	multiple-input multiple-output
ML	machine learning
mMIMO	massive multiple-input multiple-output

mmWave	millimeter-wave
MRC	maximum-ratio combining
multi-RAT	multi-radio-access technology
MZM	Mach-Zehnder Modulator
NLoS	non-line-of-sight
O/E	opto-electrical
PA	power amplifier
PC	polarization controller
PCB	printed circuit board
PD	photodiode, photodetector
PIC	pohotonic integrated circuit
PRBS	pseudo random bit sequence
RAU	remote antenna unit
RFoF	radio-frequency-over-fiber
RIN	relative intensity noise
RIS	reflective intelligent surface
rms	root-mean-square
RTO	real-time oscilloscope
SC	selection combining
SDIFoF	sigma-delta intermediate-frequency-over-fiber
SDM	sigma-delta modulator
SDoF	sigma-delta-over-fiber
SER	serializer
SINAD	signal-to-noise-and-distortion ratio
SINR	signal-to-interference-plus-noise ratio
SIW	surface-integrated waveguide
SLA	stereolithography
SLL	sidelobe level
SNR	signal-to-noise ratio
SSB	single sideband

Tbps	terrabit per second
TDD	time-division-duplex
TRP	transmission/reception point
TRX	transceiver, transmit/receive
UE	user equipment
URLLC	ultra-reliable low latency communication
VNA	vector network analyzer
VR	virtual reality
XR	extended reality
ZF	zero forcing

mmWave-over-fiber Distributed Antenna Systems for Next-Generation Wireless Applications

1
Introduction

1.1 Context

In today's society, connectivity has become so deeply embedded in our daily lives that it is almost unimaginable to live without the ability to instantly reach each other. Since the first simple "*Merry Christmas.*" text message was sent in 1992 [1], network infrastructure has rapidly expanded over the past 30 years, providing internet connections with ever-increasing data throughput to an ever-growing number of users. While current fourth- and fifth-generation (4G/5G) networks already offer impressive data speeds, our world continues to evolve towards a data-centric future. This evolution is driving the development of networks beyond 5G, aiming to realize the Internet of Everything (IoE) [2]–[4], where a large number of people, countless devices and even more systems will communicate seamlessly over ultra-reliable, low-latency links with high data throughput.

The concept of the Internet of Everything has sparked a wave of visionary thinking exploring the potential "killer applications" that this new network could enable [5]–[8]. These applications are expected to seamlessly integrate into our daily lives, driving the widespread adoption of augmented and virtual reality (AR/VR) technologies. Extended reality, which builds on AR/VR, further enhances the experience by incorporating multi-sensor capabilities that engage all five human senses [6]. Notable examples include holographic telepresence and remote surgery, which have the potential to revolutionize communication and healthcare. Additionally, the IoE is set to transform industry through the adoption of the Industry 5.0 concept, where entire assembly lines will operate seamlessly together, and heavy machinery will be controlled remotely [4], [9].

Figure 1.1 illustrates some of these potential applications along with the

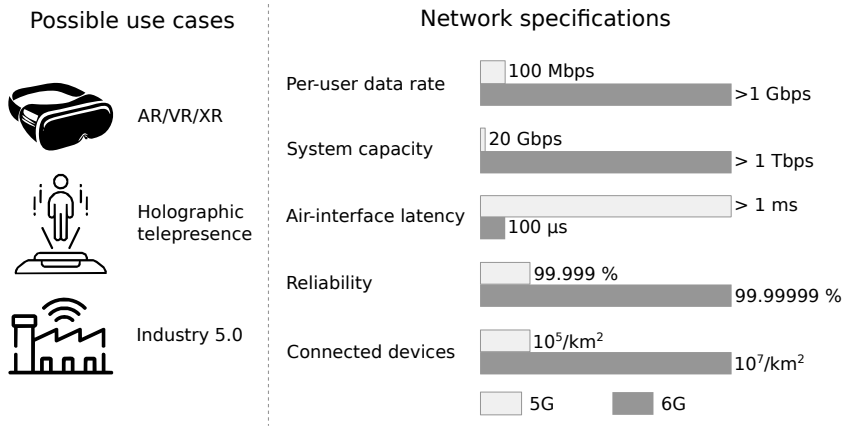

Figure 1.1: 6G network use cases and the specifications required to enable the Internet of Everything [6], [7]. It is clear that current-generation networks fall short realizing these needs.

projected network specifications required to deliver a fully immersive experience [6], [7]. It is clear that current-generation networks fall significantly short, missing key requirements by a factor of ten to one hundred. Moreover, while the fifth-generation network is designed to deliver either high data throughput (enhanced mobile broadband, eMBB), ultra reliable, low latency communication (URLLC), or massive connectivity depending on the application, the aforementioned applications in the sixth-generation network must achieve all of these features simultaneously [6]. While estimates for per-user data rates vary widely in the literature, ranging from gigabits per second [6], [10] to hundreds of gigabits per second [8], [11], and even terabits per second for uncompressed holograms [6], they all exceed the current maximum per-user data rate by at least an order of magnitude. When these increased data rates are combined with the massive growth in device density, the total system capacity surges well into the terabits per second range [7]. Given the unique demands of each application, one thing is clear: the network must undergo a substantial transformation to support the vast number of users, each requiring highly reliable, high-speed data access.

1.2 Motivation

To address the demands of next-generation wireless applications, particularly in terms of increased system capacity and data throughput, a shift to higher frequency bands, such as the millimeter-wave (mmWave) spectrum (30 GHz–300 GHz), is recognized as a key enabler. Unlike the heavily congested sub-6 GHz bands currently in use, these higher frequency bands are largely untapped and offer substantial bandwidth, with several GHz available in the lower mmWave range and even tens of GHz at the upper end. Figure 1.2 illustrates Nokia's spectrum vision for the 6G era, where the company anticipates deploying the new FR3 frequency band (7 GHz–24 GHz) primarily in densely populated urban areas. Immersive applications requiring reliable, high data throughput are expected to operate in the FR2 frequency band (24 GHz–71 GHz) and the sub-THz band (100 GHz–300 GHz), where abundant bandwidth is available [12]. However, operating at these higher frequencies introduces several challenges.

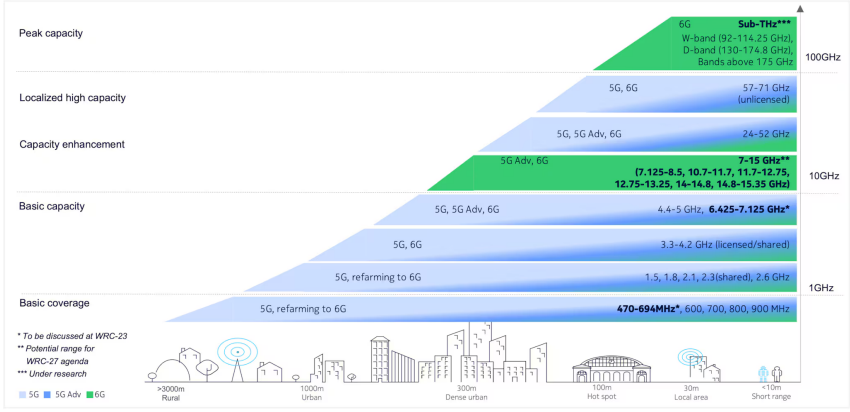

Figure 1.2: The 6G spectrum vision of Nokia [12]. Several new frequency bands are introduced, each serving their own specific area size with their envisioned total capacity requirement.

First, transitioning to the mmWave frequency bands result in shorter wavelengths, which in turn shrinks the feature sizes of wireless systems, making them more susceptible to fabrication tolerances. Additionally, at these mmWave frequencies, the reduced efficiency of amplifiers leads to lower

output powers on the transmit side and higher noise figures at the receive side [13], [14]. Combined with higher interconnect losses from increased dielectric and conductor losses, this degrades the link budget. These issues necessitate innovative manufacturing techniques capable of realizing small feature sizes with tight tolerances while maintaining high efficiency and affordability. Several technology and packaging platforms with tight tolerances are emerging [15]–[17]. Custom-designed printed circuit board (PCB) stack-ups and low-temperature cofired ceramics (LTCC) offer a good balanced trade-off between cost and feature size with straightforward integration of integrated circuits (IC) [15]. However, they often suffer from efficiency issues due to the lossy nature of the adopted materials [18]. Additionally, additive manufacturing techniques, such as stereolithography (SLA) [19], [20] and direct metal laser sintering (DMLS) [21]–[23] 3D-printing show promising results in maintaining tolerances below 15 µm. Moreover, from a tolerance standpoint, silicon micromachined structures offer the most precise control over feature size and tolerance (both < 1 µm). However, these fabrication methods come with higher cost [24], [25] and the integration of active circuitry remains a significant challenge due to interface losses and the need for routing control signals and DC power [26]. As a result, there is a growing demand for more efficient millimeterwave components in affordable technology platforms that facilitate IC integration, confine the electromagnetic fields within less lossy materials while routing, and enable efficient radiation [15], [25].

Moreover, wireless mmWave propagation is significantly affected by adverse propagation conditions, such as increased path loss, molecular absorption, and high penetration losses [6], all of which degrade link quality. Fortunately, combining antenna arrays with beamforming techniques can substantially increase the total gain, helping to offset these high losses [27]–[29]. By utilizing co-located antenna arrays, precise beamforming can be achieved to shape the beam toward a desired user while creating nulls to reduce interference with undesired users, thereby improving signal quality [27], [30]. Additionally, co-located massive MIMO arrays enhance data rates for multiple users simultaneously through spatial multiplexing, which directs different data streams along distinct spatial paths within the same frequency band [31]. Figure 1.3 illustrates the throughput of several mmWave wireless links as a function of carrier frequency [13]. It demonstrates that higher bandwidths at higher carrier frequencies allow for higher data rates. Furthermore, employing MIMO techniques result in an even higher throughput when compared to a single-channel link at the same carrier frequency. However, even co-located MIMO arrays at a single base station or access point remain vulnerable to

high penetration losses, leading to shadowing zones when obstacles or people obstruct the array [6], [32]–[37]. Hence, while the rollout of the mmWave spectrum along with base stations equipped with co-located arrays paves the way towards high-speed connectivity, it still falls short in delivering the reliability required for the envisioned 6G network [32]–[37].

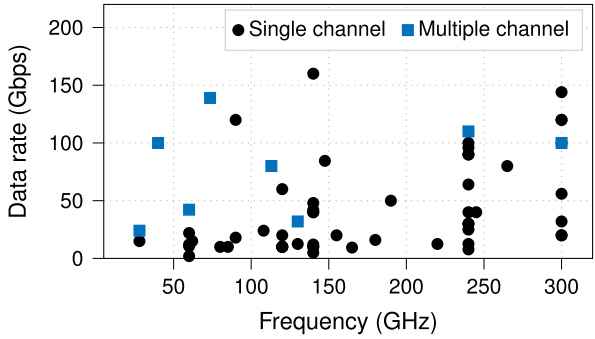

Figure 1.3: Data rate as a function of the carrier frequency of several recent mmWave wireless (MIMO) links, showing the potential of mmWave communication to enable high-throughput wireless links [13].

Another effective strategy to increase data throughput, total capacity, and reliability is cell densification, which involves deploying more base stations or access points within a given area, thereby reducing cell sizes [38]. For the past century, this approach has been a key factor behind Cooper's Law, which states that the wireless system capacity doubles approximately every other year [31], [38]. The increase in total throughput can be attributed to signal-to-interference-and-noise ratio (SINR) invariance, which indicates that the SINR remains unaffected even as base station density increases, allowing for more resources to be allocated to each user [38]. SINR invariance is quite robust and even holds under a number of network improvements such as densification through sectorization [39] and the use of space division multiple access [40]. Figure 1.4 visualizes cell densification through sectorization. The increased reliability, on the other hand, results from higher base station density which reduces the likelihood of signal blockage [41]. However, research suggests that SINR invariance no longer holds for dual-slope channel models with a close-in path loss exponent ≤ 3, which are common in indoor and dense outdoor environments at mmWave frequencies [42]. Beyond a certain level of densification, determined by the specific close-in path loss exponent, wireless link quality becomes interference-limited. Studies show that, at

this point, SINR and coverage probability decrease monotonically, adversely affecting both individual user throughput and overall system capacity [38]. While densification has been an effective solution for boosting throughput and improving reliability by mitigating base station shadowing, its effectiveness may diminish, and further densification may no longer be a viable strategy to prolong Cooper's Law.

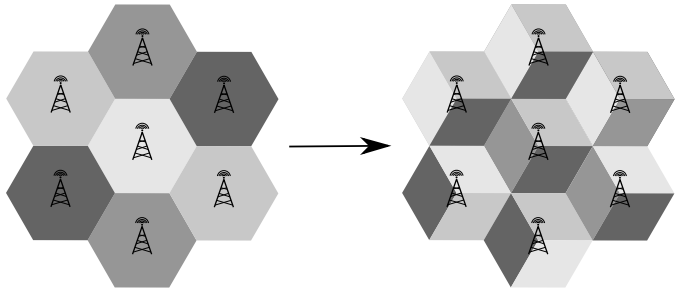

Figure 1.4: Example of cell densification through sectorization, splitting a given cell into multiple sectors. Cell densification has been a key enabler to increase data throughput, total capacity, and reliability in the past century.

A promising solution to tackle line-of-sight blockage issues with co-located mmWave massive MIMO arrays, as well as the challenges of cell densification, is the introduction of a split hardware architecture, known as a distributed antenna system (DAS) [43]. This architecture separates the mmWave radio components, termed remote antenna units (RAUs), from the base station part, called the central office (CO), to improve coordination among the increased number of distributed RAUs and to reduce the hardware costs associated with densification [43], [44]. Figure 1.5 shows a conceptual representation of a DAS, with the CO distributing signals to various RAUs spread across a building [45]. Initially, by switching between RAUs to ensure the best signal quality for a user, this approach enhances reliability and throughput, effectively implementing the densification strategy. Additionally, synchronized RAUs combined with MIMO techniques enable interference cancellation, extending the SINR invariance limit [38]. Traditionally, the network could be viewed as base stations surrounded by users. In this concept, however, the network evolves to users surrounded by multiple coordinated RAUs [46]. In 5G terminology, this strategy is known as Coordinated MultiPoint (CoMP) Coherent Joint Transmission (C-JT) [47]. Within this context, MIMO techniques are often referred to as cell-free MIMO or

distributed MIMO (DMIMO). Consequently, a mmWave DAS utilizing DMIMO techniques hold significant potential for effectively harnessing the mmWave broadband spectrum, paving the way for the next generation of ultra-reliable high-data-rate networks.

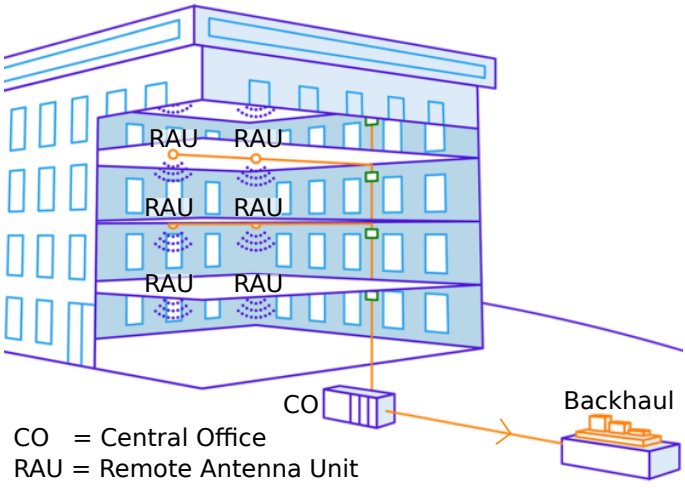

Figure 1.5: Distributed Antenna System (DAS) indicating a central office (CO) distributing signals to multiple remote antenna units (RAUs) distributed over a large building to ensure reliable high-datarate coverage [45].

Multiple theoretical studies on mmWave DASs and DMIMO, including studies on the optimal placement of RAUs for communication [48], [49] and sensing [50], have proven major improvements on the average throughput at the cell-edges and on localization performance, respectively, when compared to co-located and random RAU distribution approaches. Moreover, specific attention is devoted to MIMO signal processing in DAS to optimize channel capacity [51]–[53], improve analog beamforming [54], and estimate channel state information (CSI) under various conditions [55], [56]. Studies also indicate that increasing the number of distributed RAUs relative to the number of users lead to higher total capacity and reduced outage probability [46], [57], [58]. These findings demonstrate the potential of a large-scale mmWave DAS to accommodate a high number of users while boosting overall system capacity and reliability for future networks. However, a practical implementation that enables large-scale deployment of mmWave DAS has yet to be achieved.

1.3 State-of-the-Art

To advance toward efficient large-scale mmWave DASs, it is crucial to utilize low-loss routing technologies that enable synchronized spectrally-efficient communication between the numerous distributed RAUs and the central office (CO), thereby supporting the effective implementation of DMIMO. Additionally, high-performance, yet low-cost and low-power RAUs are essential to remain economically viable when scaling to scenarios where hundreds, or even thousands of end users are simultaneously served. Since traditional all-electric-based distribution approaches fall short for systems operating at high frequencies in terms of bandwidth and loss [59], [60], there is already a lot of research devoted to fiber-based interconnects. These are advantageous owing to the low-loss transmission of broadband signals, the compact size, light weight, and the immunity to electromagnetic interference [61]–[65]. Figure 1.6 illustrates three optical-based distribution methods [43], [65], being digitized-radio-over-fiber (DRoF), sigma-delta-over-fiber (SDoF), and analog-radio-over-fiber (ARoF), also known as mmWave-over-fiber when operating at mmWave frequencies.

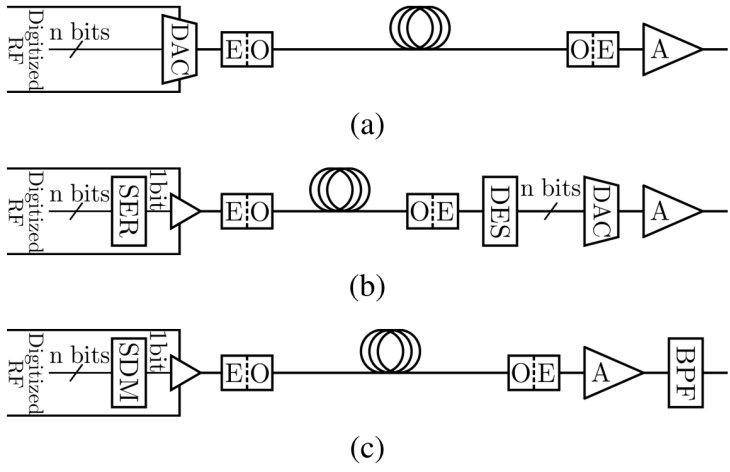

Figure 1.6: Radio signals are exchanged over fiber using (a) analog-radio-over-fiber (ARoF), (b) digitized-radio-over-fiber, or (c) sigma-delta-over-fiber. E/O: Electrical-to-optical; O/E: Optical-to-electrical; A: Amplifier; SER: Serializer; DES; Deserializer; SDM: Sigma Delta Modulator; BPF: Bandpass Filter. [65]

DRoF is the most mature architecture, with several standards, such as Common Public Radio Interface (CPRI) [66], already in commercial use. In a DRoF CO-to-RAU link, a binary stream is transmitted over fiber and the RAU must deserialize the stream and convert it to an analog mmWave signal using a digital-to-analog converter (DAC) and an upconversion stage. The transmission over fiber is very robust against distortion and non-linearities, achieving fiber throughputs between CO and RAU of more than 50 Gbps using standard cost-effective electro-optical transceivers [43], [63]. However, the RAU architecture is complex and involves higher power consumption due to the electronics required for deserialization, the DAC, upconversion and clock generation [65], rendering it unsuitable for cost-effective mmWave DAS deployments.

In SDoF, robustness against distortions is combined with a simpler and more efficient RAU architecture. A sigma-delta modulator (SDM) generates a digital-like signal by oversampling the analog input before modulating it onto a light carrier for transmission over fiber. This approach simplifies the RAU design, requiring only amplification and filtering of the signal to obtain the desired mmWave output signal. However, the performance of the SDM is constrained by the necessary oversampling ratio and the order of the SDM feedback filter, dictating the SDM complexity [43]. Sigma-delta-over-fiber-wireless links have been proposed in literature for FR2 frequency bands, achieving wireless data rates of up to 5.25 Gbps. Yet, achieving these rates requires oversampling ratios greater than 64, leading to high digital clock speeds over 50 GS/s for bandwidths limited to 500 MHz [43], [64], [67]. This limits the usability of SDoF in mmWave high-throughput wireless systems.

Next, in ARoF, the analog signal is modulated on a light carrier and transmitted through the optical link. Similar to SDoF, remote antenna units in ARoF schemes benefit from a simpler architecture that only requires opto-electric conversion and electrical amplification. This architecture is capable of supporting very broad bandwidths with high spectral efficiencies at the cost of needing highly linear opto-electronic components [43], [61], [62], [68]. The cost-effectiveness of ARoF RAUs is currently limited by these linear opto-electronic components. However, advancements in photonic integrated circuits (PICs) are expected to drive down these costs in the future [69], [70]. Some single fiber-wireless links in the FR2 frequency bands have demonstrated data rates up to 12 Gbps in downlink [71], [72] and a maximum throughput of 7 Gbps in both up- and downlink [73]. Despite this, most analog-over-fiber-wireless links operate below 6 GHz [74]–[77], due to the

scarcity of highly linear opto-electric components with large bandwidths. Hence, while ARoF intrinsically offers broad bandwidths with low-complexity RAU architectures, current implementations often underutilize available bandwidth and are constrained to single fiber-wireless links.

Lastly, variations of ARoF and SDoF have been proposed where an intermediate-frequency signal is transmitted over fiber and upconverted at the RAU. This approach can be implemented using ARoF, resulting in intermediate-frequency-over-fiber (IFoF) [78], [79], or using SDoF, leading to sigma-delta-intermediate-frequency-over-fiber (SDIFoF) [80]–[82]. Both approaches have similar advantages as their direct radio-frequency counterparts, being large bandwidths for ARoF and high distortion immunity for SDoF, but with the additional advantage that the bandwidth requirements of the opto-electronic and electro-optic transducers are relaxed. However, these approaches have notable drawbacks, including the need for power-hungry up- and downconversion at the RAU and the need for synchronized clock generation at the RAU, adding extra complexity and resulting in more difficult DMIMO implementation. A single fiber-wireless IFoF link is shown around a 60 GHz carrier frequency, achieving 24 Gbps [78]. Furthermore, mmWave DAS implementations using intermediate-frequency methods have reached a maximum data throughput of 6 Gbps in FR2 frequency bands [79]–[83]. Despite these advances, the power demands, the complexity, and the cost of RAUs remain significant obstacles hindering a possible large-scale roll-out.

Despite the clear potential of mmWave DAS and the advancements in fiber-based distribution methods, a practical mmWave DAS designed for large-scale deployment is still needed to ensure reliable, high-data-rate communication towards numerous simultaneous users, enabling the envisioned multi-sensory "killer applications" in the beyond 5G era. To this end, several research questions must be addressed to fully unleash the potential of mmWave DAS in real-world environments, especially when serving multiple users in conditions with frequent non-line-of-sight challenges.

- How can synchronized data communication between the central office and multiple remote antenna units be achieved to enable the effective implementation of DMIMO systems?
- How can the mmWave RAU architecture be optimized to balance simplicity and cost-effectiveness, enabling large-scale deployment while maintaining high performance in challenging real-life environments?

- How can a mmWave DAS be designed and optimized in a time-efficient and accurate way, while taking into account real-life deployment scenarios?
- How is the user's exposure affected, and how do the electromagnetic fields behave around a user when surrounded by a large-scale mmWave DAS with numerous remote antenna units?

1.4 Own Contributions and Outline

This doctoral dissertation investigates and proposes innovative photonic-enabled distributed antenna systems to overcome the challenging propagation conditions at mmWave frequencies and the exploitation of air-filled substrate-integrated-waveguide-based remote antenna units to enable their practical deployment. The research contributes to the advancement of wireless mmWave communication through the following achievements:

1. The first implementation of a realistic mmWave-over-fiber distributed antenna system, establishing high-data-rate wireless communication in real-life environments with challenging non-line-of-sight conditions. (Chapter 2)

- A novel photonically-enabled mmWave-over-fiber-based architecture was proposed to practically realize mmWave DASs. It consists of a CO, responsible for the signal processing and ensures synchronized exchange of broadband mmWave signals between CO and the distributed RAUs.
- The exploitation of AFSIW technology is analyzed to realize high-performance, yet cost-efficient RAUs that maintain their performance when deployed in challenging environments.
- The ultra-low-cost nature of the RAUs is further invigorated by leveraging a single fiber for both up- and downlink fiber-wireless communication, enabling laser-free RAU operation.
- A 48-Gbps wireless communication link is established between a central office and the user equipment in a realistic Industry 5.0 environment

using two RAUs and four user equipment (UE) antennas, by leveraging the synchronized nature of the architecture to demonstrate the potential of mmWave-over-fiber distributed antenna systems. This lays the groundwork for the implementation of large-scale distributed MIMO systems, or large intelligent surfaces (LIS).

2. mmWave fiber-wireless experiments in real-life environments to assess and enhance throughput and reliability. (Chapter 3)

- A system-level analysis is performed by varying the baudrate, laser power, and amplifier gain to optimize the throughput of a single-input single-output (SISO) fiber-wireless link in an anechoic chamber. A representative experiment yielded a signal quality of 12.5 % EVM at a distance of 2 m, resulting in a throughput of 24 Gbps with a symbol rate of 6 GBaud.
- The reliability and robustness of the system against self-blockage, which is detrimental for the link quality, is increased by distributing four antennas at the UE. By switching between the UE's antennas (selection combining (SC)), the link quality remains guaranteed over a full rotation of the user by 360°, except in handover regions where the signal quality drops (EVM $>$ 12.5 %).
- More advanced processing of the signals by performing Maximum Ratio Combining (MRC), is compared to SC, resulting in an enhancement up to 3 % EVM in link quality within handover regions in an anechoic environment, and for different distances to the RAU in real-life Industry 5.0 environment.

3. Multi-disciplinary system-level framework to assess and optimize mmWave-over-fiber-based DAS. (Chapter 4)

- A modular system-level framework is proposed that facilitates accurate and time-efficient optimization of mmWave-over-fiber DAS by optimally linking commercial software and in-house developed code. The framework takes into account nonlinear distortion and noise in the

mmWave-over-fiber link and in the amplifiers by relying on circuit models, the mismatch and frequency-dependent radiation patterns of the antenna front-ends by means of a full-wave electromagnetic model, and the wireless channel via an analytical model.

- A first measurement campaign proves a good agreement between predicted and measured signal quality, expressed in EVM, of a single fiber-wireless link in an anechoic chamber, when varying several system-level variables such as optical power, signal input power and baudrate. This confirms the symbiosis between the different framework modules in terms of accurately modeling the different passive and active optical, opto-electrical, and electrical components.

- A second measurement campaign shows a good agreement between measured and simulated signal quality as a function of different UE positions in both up- and downlink. This validates the framework as a tool to accurately assess the signal quality in a DAS for certain environments and positions, by including full-wave simulations.

- The influence of different channel models is studied to show the modular nature of the framework. This is done by also performing the measurements in a half-anechoic environment and implementing a two-ray channel model, which agrees well with measurements.

- Finally, the impact of inter-user interference is analyzed by modelling and measuring a multi-user scenario where different UEs are served by the same multi-beam RAU. As seen in both measurements and simulations, a RAU based on a Butler matrix is able to serve multiple users simultaneously, but at a lower data throughput due to the signal quality degradation.

4. mmWave-over-fiber DAS for interactive AR/VR with headmount UEs: antenna, bio-electromagnetic, and system-level analysis. (Chapter 5)

- A DAS with several distributed RAUs is proposed and found suitable to increase the communication link quality by switching to links with no blockage loss. Additionally, this DAS is ideal to keep the background exposure low.

- The AR/VR environment is studied from a bio-electromagnetic and antenna systems designer perspective, leading to a new metric that links bio-electromagnetic criteria with wireless communication specifications to acquire valuable insights on antenna design and system considerations.
- Different mmWave antenna topologies are studied using this metric. It is shown that air-filled substrate-integrated-waveguide topologies provide the highest platform-independency while having a low absorbed power density in the human body.
- Measurements in an anechoic chamber using a bio-electromagnetically accurate phantom head show a reliable link in an interactive VR scenario with a headmount UE. By exploiting spatial and polarization diversity at the UE side, high-data-rate mmWave communication is demonstrated up to 12 Gbps withing the n257 frequency band (26.5 GHz-29.5 GHz), even when the UE rotates and when a blockage loss up to 30 dB occurs.

References

[1] BBC, *'Merry Christmas': 30 years of the text message*, Aug. 2024. [Online]. Available: https://www.bbc.com/news/technology-63825894.

[2] M. H. Miraz, M. Ali, P. S. Excell, and R. Picking, "A review on Internet of Things (IoT), Internet of everything (IoE) and Internet of nano things (IoNT)", *2015 Internet Technologies and Applications (ITA)*, pp. 219–224, 2015.

[3] D. Evans, *The Internet of Everything: How More Relevant and Valuable Connections Will Change the World*, Cisco Internet Business Solution Group (IBSG), Cisco Systems, Inc., White paper 2012 [Online] Available: https://www.cisco.com/c/dam/global/en_my/assets/ciscoinnovate/pdfs/{I}o{E}.pdf.

[4] P. K. R. Maddikunta, Q.-V. Pham, P. B, *et al.*, "Industry 5.0: A survey on enabling technologies and potential applications", *Journal of Industrial Information Integration*, vol. 26, p. 100 257, 2022.

[5] Horizon 2020 Project: A flagship for B5G/6G vision and intelligent fabric of technology enablers connecting human, physical, and digital worlds, *Expanded 6G vision, use cases and societal values (Deliverable D1.2)*, [Online] Available: https://hexa-x.eu/wp-content/uploads/2022/04/Hexa-X_D1.2_Edited.pdf.

[6] M. Giordani, M. Polese, M. Mezzavilla, S. Rangan, and M. Zorzi, "Toward 6G networks: Use cases and technologies", *IEEE communications magazine*, vol. 58, no. 3, pp. 55–61, 2020.

[7] Z. Zhang, Y. Xiao, Z. Ma, *et al.*, "6g wireless networks: Vision, requirements, architecture, and key technologies", *IEEE vehicular technology magazine*, vol. 14, no. 3, pp. 28–41, 2019.

[8] F. Hu, Y. Deng, W. Saad, M. Bennis, and A. H. Aghvami, "Cellular-connected wireless virtual reality: Requirements, challenges, and solutions", *IEEE Communications Magazine*, vol. 58, no. 5, pp. 105–111, 2020.

[9] M. Gundall, M. Strufe, H. D. Schotten, *et al.*, "Introduction of a 5G-enabled architecture for the realization of industry 4.0 use cases", *IEEE access*, vol. 9, pp. 25 508–25 521, 2021.

[10] E. Bastug, M. Bennis, M. Médard, and M. Debbah, "Toward interconnected virtual reality: Opportunities, challenges, and enablers", *IEEE Communications Magazine*, vol. 55, no. 6, pp. 110–117, 2017.

[11] T. Taleb, Z. Nadir, H. Flinck, and J. Song, "Extremely interactive and low-latency services in 5G and beyond mobile systems", *IEEE Communications Standards Magazine*, vol. 5, no. 2, pp. 114–119, 2021.

[12] Nokia [White Paper], *Spectrum for 6G explained*, [Online] Available: `https://www.nokia.com/about-us/newsroom/articles/spectrum-for-6G-explained/`.

[13] T. Maiwald, T. Li, G.-R. Hotopan, *et al.*, "A review of integrated systems and components for 6G wireless communication in the D-band", *Proceedings of the IEEE*, vol. 111, no. 3, pp. 220–256, 2023.

[14] V. Camarchia, R. Quaglia, A. Piacibello, D. P. Nguyen, H. Wang, and A.-V. Pham, "A review of technologies and design techniques of millimeter-wave power amplifiers", *IEEE Transactions on Microwave Theory and Techniques*, vol. 68, no. 7, pp. 2957–2983, 2020.

[15] L. Van Messem, R. Broucke, H. Rogier, *et al.*, "Consistent and Cost-Effective PCB-Based D-Band Air-Filled Substrate-Integrated-Waveguide Filters", in *2024 IEEE International Microwave Filter Workshop (IMFW)*, IEEE, 2024, pp. 167–169.

[16] X. Gu, D. Liu, and B. Sadhu, "Packaging and antenna integration for silicon-based millimeter-wave phased arrays: 5G and beyond", *IEEE Journal of Microwaves*, vol. 1, no. 1, pp. 123–134, 2021.

[17] A. O. Watanabe, M. Ali, S. Y. B. Sayeed, R. R. Tummala, and M. R. Pulugurtha, "A review of 5G front-end systems package integration", *IEEE Transactions on Components, Packaging and Manufacturing Technology*, vol. 11, no. 1, pp. 118–133, 2020.

[18] M. Ihle, S. Ziesche, C. Zech, and B. Baumann, "Functional printing of MMIC-interconnects on LTCC packages for sub-THz applications", in *2019 22nd European Microelectronics and Packaging Conference & Exhibition (EMPC)*, IEEE, 2019, pp. 1–4.

[19] J. Shen, M. W. Aiken, M. Abbasi, *et al.*, "Rapid prototyping of low loss 3D printed waveguides for millimeter-wave applications", in *2017 IEEE MTT-S International Microwave Symposium (IMS)*, IEEE, 2017, pp. 41–44.

[20] K. Lomakin, M. Sippel, K. Helmreich, and G. Gold, "Design and analysis of 3d printed slotted waveguides for d-band using stereolithography and electroless silver plating", in *2020 IEEE/MTT-S International Microwave Symposium (IMS)*, IEEE, 2020, pp. 177–180.

[21] B. Zhang and H. Zirath, "Metallic 3-D printed rectangular waveguides for millimeter-wave applications", *IEEE Transactions on Components, Packaging and Manufacturing Technology*, vol. 6, no. 5, pp. 796–804, 2016.

[22] S. Y. Chin, V. Dikshit, B. Meera Priyadarshini, and Y. Zhang, "Powder-based 3D printing for the fabrication of device with micro and mesoscale features", *Micromachines*, vol. 11, no. 7, p. 658, 2020.

[23] B. Nagarajan, Z. Hu, X. Song, W. Zhai, and J. Wei, "Development of micro selective laser melting: the state of the art and future perspectives", *Engineering*, vol. 5, no. 4, pp. 702–720, 2019.

[24] B. Beuerle, J. Campion, U. Shah, and J. Oberhammer, "Low-Loss Silicon Micromachined Waveguides Above 100 GHz Utilising Multiple H-Plane Splits", in *2018 48th European Microwave Conference (EuMC)*, 2018, pp. 1041–1044.

[25] A. Krivovitca, U. Shah, O. Glubokov, and J. Oberhammer, "Micromachined silicon-core substrate-integrated waveguides at 220–330 GHz", *IEEE Transactions on Microwave Theory and Techniques*, vol. 68, no. 12, pp. 5123–5131, 2020.

[26] T. Maiwald, T. Li, G.-R. Hotopan, *et al.*, "A Review of Integrated Systems and Components for 6G Wireless Communication in the D-Band", *Proceedings of the IEEE*, vol. 111, no. 3, pp. 220–256, 2023.

[27] H. Steyskal, "Digital Beamforming Antennas: an Introduction.", *Microwave journal*, vol. 30, no. 1, 1987.

[28] I. Ahmed, H. Khammari, A. Shahid, *et al.*, "A survey on hybrid beamforming techniques in 5G: Architecture and system model perspectives", *IEEE Communications Surveys & Tutorials*, vol. 20, no. 4, pp. 3060–3097, 2018.

[29] S. Payami, M. Khalily, A. Araghi, *et al.*, "Developing the first mmWave fully-connected hybrid beamformer with a large antenna array", *IEEE Access*, vol. 8, pp. 141 282–141 291, 2020.

[30] S. Noh, M. D. Zoltowski, and D. J. Love, "Multi-resolution codebook and adaptive beamforming sequence design for millimeter wave beam alignment", *IEEE Transactions on Wireless Communications*, vol. 16, no. 9, pp. 5689–5701, 2017.

[31] E. Björnson, E. G. Larsson, and T. L. Marzetta, "Massive MIMO: Ten myths and one critical question", *IEEE Communications Magazine*, vol. 54, no. 2, pp. 114–123, 2016.

[32] X. Zhao, Q. Wang, S. Li, *et al.*, "Attenuation by human bodies at 26-and 39.5-GHz millimeter wavebands", *IEEE Antennas and Wireless Propagation Letters*, vol. 16, pp. 1229–1232, 2016.

[33] R. Schulpen, L. A. Bronckers, A. B. Smolders, and U. Johannsen, "Impact of Human Blockage on Dynamic Indoor Multipath Channels at 27 GHz", *IEEE Transactions on Antennas and Propagation*, vol. 70, no. 9, pp. 8291–8303, 2022.

[34] U. T. Virk and K. Haneda, "Modeling human blockage at 5G millimeter-wave frequencies", *IEEE Transactions on Antennas and Propagation*, vol. 68, no. 3, pp. 2256–2266, 2019.

[35] C. Ballesteros, L. Vähä-Savo, K. Haneda, C. Icheln, J. Romeu, and L. Jofre, "Assessment of mmWave handset arrays in the presence of the user body", *IEEE Antennas and Wireless Propagation Letters*, vol. 20, no. 9, pp. 1736–1740, 2021.

[36] D. Prado-Alvarez, S. Inca, D. Martín-Sacristán, and J. F. Monserrat, "Millimeter-wave human blockage model enhancements for directional antennas and multiple blockers", *IEEE Communications Letters*, vol. 25, no. 9, pp. 2776–2780, 2021.

[37] L. A. Fierro, E. C. Maggi, A. A. Vazquez, and D. Schkolnik, "Empirical results for human-induced shadowing events for indoor 60 GHz wireless links", *IEEE Access*, vol. 8, pp. 44 522–44 533, 2020.

[38] J. G. Andrews, X. Zhang, G. D. Durgin, and A. K. Gupta, "Are we approaching the fundamental limits of wireless network densification?", *IEEE Communications Magazine*, vol. 54, no. 10, pp. 184–190, 2016.

[39] B. Błaszczyszyn and M. K. Karray, "Spatial distribution of the SINR in Poisson cellular networks with sector antennas", *IEEE Transactions on Wireless Communications*, vol. 15, no. 1, pp. 581–593, 2015.

[40] H. S. Dhillon, M. Kountouris, and J. G. Andrews, "Downlink MIMO HetNets: Modeling, ordering results and performance analysis", *IEEE Transactions on Wireless Communications*, vol. 12, no. 10, pp. 5208–5222, 2013.

[41] I. K. Jain, R. Kumar, and S. Panwar, "Driven by capacity or blockage? A millimeter wave blockage analysis", in *2018 30th International Teletraffic Congress (ITC 30)*, IEEE, vol. 1, 2018, pp. 153–159.

[42] G. R. Maccartney, T. S. Rappaport, S. Sun, and S. Deng, "Indoor office wideband millimeter-wave propagation measurements and channel models at 28 and 73 GHz for ultra-dense 5G wireless networks", *IEEE access*, vol. 3, pp. 2388–2424, 2015.

[43] G. Torfs, A. Vandierendonck, F. Zardosht, *et al.*, "Sigma-Delta-over-Fiber", in *2024 Optical Fiber Communications Conference and Exhibition (OFC)*, 2024, pp. 1–3.

[44] Lance Brown [Blogpost], *What are RAN Functional Splits*, [Online] Available: `https://www.linkedin.com/pulse/what-ran-functional-splits-lance-brown/`.

[45] Abiom [Product Page], *Sistributed Antenna System (DAS)*, [Online] Available: `https://abiom.nl/nl/productgroep/portofonie-infrastructuur/distributed-antenna-system-das/`.

[46] Ö. T. Demir, E. Björnson, L. Sanguinetti, *et al.*, "Foundations of user-centric cell-free massive MIMO", *Foundations and Trends® in Signal Processing*, vol. 14, no. 3-4, pp. 162–472, 2021.

[47] S. Muruganathan, S. Faxer, S. Jarmyr, S. Gao, and M. Frenne, "On the system-level performance of coordinated multi-point transmission schemes in 5G NR deployment scenarios", in *2019 IEEE 90th vehicular technology conference (VTC2019-fall)*, IEEE, 2019, pp. 1–5.

[48] A. Minasian, R. S. Adve, S. Shahbazpanahi, and G. Boudreau, "On RRH placement for multi-user distributed massive MIMO systems", *IEEE Access*, vol. 6, pp. 70 597–70 614, 2018.

[49] H. A. Ammar, R. Adve, S. Shahbazpanahi, and G. Boudreau, "Optimizing RRH placement under a noise-limited point-to-point wireless backhaul", in *ICC 2021-IEEE International Conference on Communications*, IEEE, 2021, pp. 1–6.

[50] P. Chen, C. Qi, and L. Wu, "Antenna placement optimisation for compressed sensing-based distributed MIMO radar", *IET Radar, Sonar & Navigation*, vol. 11, no. 2, pp. 285–293, 2017.

[51] M. Jafri, S. Srivastava, N. K. Venkategowda, A. K. Jagannatham, and L. Hanzo, "Cooperative hybrid transmit beamforming in cell-free mmWave MIMO networks", *IEEE Transactions on Vehicular Technology*, vol. 72, no. 5, pp. 6023–6038, 2023.

[52] Z. H. Shaik, E. Björnson, and E. G. Larsson, "MMSE-optimal sequential processing for cell-free massive MIMO with radio stripes", *IEEE Transactions on Communications*, vol. 69, no. 11, pp. 7775–7789, 2021.

[53] E. Björnson and L. Sanguinetti, "Cell-free versus cellular massive MIMO: What processing is needed for cell-free to win?", in *2019 IEEE 20th International Workshop on Signal Processing Advances in Wireless Communications (SPAWC)*, IEEE, 2019, pp. 1–5.

[54] S. Buzzi, C. D'Andrea, M. Fresia, and X. Wu, "Multi-UE multi-AP beam alignment in user-centric cell-free massive MIMO systems operating at mmWave", *IEEE Transactions on Wireless Communications*, vol. 21, no. 11, pp. 8919–8934, 2022.

[55] G. Femenias and F. Riera-Palou, "Cell-free millimeter-wave massive MIMO systems with limited fronthaul capacity", *IEEE Access*, vol. 7, pp. 44 596–44 612, 2019.

[56] Y. Jin, J. Zhang, S. Jin, and B. Ai, "Channel estimation for cell-free mmWave massive MIMO through deep learning", *IEEE Transactions on Vehicular Technology*, vol. 68, no. 10, pp. 10 325–10 329, 2019.

[57] W. Roh and A. Paulraj, "MIMO channel capacity for the distributed antenna", in *Proceedings IEEE 56th Vehicular Technology Conference*, IEEE, vol. 2, 2002, pp. 706–709.

[58] E. Björnson and L. Sanguinetti, "Scalable cell-free massive MIMO systems", *IEEE Trans. Commun.*, vol. 68, no. 7, pp. 4247–4261, 2020.

[59] H. Pirayesh, P. K. Sangdeh, Q. Yan, and H. Zeng, "UD-MIMO: Uplink Distributed MIMO for Wireless LANs", in *2021 18th Annual IEEE International Conference on Sensing, Communication, and Networking (SECON)*, IEEE, 2021, pp. 1–9.

[60] N. Tawa, T. Kuwabara, Y. Maruta, and T. Kaneko, "28 GHz Distributed-MIMO Comprehensive Antenna Calibration for 5G Indoor Spatial Division Multiplex", in *2021 IEEE MTT-S International Microwave Symposium (IMS)*, IEEE, 2021, pp. 541–544.

[61] C. H. Cox, "Noise in links", in *Analog Optical Links: Theory and Practice*, Cambridge, UK: Cambridge University Press, 2004, ch. 5, sec. 2, pp. 160-168.

[62] C. H. Cox, E. I. Ackerman, G. E. Betts, and J. L. Prince, "Limits on the performance of RF-over-fiber links and their impact on device design", *IEEE Trans. Microw. Theory Techn.*, vol. 54, no. 2, pp. 906–920, Feb. 2006.

[63] K. Szczerba, P. Westbergh, J. Karout, *et al.*, "4-PAM for high-speed short-range optical communications", *Journal of optical communications and networking*, vol. 4, no. 11, pp. 885–894, 2012.

[64] H. Li, M. Verplaetse, J. Verbist, *et al.*, "Real-time 100-GS/s sigma-delta modulator for all-digital radio-over-fiber transmission", *Journal of Lightwave Technology*, vol. 38, no. 2, pp. 386–393, 2020.

[65] L. Breyne, G. Torfs, X. Yin, P. Demeester, and J. Bauwelinck, "Comparison Between Analog Radio-Over-Fiber and Sigma Delta Modulated Radio-Over-Fiber", *IEEE Photon. Technol. Lett.*, vol. 29, no. 21, pp. 1808–1811, Nov. 2017.

[66] *Common Public Radio Interface (CPRI)*, Accessed: August 2024. [online]. Available: `https://www.cpri.info/`.

[67] J. Declercq, H. Li, J. Van Kerrebrouck, *et al.*, "Low power all-digital radio-over-fiber transmission for 28-GHz band using parallel electro-absorption modulators", *Journal of Lightwave Technology*, vol. 39, no. 4, pp. 1125–1131, 2021.

[68] J. Beas, G. Castanon, I. Aldaya, A. Aragón-Zavala, and G. Campuzano, "Millimeter-wave frequency radio over fiber systems: a survey", *IEEE Communications surveys & tutorials*, vol. 15, no. 4, pp. 1593–1619, 2013.

[69] R. Nagarajan, C. H. Joyner, R. P. Schneider, *et al.*, "Large-scale photonic integrated circuits", *IEEE Journal of Selected Topics in Quantum Electronics*, vol. 11, no. 1, pp. 50–65, 2005.

[70] R. Helkey, A. A. Saleh, J. Buckwalter, and J. E. Bowers, "High-performance photonic integrated circuits on silicon", *IEEE Journal of Selected Topics in Quantum Electronics*, vol. 25, no. 5, pp. 1–15, 2019.

[71] Y. Tian, K.-L. Lee, C. Lim, and A. Nirmalathas, "Demonstration of non-orthogonal multiple access scheme using multilevel coding without successive interference cancellation with 60 GHz radio-over-fiber fronthaul", in *2018 Optical Fiber Communications Conference and Exposition (OFC)*, IEEE, 2018, pp. 1–3.

[72] H.-Y. Wang, Y.-C. Chi, Y.-W. Chen, and G.-R. Lin, "Tri-color optical transmitter with embedding 28-GHz millimeter-wave carrier for 5G mobile over fiber", in *CLEO: Science and Innovations*, Optica Publishing Group, 2017, SM1O–1.

[73] L. Bogaert, J. Van Kerrebrouck, H. Li, *et al.*, "SiPhotonics/GaAs 28-GHz Transceiver With Reflective EAM for Laser-Less mmWave-Over-Fiber", *J. Lightw. Technol.*, vol. 39, no. 3, pp. 779–786, 2021.

[74] X. Yu, T. B. Gibbon, and I. T. Monroy, "Bidirectional radio-over-fiber system with phase-modulation downlink and RF oscillator-free uplink using a reflective SOA", *IEEE Photonics Technology Letters*, vol. 20, no. 24, pp. 2180–2182, 2008.

[75] G. Torfs, H. Li, S. Agneessens, *et al.*, "ATTO: Wireless networking at fiber speed", *Journal of Lightwave Technology*, vol. 36, no. 8, pp. 1468–1477, 2017.

[76] J.-S. Yoon, H.-S. Kang, M.-J. Lee, K.-Y. Park, and W.-Y. Choi, "CMOS integrated optical receivers for radio-over-fiber transmission of IEEE 802.11 g WLAN signals", in *Proceedings of the Asia-Pacific Microwave Photonics Conference, Beijing, China*, 2009, pp. 22–24.

[77] M. Ko, M.-J. Lee, H. Rücker, and W.-Y. Choi, "Silicon photonics-wireless interface ICs for micro-/millimeter-wave fiber-wireless networks", *Optics express*, vol. 21, no. 19, pp. 22 962–22 973, 2013.

[78] N. Argyris, G. Giannoulis, K. Kanta, *et al.*, "A 5G mmWave fiber-wireless IFoF analog mobile fronthaul link with up to 24-Gb/s multiband wireless capacity", *Journal of Lightwave Technology*, vol. 37, no. 12, pp. 2883–2891, 2019.

[79] J. Kim, M. Sung, S.-H. Cho, *et al.*, "MIMO-supporting radio-over-fiber system and its application in mmWave-based indoor 5G mobile network", *Journal of Lightwave Technology*, vol. 38, no. 1, pp. 101–111, 2019.

[80] H. Bao, Z. S. He, F. Ponzini, and C. Fager, "Demonstration of flexible mmWave digital beamforming transmitter using sigma-delta radio-over-fiber link", in *2022 52nd European Microwave Conference (EuMC)*, IEEE, 2022, pp. 692–695.

[81] H. Bao, F. Ponzini, and C. Fager, "Flexible mm-Wave sigma-delta-over-fiber MIMO link", *Journal of Lightwave Technology*, vol. 41, no. 14, pp. 4734–4742, 2023.

[82] H. Bao, F. Ponzini, and C. Fager, “Wideband mm-wave 6 × 2 Distributed MIMO Transmitter using Sigma-Delta-over-Fiber”, *Journal of Lightwave Technology*, 2024.

[83] C.-Y. Wu, H. Li, J. Van Kerrebrouck, *et al.*, “Distributed antenna system using sigma-delta intermediate-frequency-over-fiber for frequency bands above 24 GHz”, *J. Lightw. Technol.*, vol. 38, no. 10, pp. 2765–2773, May 2020.

2

Beyond 5G Without Obstacles: Distributed Antenna Systems Based on mmWave-over-Fiber

Based on "Beyond 5G Without Obstacles: mmWave-over-Fiber Distributed Antenna Systems" by Arno Moerman, Joris Van Kerrebrouck, Olivier Caytan, Igor Lima de Paula, Laurens Bogaert, Guy Torfs, Piet Demeester, Hendrik Rogier and Sam Lemey, as published in Communications Magazine.

Beyond-5G wireless systems require significant improvement to enable the Internet of Everything, offering ultra-reliability, ultra-low-latency and high data-rates for holographic telepresence, immersive augmented and virtual reality, and cyber-physical systems in Industry 5.0. The mmWave frequency band (30 GHz to 300 GHz) provides the required bandwidths, but very challenging propagation conditions exist. Conventional co-located multi-antenna systems counter higher path loss, but are insufficient in challenging real-life scenarios with frequent non-line-of-sight conditions. For distributed massive MIMO systems or large intelligent surfaces, we advocate optically-enabled distributed antenna systems (DAS) to alleviate these issues. To ensure tight synchronization and scalability, we propose a mmWave-over-fiber based architecture with low-complexity high-performance remote antenna units (RAUs). Strategically distributing and integrating RAUs in the user equipments' environment yield high throughput and reliable coverage. We demonstrate a mmWave-over-fiber DAS yielding multi-Gbps mmWave communication in a harsh indoor environment with non-line-of-sight conditions, measuring wireless data rates up to 24 Gbps, by selecting the RAU yielding the best link quality, and up to 48 Gbps, by leveraging distributed MIMO techniques.

2.1 Introduction

Through massive multiple-input multiple-output (mMIMO) wireless communication, the fifth-generation (5G) wireless mobile network provides enhanced mobile broadband (eMBB) access, but falls short as enabler for the Internet of Everything (IoE), where multiple devices require eMBB at millimeter-wave (mmWave) frequencies to communicate at high data rate, high reliability and low latency. The performance of current basic IoE and ultra-reliable low latency communication (URLLC) does not meet the ever-increasing demands of emerging wireless applications [1]. Holographic telepresence, immersive multisensory interactive augmented and virtual reality (AR/VR), and cyber-physical systems in Industry 5.0 require high data rates (up to multiple Gbps per-user and up to one Tbps aggregated), with strict reliability (99.99999 %) and air-interface latency (100 µs) conditions. Beyond 5G (B5G) and 6G networks must jointly meet all stringent network demands [2] (reliability, capacity, data rate, latency and energy efficiency).

Unleashing the full potential of B5G and 6G requires a holistic multi-disciplinary approach, based on disruptive communication technologies, innovative network architectures, and artificial intelligence (AI) [1]. To support extremely high data rates, mmWave (30 GHz to 300 GHz) and TeraHertz (0.1 THz to 10 THz) frequency bands play a key role. Yet, at these frequencies, challenging propagation conditions exist, such as increased path loss, higher penetration loss, and more severe shadowing. However, the very short wavelengths facilitate the integration of a massive number of antenna elements in a small footprint to counter the unfavorable path loss and to mitigate impact of user mobility through adaptive beamforming [3]. Moreover, MIMO algorithms can further optimize throughput and reliability. Still, a conventional co-located approach, with all antennas compactly grouped at a single location, cannot maintain the very high data rates in challenging, non-line-of-sight (NLoS), real-life conditions, due to shadowing or self-blocking, as illustrated in Figure 2.1 (Challenge #1), with the user equipment (UE) obstructing the line-of-sight (LoS) path. This represents a major issue in Industry 5.0 and interactive AR/VR applications, due to (1) very challenging UE antenna deployment conditions, on metal robots in the former and human bodies in the latter, and (2) the use of directive antennas with high antenna-to-integration-platform isolation. Additionally, link quality also deteriorates in other NLoS scenarios, as in Challenge #2, where obstacles (static machinery/racks or dynamic robots/humans) block the LoS-path between UE and access point.

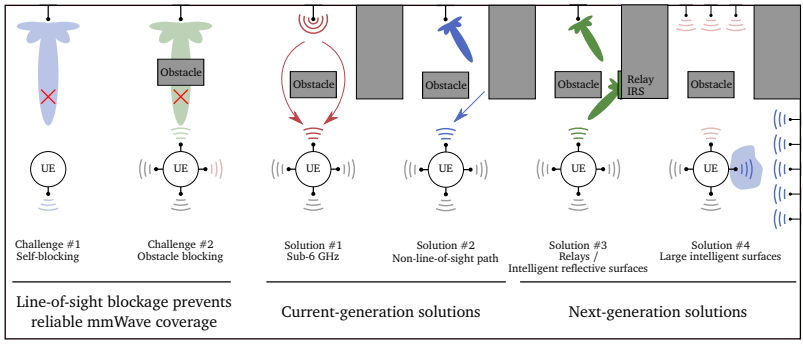

Figure 2.1: Indoor millimeter-wave (mmWave) communication: Reduced indoor mmWave coverage to the user equipment (UE) due to difficult propagation conditions, such as (self-)blocking (left), solutions to maintain wireless communication at the cost of reduced throughput and/or higher power consumption (middle), and next-generation solutions for reliable high-data-rate mmWave communication by deploying active relays, intelligent reflective surfaces (IRSs) or large intelligent surfaces (LISs) (right).

To improve link reliability in case of LoS blockage, current solutions either revert to sub-6 GHz frequencies or advanced beamforming to exploit reflections in the environment. In Figure 2.1, fallback solution #1, implemented through multi-radio-access technology (multi-RAT) and/or dual connectivity, leverages more relaxed propagation conditions at sub-6 GHz frequencies to maintain the wireless link, compromising on data rate and network capacity. Alternatively, solution #2 maintains mmWave communication by beamforming along a strong reflection via existing or intentionally deployed reflectors. Unfortunately, this increases propagation loss, requiring larger array gain or increased transmit power.

In recent years, many innovative concepts for reliable, high-data-rate wireless connectivity were proposed, such as active phased-array-based relays [4], intelligent reflective surfaces (IRS) [4], and large intelligent surfaces (LISs) [5]. Solution #3 (Figure 2.1) deploys a co-located antenna array at the access point, while judiciously distributing relays to improve coverage. These repeaters could be phased antenna arrays retransmitting an amplified version of the received signal, potentially applying intermediate (de)coding. Yet, promising advancements are being made in the field of IRS, which rely on a holographic principle to steer the retransmitted signal. Compared to

conventional phased-array-based repeaters, IRSs realize similar directivities while being less power-hungry. However, much more research is still required to practically implement this technology at mmWave frequencies [4]. Alternatively, a LIS, envisioned as an extremely large contiguous surface of electromagnetically active material, controls electromagnetic fields across a large area, implementing unprecedented energy focusing in three dimensions. This concept, illustrated by Solution #4 in Figure 2.1, makes the entire harsh and challenging environment smart to fulfill the boldest B5G and 6G requirements in terms of data rate, latency, and reliability. A controlled field across a contiguous LIS can be practically implemented by distributing a massive amount of antennas [5]. This places the UEs in the near field of the total system, enabling holographic beamforming, focusing energy at each UE and effectively suppressing inter-user interference. In general, a LIS promises exciting new features and substantial gains compared to co-located mMIMO systems [5], but also introduces significant challenges, such as efficient signal processing and low-loss distribution of broadband mmWave signals to a massive number of tightly synchronized distributed mmWave antennas, which are highly efficient, robust, and realized in a cost-effective technology compatible with large-scale deployment. This chapter analyses and demonstrates the potential of optically-enabled mmWave distributed antenna systems (DAS) to provide multi-Gbps wireless data rates to UEs in harsh indoor environments by:

- briefly reviewing the state-of-the-art in mmWave distributed antenna systems;
- proposing a novel optically-enabled mmWave architecture, consisting of a Central Office (CO), responsible for all signal processing, and ultra-low-complexity fiber-connected distributed Remote Antenna Units (RAUs);
- leveraging mmWave-over-fiber to efficiently exchange broadband mmWave signals between CO and distributed RAUs while guaranteeing tight synchronization;
- elucidating how robust and high-performance, yet low-cost and laser-free RAUs are realized by leveraging air-filled substrate-integrated-waveguide (AFSIW) technology and SiPhotonics transceivers, enabling the practical large-scale rollout of distributed mMIMO antenna systems and LISs;

- describing the crucial role of machine learning (ML) and artificial intelligence (AI) technology in broadband mmWave mMIMO antenna systems and LISs for efficient channel estimation and real-time processing of the massive amount of data;
- demonstrating the proposed architecture's potential to establish reliable multi-Gbps wireless communication with multiple collaborating distributed RAUs via an extensive measurement campaign in an anechoic setup and a realistic Industry 5.0 environment.

2.2 mmWave Distributed Antenna Systems

At mmWave frequencies, unreliable communication due to very challenging NLoS propagation conditions must be avoided by a holistic multi-disciplinary approach. We propose an optically-enabled mmWave DAS, consisting of a CO and optically fed RAUs as shown in Figure 2.2, to implement high-data-rate mmWave communication with improved coverage in harsh environments. Strategically integrating RAUs in the building infrastructure surrounding the UEs guarantees line-of-sight communication in a substantial part of the operating range. [6] theoretically shows that the total capacity of the system increases by augmenting the number of RAUs. According to the number of UEs, the target application, and the envisioned deployment environment, the required number of RAUs can then be adequately determined. Depending on the CO's architecture, the DAS enables switching between RAUs or cooperation between tightly synchronized RAUs. Selecting the RAU with the best link quality, as in the middle of Figure 2.2, reduces the CO's hardware complexity, enabling maximum hardware reuse while yielding power efficient and reliable mmWave communication, provided that hand-over is properly implemented. Yet, effective cooperation between tightly synchronized RAUs enables the realization of a distributed mmWave mMIMO setup, with each RAU equipped with an appropriate number of antennas. By increasing the number of RAUs and their number of radiating elements, a massive number of antennas is deployed around the UEs, approximating a contiguous radiating surface that practically implements the LIS-concept. Eventually, this realizes holographic beamforming (robot to the right in Figure 2.2), focusing energy in a confined three-dimensional volume around each UE [5].

Although optically-enabled DASs allow realizing a reliable cell-free high-data-rate mmWave network, several multi-disciplinary challenges remain.

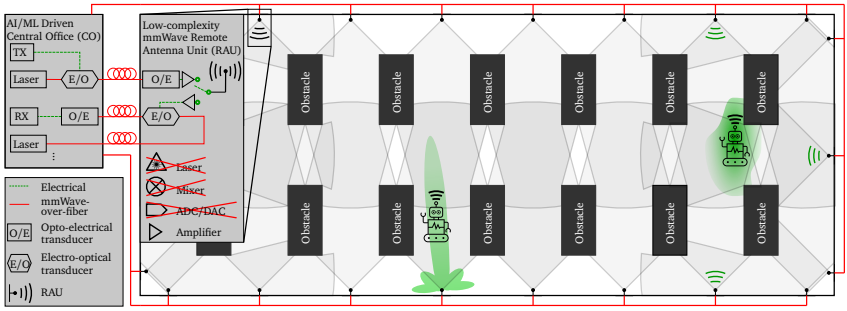

Figure 2.2: Robust, high-data-rate indoor coverage in challenging Industry 5.0 environments by a distributed antenna system. Strategic deployment always provides at least one line-of-sight path. mmWave-over-fiber enables (1) centralization of all expensive hardware at the central office, (2) scalability, (3) low-loss routing of broadband signals, and (4) tightly synchronized RAUs, essential for distributed MIMO and LIS systems.

High-performance, power-efficient, low-cost and low-complexity RAUs are vital to scale this concept to an economically viable LIS. A novel architecture should be conceived to efficiently distribute broadband mmWave signals to a large number of tightly synchronized RAUs. Finally, all signals generated and received by this massive number of radiating elements must be efficiently processed in real-time.

2.2.1 mmWave-over-fiber for Efficient Signal Distribution

The architecture in Figure 2.2 leverages the advantages of optical fiber (large bandwidth, low loss, no interference issues,...) to efficiently distribute broadband signals to a large number of RAUs. In literature, most realized DASs rely on sub-6GHz analog radio-over-fiber (ARoF) and adopt an intermediate frequency-over-fiber (IFoF) approach, with the CO providing a downconverted IF signal to each RAU. The distribution of a dedicated synchronous carrier with mixing at the RAU significantly increases its complexity. Other works [7] apply digitized-radio-over-fiber (DRoF) or sigma-delta-over-fiber (SDoF), but without achieving the same spectral efficiency and RAU simplicity as the proposed mmWave-over-fiber scheme, in which the broadband signal is directly modulated onto the optical carrier. Now, RAUs only implement opto-electrical/electro-optical conversion and amplification, while all expensive hardware remains centralized at the CO. Shifting up- and

down-conversion from RAU to CO both eliminates power-hungry mixers at the RAU and tightly synchronizes all RAUs, enabling distributed mMIMO and LIS implementations. Still, this requires high-speed opto-electronic devices and entails chromatic dispersion fading in the fiber [8]. To realize a highly efficient transceiver for mmWave-over-fiber communication, a high-speed ISIPP50G silicon-photonic photodetector and electroabsorption modulator were co-optimized and compactly integrated with dedicated GaAs amplifiers to maximize power transfer within the targeted mmWave frequency band [8]. Yet, even faster opto-electric transducers are actively researched, currently reporting devices with sub-THz bandwidths [9]. Here, we leverage the link in [8] together with low-complexity and cost-effective RAUs to realize a scalable mmWave DAS. To increase the number of RAUs, while providing every RAU with a dedicated signal, required for next generation mMIMO or LIS systems to serve a large number of users, one may adopt a star configuration, with a dedicated point-to-point fiber link from the CO to each RAU, or a ring configuration, with wavelength division multiplexing (WDM) and optical filtering. At lower mmWave frequencies and with standard fibers, chromatic dispersion fading only becomes problematic after kilometers of fiber, which is typically not encountered in indoor environments. Yet, if longer fiber connections are needed, as in large factories of the future, or operation at higher mmWave frequencies is targeted, this problem can be countered by optical single sideband architectures [8]. Figure 2.2 shows that such a bi-directional time-division-duplex (TDD) mmWave-over-fiber link yields a distributed mmWave antenna system that overcomes LoS-blocking, as required to meet the very challenging specifications of future-generation applications in realistic environments.

2.2.2 Cost-Effective and High-Performance Remote Antenna Units

Robust and high-performance, yet cost-effective RAUs are of major importance in the rollout of large-scale distributed mMIMO systems and LISs. The mmWave-over-fiber architecture already eliminates up- and downconverters at the RAU and local oscillator (LO) signal distribution. Shifting the laser for uplink communication to the CO further reduces RAU complexity, cost and power consumption, only implementing electro-optical conversion, amplification, and radiation [8]. With all expensive hardware located at the CO, the laser-free RAUs efficiently reuse this equipment in case only a subset of RAUs is active. AFSIW technology is put forward as a prime

candidate for photonic-enabled antenna systems as efficient, broadband mmWave antenna integration platform, facilitating compact integration of all required RF amplifiers and opto-electronic transducers [10]. Highly efficient, robust multi-antenna systems may be realized in low-cost lossy substrates, such as FR4, silicon, cork, ABS and particle board through standard fabrication technology [3]. By exploiting metallized air cavities, dielectric losses are eliminated, yielding unprecedented radiation efficiencies. Furthermore, surface waves are blocked, enabling compact arrays with low mutual coupling, stable radiation patterns, and high antenna-to-integration-platform isolation, providing robust stable performance in harsh environments. Therefore, the antenna elements and array proposed in [3] are deployed at the UE and RAU in all presented experiments. To exploit this technology in the higher mmWave bands and beyond with a performance comparable to that in the lower mmWave frequency bands, further research on silicon micromachining, 3D printing and PCB manufacturing [11] is needed. Silicon micromachining provides precise fabrication, yet currently lacks the potential to integrate active electronics or photonics. Implementing AFSIW in PCBs at higher frequencies requires custom stack-ups. This provides a more cost-effective and lower-loss alternative to dielectric-filled SIW antennas. Moreover, advancements in 3D printing and surface-roughness-reducing treatments also provide opportunities to realize competitive antennas, but more research is needed to efficiently integrate active circuitry.

2.2.3 Machine-learning for large-scale mmWave DAS

In B5G and 6G wireless communication networks, machine learning (ML) will be exploited at each abstraction layer to predict users/services demands and evolution of the wireless channel to conceive self-optimizing and self-updating networks. Specifically for broadband mmWave cell-free distributed mMIMO systems and LISs, traditional multi-antenna signal processing techniques no longer suffice due to the massive number of radiating elements, the extreme data rates and ever-increasing number of mobile users. In contrast to conventional approaches, which require excessive computational power and lead to unacceptable latencies, deep-learning-based approaches that exploit inherent channel sparsity to efficiently precode and modulate the data onto multiple streams towards the distributed RAUs have shown near-optimal effective data rates at significantly lower computational complexity for coordinated distributed beamforming systems [12], cell-free distributed mMIMO systems [13] and LISs [14].

2.3 Providing Robust and High Data Rate Coverage

We now experimentally demonstrate the mmWave-over-fiber-based DAS's potential to generate high-data-rate wireless mmWave links at symbol rates of 3 GBd and 6 GBd. The setup in Figure 2.3 was first deployed in a controlled anechoic chamber environment. A metal cylinder with a diameter of 25 cm and height 30 cm, resembling the body of a robot, serves as UE. Fujitsu H74M-5208 lithium niobate Mach-Zehnder Modulators (MZMs) perform the electro-optical transduction in both downlink and uplink, while the photoreceiver in [8] implements the opto-electric conversion. An optical laser power of 10 dBm and fibers of 20 m are used. At the RAU, a 1x4 corporate-fed (24.25-29.5) GHz AFSIW antenna array [3], with a peak gain of 10.1 dBi at broadside, is applied. At the UE, a single antenna of the same topology, with 7.4 dBi peak gain and 70° half-power beamwidth, is deployed on the metal shaft [3]. A variable-gain amplifier (HMC943APM5E) ensures a constant transmit power of 20 dBm to overcome losses due to the wireless path of 2 m. Link quality in our setup is evaluated through the root-mean-square error vector magnitude (EVM), after zero-forcing (ZF) equalization over a QPSK symbol stream, quantifying the discrepancy between received and transmitted symbols and the symbols in the transmitted constellation. According to 3GPP, reliable transmission of QPSK, or higher-order 16-QAM or 64-QAM symbols requires an EVM below 17.5 %, 12.5 % and 8 %, respectively [15]. The baseband symbols, generated by a Keysight M8195 arbitrary wave form generator, are upconverted by Analog ADMV1013 mixers to an RF carrier of 26.5 GHz. At the receiver, the signal is sampled by a Lecroy LabMaster 10Zi-A real-time oscilloscope. Next, the EVM is calculated in post-processing, selecting part of the symbol stream as pilot symbols. The mmWave-over-fiber link does not pose any condition on the applied symbol constellation, making the link signal-transparent. Therefore, the architecture supports 5G signals and is future-proof. Across the different experiments, we stress the different challenges that were resolved and point out remaining pitfalls.

2.3.1 High-Data-Rate Bi-directional Fiber-Wireless Link

First, the above wireless mmWave-over-fiber setup implements bi-directional multi-Gbps communication between one antenna on the UE, and a four-antenna-element RAU. Figure 2.3 shows the link quality. Because of the highly efficient directional antenna systems, guaranteeing robust performance

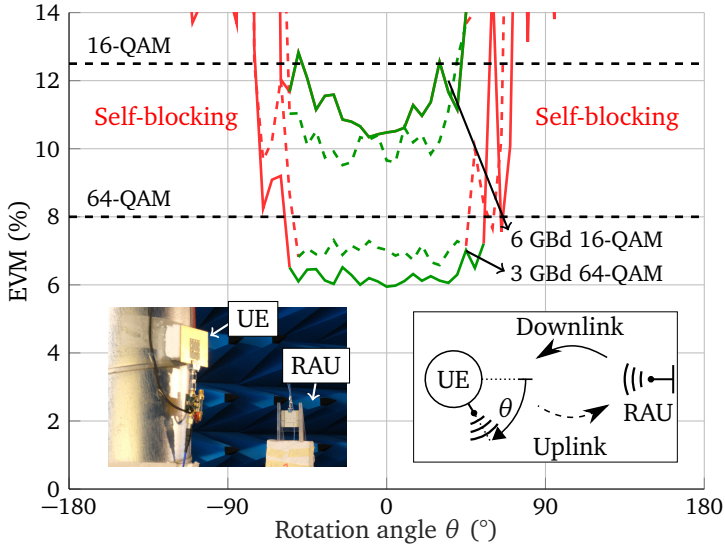

Figure 2.3: Measurement of bi-directional fiber-wireless mmWave link supporting 24 Gbps or 18 Gbps in line-of-sight conditions. Self-blocking prevents high-data-rate mmWave communication.

on the robot platform, and the dedicated photoreceiver design, a 6 GBd signal can be supported, providing 24 Gbps in both uplink and downlink. While ensuring sufficient link budget, even after deployment on a conducting platform or human body, the mmWave link is only maintained over a field of view of 90° due to the metallic cylinder and the antenna directivity. A reduced symbol rate of 3 GBd still achieves a data rate of 18 Gbps (64-QAM) [15], showcasing a TDD half-duplex bi-directional link providing multi-Gbps communication using mmWave-over-fiber and cost-effective, highly efficient custom RAUs. While this experiment used dedicated fibers for up- and downlink, the approach in [8] can be leveraged for bidirectional transmission over a single fiber, facilitating the interconnection of a large number of RAUs for large-scale deployment. Still, the link remains unreliable due to self-blocking. Since up- and downlink communication yield very similar performance, the remainder of the measurement analysis focuses on downlink communication.

2.3.2 Solving Self Blocking

Spatial diversity solves self-blocking by deploying multiple antennas on the UE or installing several RAUs in the room to form a DAS. For the former, selection combining with four antennas maintains the 24 GBps link for almost all rotations, significantly mitigating self-blocking. However, in the hand-over regions, the EVM exceeds the 12.5 %-threshold for 16-QAM modulation, which can be resolved by upscaling the number of antennas at the UE, performing analog beamforming at the RAU or exploiting equal gain or maximum ratio combiners. Alternatively, reducing the baudrate to 3 GBd achieves a steady data rate of 18 Gbps without degradation due to self-blocking. For the latter, similar findings were found when distributing three RAUs around the targeted UE. When the link quality towards a particular RAU drops below a set threshold, another RAU takes over. This approach also further reduces the CO complexity through hardware re-use. In general, this experiment shows that self-blocking can either be solved by applying spatial diversity at the UE or through a DAS. Yet, the number of UE antennas and RAUs should be tailored to the application, environment and the antenna topologies used at the UE and RAU. Furthermore, the largest pitfall of this setup remains shadowing by external static or dynamic obstacles obstructing the LoS-path.

2.3.3 Solving Shadowing and Increasing Link Capacity

To overcome LoS-blocking effects, UE spatial diversity should be combined with a DAS. After detailed analysis of the targeted environment and potential UE locations, multiple RAUs are strategically distributed and the UEs are equipped with a suitable number of antennas. Drops in link quality, either due to self-blocking or an external static or dynamic blocker, are then resolved by simply selecting the best-positioned RAU and UE-antenna, as in Figure 2.2 (middle). Conceptually, this approach closely relates to coordinated multi-point (CoMP) techniques, first introduced in LTE release 11, where multiple coordinating transmission/reception points (TRPs) serve a UE. Specifically, it is similar to dynamic point selection, where the TRP offering the best channel conditions connects to the UE. Although originally proposed to mitigate interference and improve throughput at the cell edge, CoMP techniques will be leveraged in future 5G systems to enhance reliability in challenging propagation conditions. Moreover, when ensuring tight synchronization among all RAUs, as in our setup, multiple RAUs can collaborate to further improve performance, such as UE data rate. In Figure 2.5, two cooperating RAUs transmit two simultaneous data streams to an UE

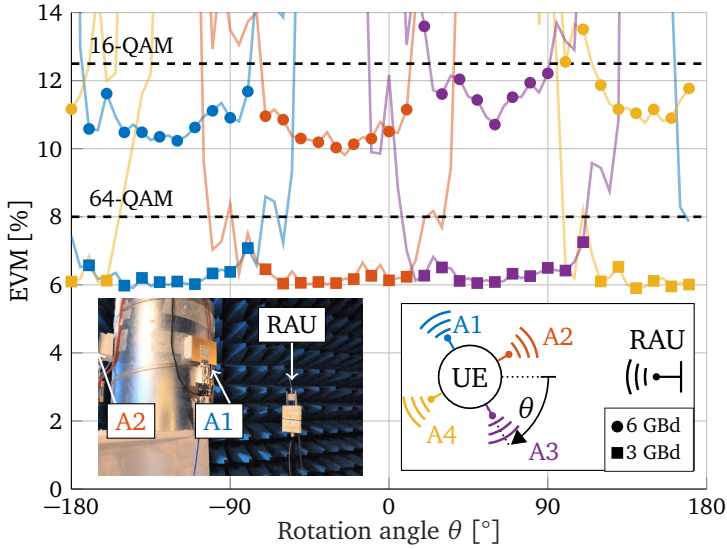

Figure 2.4: Self-blocking problem resolved: Measurement of spatial diversity at user equipment (UE) ensures 24 Gbps (6 GBd) or 18 GBps (3 GBd) over 360° by combining signals at Antennas 1, 2, 3 and 4 (A1, A2, A3 & A4).

equipped with four antennas, at a symbol rate of 3 GBd or 6 GBd. At the UE, both data streams are recovered properly, resulting in a data rate of 36 Gbps or 48 Gbps, respectively, for all rotation angles of the UE. Again, conceptually, this compares to CoMP joint transmission mode. Whereas our synchronized architecture enables coherent beamforming, LTE has no plans for such features. Hence, an optically-enabled DAS, combined with UE spatial diversity not only offers a very promising path towards robust mmWave coverage in challenging environments, mitigating the effects of LoS blockage, but also boosts wireless data rates to unprecedented levels through distributed MIMO techniques.

2.4 Workplace Environment

After validation in an anechoic environment, our optically-enabled DAS was deployed in a lab environment with 4-m-high ceilings, concrete floors, metal walls and metal racks, mimicking the harsh environments encountered in Industry 5.0 applications, to demonstrate robust, high-data-rate coverage in a realistic environment. The measurement setup (Figure 2.6) consists of two

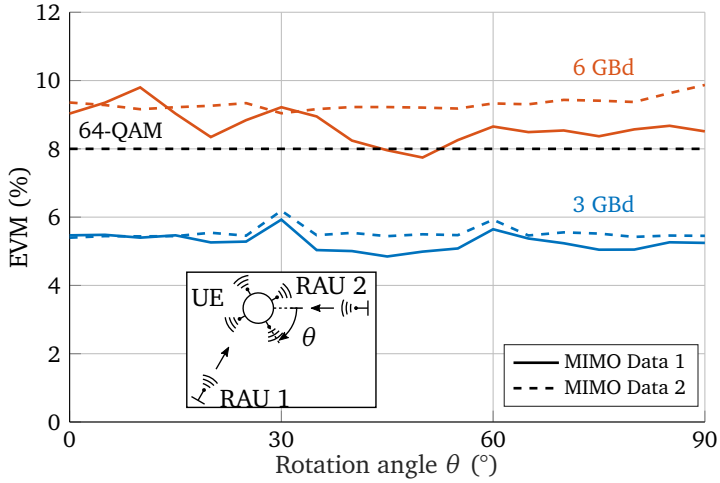

Figure 2.5: Increased data rate through distributed MIMO: 48 Gbps measurement without self-blocking.

RAUs, at both ends of a corner, formed by metal walls, communicating with a metal cylindrical robot, equipped with four antennas. The robot is then positioned at seven different locations, at 0.5 m intervals, in between both RAUs. The link quality between RAU 1 and the UE, which applies selection combining, gradually deteriorates due to increasing path loss. Once the robot turns around the corner, the link quality drops significantly. A similar behavior is observed when only RAU 2 is active and the robot moves from position #7 to #1. Hence, by deploying these RAUs in this complementary way, a stable connection of 24 Gbps is maintained along the track, thereby fully resolving shadowing by the corner. Additionally, at position #4, two data streams were sent to the UE by leveraging distributed MIMO techniques at both cooperating RAUs. At the UE, both streams were recovered, achieving an EVM below 10 % (Figure 2.6), thereby doubling the data rate to 48 Gbps (two 16-QAM 6 GBd data streams). Hence, our approach provides stable high-data-rate coverage in harsh and challenging real-life environments, typically encountered in industrial settings. Moreover, through tight synchronization between the distributed RAUs, MIMO techniques increase wireless data rates even further. Yet, to fully unleash the potential of optically-enabled mmWave DAS, many challenges still remain. The highly complex environments and the large number of parameters and expected users need advancements in ML to determine the optimal positions of RAUs in real-life environments and the

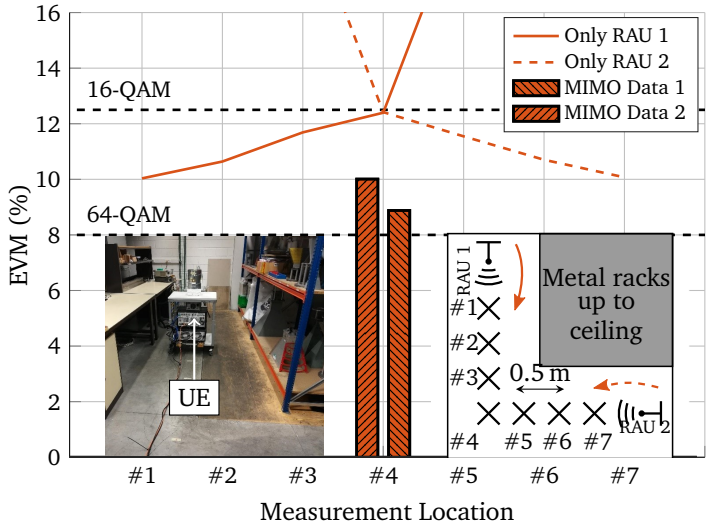

Figure 2.6: Robust mmWave coverage ensuring 24 Gbps at every position by RAU selection. Throughput at position #4 doubled to 48 Gbps by distributed MIMO. Adjacent measurement positions spaced 0.5 m.

optimal number of antenna elements at each RAU and UE, to efficiently estimate the channel and to perform ultrafast precoding of all data streams to a large number of RAUs in real time, providing these high data rates in dynamic application scenarios. In this process, the impact of next-generation compression techniques on wireless data rates and latency should be analyzed. First, the generation and collection of large, accurate, real-world datasets, gathered within the small coherence time of the highly mobile users, is of major importance to further develop robust and efficient ML algorithms. Second, dedicated AI hardware is needed to efficiently implement these ML/AI techniques to process massive amounts of data at both CO and UE, within stringent latency constraints at an acceptable power level. It is important that (1) a hardware-algorithm co-design strategy is adopted for hardware-aware algorithms and algorithm-friendly transceiver structures, and that (2) a modular architecture enables reuse of AI hardware in the UE and a scaled-up version in the CO. Third, synchronized ML procedures in each layer, and not only the PHY layer, will fully exploit the potential of ML and ensure highly secure data transfer. Moreover, higher level of integration at the RAU side should also be pursued.

2.5 Conclusion

The potential of mmWave-over-fiber distributed antenna systems (DAS) for simultaneous reliable high-data wireless communication in future generation networks was demonstrated. Such a DAS is highly scalable owing to centralized processing and low-complexity, high-performance, laser-free remote antenna units (RAUs) composed of co-optimized opto-electric components and highly efficient air-filled substrate-integrated-waveguide antennas. Strategic distribution and integration of tightly synchronized RAUs in the user equipments' environment enables the rollout of a distributed mMIMO system or a large intelligent surface. Measurements in a controlled anechoic chamber and a realistic environment, resembling an Industry 5.0 setting, show the potential of optically-enabled DAS architectures, establishing and maintaining multi-Gbps wireless communication, while resolving self-blocking and line-of-sight blockage issues. Our current setup obtains wireless data rates up to 24 Gbps by selecting the RAU with the best link quality, while achieving wireless data rates up to 48 Gbps through distributed MIMO techniques. However, large scale, efficient real-time signal processing and a suitable distribution of RAUs remain of major importance for practical rollouts in high-data-rate, low-latency and maximal-coverage communication environments, as such fulfilling the boldest B5G requirements. Machine learning forms a promising technology to tackle these challenges.

References

[1] M. Matthaiou, O. Yurduseven, H. Q. Ngo, D. Morales-Jimenez, S. L. Cotton, and V. F. Fusco, "The Road to 6G: Ten Physical Layer Challenges for Communications Engineers", *IEEE Commun. Mag.*, vol. 59, no. 1, pp. 64–69, 2021.

[2] M. Giordani, M. Polese, M. Mezzavilla, S. Rangan, and M. Zorzi, "Toward 6G Networks: Use Cases and Technologies", *IEEE Commun. Mag.*, vol. 58, no. 3, pp. 55–61, 2020.

[3] I. Lima de Paula, S. Lemey, D. Bosman, *et al.*, "Cost-effective high-performance air-filled SIW antenna array for the global 5G 26 GHz and 28 GHz bands", *IEEE Antennas Wireless Propag. Lett.*, vol. 20, no. 2, pp. 194–198, Feb. 2021.

[4] M. Di Renzo, A. Zappone, M. Debbah, *et al.*, "Smart Radio Environments Empowered by Reconfigurable Intelligent Surfaces: How It Works, State of Research, and The Road Ahead", *IEEE J. Sel. Areas Commun.*, vol. 38, no. 11, pp. 2450–2525, Nov. 2020.

[5] S. Hu, F. Rusek, and O. Edfors, "Beyond Massive MIMO: The Potential of Data Transmission With Large Intelligent Surfaces", *IEEE Trans. Signal Process.*, vol. 66, no. 10, pp. 2746–2758, 2018.

[6] E. Björnson and L. Sanguinetti, "Scalable cell-free massive MIMO systems", *IEEE Trans. Commun.*, vol. 68, no. 7, pp. 4247–4261, 2020.

[7] L. Breyne, G. Torfs, X. Yin, P. Demeester, and J. Bauwelinck, "Comparison Between Analog Radio-Over-Fiber and Sigma Delta Modulated Radio-Over-Fiber", *IEEE Photon. Technol. Lett.*, vol. 29, no. 21, pp. 1808–1811, Nov. 2017.

[8] L. Bogaert, J. Van Kerrebrouck, H. Li, *et al.*, "SiPhotonics/GaAs 28-GHz Transceiver With Reflective EAM for Laser-Less mmWave-Over-Fiber", *J. Lightw. Technol.*, vol. 39, no. 3, pp. 779–786, 2021.

[9] M. He, M. Xu, Y. Ren, *et al.*, "High-performance hybrid silicon and lithium niobate Mach–Zehnder modulators for 100 Gbit s^{-1} and beyond", *Nat. Photon.*, vol. 13, no. 5, pp. 359–364, 2019.

[10] Q. Van den Brande, S. Lemey, S. Cuyvers, *et al.*, "A Hybrid Integration Strategy for Compact, Broadband, and Highly Efficient Millimeter-Wave On-Chip Antennas", *IEEE Antennas Wireless Propag. Lett.*, vol. 18, no. 11, pp. 2424–2428, 2019.

[11] B. Zhang, W. Chen, K. D. Yanjie Wu, and R. Li, "Review of 3D Printed Millimeter-Wave and Terahertz Passive Devices", *Int J. Antennas Propag.*, 2017.

[12] A. Alkhateeb, S. Alex, P. Varkey, Y. Li, Q. Qu, and D. Tujkovic, "Deep Learning Coordinated Beamforming for Highly-Mobile Millimeter Wave Systems", *IEEE Access*, vol. 6, pp. 37 328–37 348, 2018.

[13] Y. Jin, J. Zhang, S. Jin, and B. Ai, "Channel Estimation for Cell-Free mmWave Massive MIMO Through Deep Learning", *IEEE Trans. Veh. Technol.*, vol. 68, no. 10, pp. 10 325–10 329, 2019.

[14] A. Taha, M. Alrabeiah, and A. Alkhateeb, "Enabling Large Intelligent Surfaces With Compressive Sensing and Deep Learning", *IEEE Access*, vol. 9, pp. 44 304–44 321, 2021.

[15] 3GPP, *LTE; Evolved Universal Terrestrial Radio Access (E-UTRA); Base Station (BS) radio transmission and reception - Release 15 - v 15.3.0*, Tech. Rep. TR 36.104, Jan. 2021. [Online]. Available: `https://www.3gpp.org/dynareport/36-series.htm`.

3

Enhancing Reliability in multi-Gbps Fiber-Wireless Communication Links

Based on "mmWave-over-Fiber Distributed Antenna Systems for Reliable multi-Gbps Wireless Communication" by Arno Moerman, Joris Van Kerrebrouck, Olivier Caytan, Igor Lima de Paula, Laurens Bogaert, Guy Torfs, Piet Demeester, Marc Moeneclaey, Hendrik Rogier and Sam Lemey, as presented on the URSI AT-AP-RASC Conference, Gran Canaria, 2022.

Recent technological advancements in the field of antenna design and microwave photonics have paved the way for broadband and efficient mmWave-over-fiber distributed antenna systems. In this work, we discuss the practical realization and measurement setup of a mmWave-over-fiber link and tackle the unfavorable propagation conditions that arise at mmWave frequencies. First, we demonstrate a 24 Gbps fiber-wireless link through the use of highly efficient and robust air-filled substrate-integrated-waveguide antennas and a custom co-designed photoreceiver with low-noise amplifier. Next, we deploy multiple antennas at the user equipment and analyze various combining methods to mitigate the self-blocking problem arising at these frequencies. To demonstrate its potential in harsh real-life environments, a mmWave-over-fiber distributed antenna system is set up in an environment resembling an Industry 5.0 workplace. We showcase how this system solves self-blocking and other problems that arise when the line-of-sight path is blocked. Moreover, by leveraging two tightly-synchronized remote antenna units distributed MIMO techniques double the channel capacity to 48 Gbps.

3.1 Introduction

The mmWave (30 GHz-300 GHz) frequency band is a key enabler for the Internet of Everything (IoE) in the (beyond-)5G era. Next-generation IoE applications, such as cyber-physical systems in Industry 5.0 and immersive multisensory interactive augmented and virtual reality, require enhanced mobile broadband (eMBB) access at ultra-low latency and high reliability. mmWave frequencies, however, suffers from increased path loss, higher penetration loss, and significant shadowing. Yet, their short wavelengths enable compact integration of multiple antenna elements to form highly-directive co-located antenna arrays that are capable of overcoming the higher path loss. However, such an approach is still prone to non-line-of-sight (NLoS) problems, such as shadowing or self-blocking. Different solutions have been proposed in case these unfavorable propagation conditions arise. Falling back to sub-6 GHz or exploiting a strong reflected path, either created by placing intentional reflectors or by exploiting existing reflections in the environment, compromises on link capacity and quality, respectively. Recently, some innovative solutions to provide reliable, high-data-rate wireless communication were proposed, such as the deployment of intelligent reflective surfaces (IRSs) at strategic positions in the user equipments' (UE) environment [1], or the exploitation of a large intelligent surface (LIS) [2]. The latter can be seen as a large contiguous surface filled with electromagnetic radiators surrounding the UE. This places the UE in the LIS's near field, enabling unprecedented energy focusing in three dimensions. Furthermore, [3] advocates the use of mmWave-over-Fiber distributed antenna systems (DAS) to provide high throughput and reliable coverage. Here, multiple antennas are distributed in the UEs' environment while a central office (CO) directly distributes the mmWave signal over fiber towards the different antennas. The major advantages of using mmWave-over-fiber are (1) the low-loss distribution of broadband mmWave signals, (2) the inherent potential to synchronize different remote antenna units (RAUs), and (3) cost-effective and relative simple RAUs, which only need to perform opto-electrical conversion, amplification, and potentially RF beamforming. Additionally, this approach enables the practical realization of the aforementioned LIS concept [3]. [4] compares mmWave-over-fiber to other fiber-wireless distribution options in a DAS.

In Section 3.2, a technical overview is given of the measurement setup for a single mmWave-over-fiber wireless link. Section 3.3 leverages multiple antennas at the UE to solve self-blocking problems in an anechoic environment.

Finally, in Section 3.4, a DAS is built in a realistic environment encountered in future applications. The DAS deploys two fiber-wireless links to increase the total throughput of the system by leveraging distributed MIMO (DMIMO) techniques.

3.2 Measurement Setup Overview

Figure 3.1 depicts a technical overview of the measurement setup of a single mmWave-over-fiber downlink, consisting of the equipment at the CO, a RAU, and the UE. At the CO, a 65 Gsps Keysight M8195 arbitrary waveform generator (AWG) generates the electrical baseband signals, which are upconverted to a 26.5 GHz carrier with an Analog ADMV1013 quadrature mixer. The other parts of the setup, including the mmWave-over-fiber link, the RAU and UE architecture, as well as the post-processing, are identical to the setup in Chapter 2.

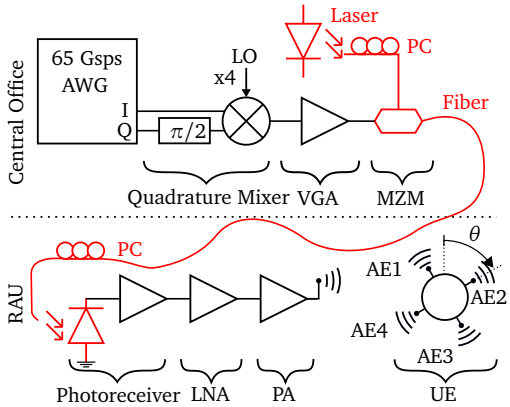

Figure 3.1: Measurement setup containing central office, remote antenna unit (RAU), arbitrary waveform generator (AWG), Mach-Zehnder modulator (MZM), polarization controller (PC), and the rotating user equipment (UE), equipped with four receiving antenna elements (AEs).

Both the UE and the RAU can be seen in Figure 3.2 in the anechoic environment. The metal shaft is able to rotate and is placed at a distance of 2 m from the RAU. The technical overview and the results in the remainder of this chapter are only discussed in downlink communication, as we have shown that the fiber-wireless uplink features similar performance [3].

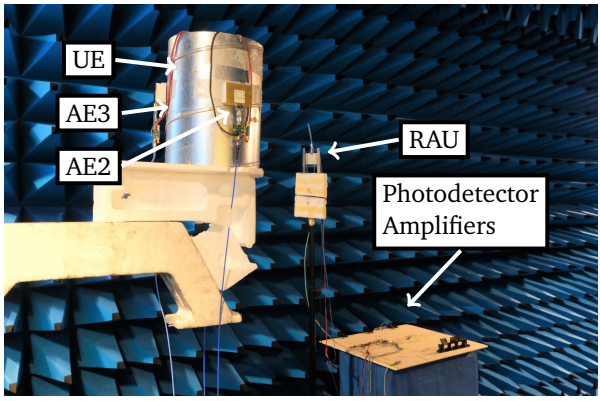

Figure 3.2: Picture of the measurement, showing the user equipment (UE) with two out of four antenna elements (AEs), the remote antenna unit (RAU), and the electronics.

As a baseline performance measurement, the single link as depicted in Figure 3.1, is tested in an anechoic environment for modulated signals with baud rates from 2 GBd up to 7 GBd. Figure 3.3 shows the rms EVM received at a single UE antenna as a function of the rotation angle of the UE. Independent from the baudrate, the link quality drastically reduces for $|\theta| > 45°$, caused by the 70° half-power beamwidth of the deployed AFSIW antennas, and the metal integration platform causing self-blocking. In the region of good coverage, the (2–4) GBd and (5–6) GBd signals result in data rates of (12–24) Gbps and (20–24) Gbps, respectively. The limited bandwidth of the total system, both caused by the co-optimized photoreceiver [5] and the antenna characteristics [6], yields an unusable link for signals with a symbol rate larger than 7 GBd (corresponding to a total bandwidth of 9.45 GHz due to the root-raised cosine filtering).

3.3 Spatial Diversity at the User Equipment

By deploying four antennas at the UE (Figure 3.1) and spacing them equally, good link quality over 360° is guaranteed without self-blocking because of the 90° coverage of one antenna and the spatial diversity that is introduced. Figure 3.4 shows the rms EVM of the received signals for the four different antennas as a function of the UE's rotation angle, for a 3 GBd and 6 GBd symbol

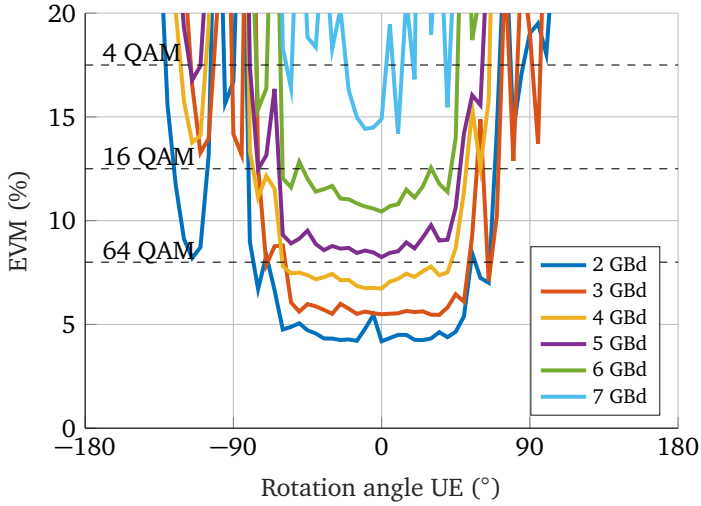

Figure 3.3: Root mean square error vector magnitude (rms EVM) for the downlink mmWave-over-fiber link when only one antenna is deployed on the UE (AE1).

rate. The solid line indicates the rms EVM value when the best possible link is selected, by applying selection combining (SC). This results in complete coverage with a symbol rate of 3 GBd. However, for a symbol rate of 6 GBd, the EVM exceeds the threshold for reliable transmission of 16-QAM symbols at the handover regions. With SC, the receiver only demodulates the signal received by the antenna that provides the best link quality and the energy received at the other antennas remains unused. At the handover regions, this issue can be resolved by adopting maximum ratio combining (MRC). In that case, the received signals are weighted with respect to their link quality and then summed. This guarantees an rms EVM below 12.5 % over 360° for the 6 GBd symbol rate (dashed line), leading to a stable 24 Gbps wireless link without self-blocking effects.

3.4 DMIMO in Realistic Environment

Previous measurements have already resolved the self-blocking problem in an anechoic environment by spatial diversity at the UE together with adequate combining techniques. In real-life scenarios, other NLoS problems may still

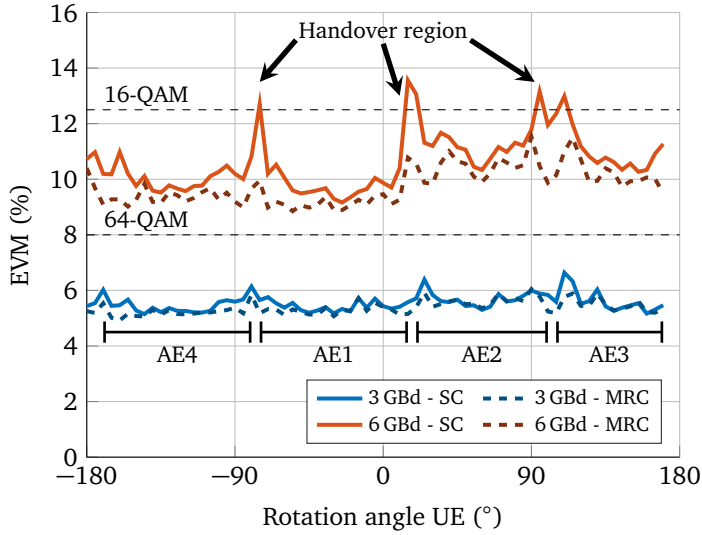

Figure 3.4: EVM as a function of the UE's rotation angle for a symbol rate of 3 GBd and 6 GBd, when deploying four antenna elements (AEs) at the UE. Selection combining (SC) guarantees a stable 18 Gbps wireless link (64-QAM at 3 GBd), while maximum ratio combining (MRC) guarantees a stable 24 Gbps wireless link (16-QAM at 6 GBd).

occur (such as line-of-sight blocked by another user or a metal rack). An appropriate amount of RAUs distributed in the environment can tackle this problem. When LoS between a RAU and UE is blocked, the CO can direct the mmWave signal to a RAU with LoS to the target UE. In addition, this approach also paves the way towards distributed MIMO (DMIMO) and holographic beamforming.

To demonstrate the potential of this mmWave-over-fiber DAS, two RAUs are now deployed in our lab, mimicking the harsh propagation conditions of an Industry 5.0 environment. Figure 3.5 shows the CO and the mmWave-over-fiber links to both RAUs and the measurement setup in the lab is the same as in Chapter 2.

In the first measurement, the UE is moved from position #1 to #7 with only RAU 1 active. Figure 3.6 shows the performance along the track for a symbol rate of 3 GBd and 6 GBd, for both SC and MRC. Although MRC extends the link quality up to location #5, if the UE is beyond the metal rack at positions

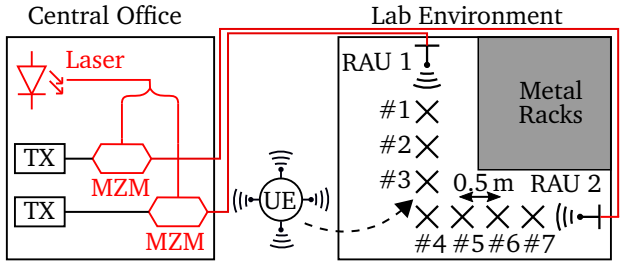

Figure 3.5: Measurement setup in our lab, representing a realistic propagation environment.

#6 and #7, the LoS path is blocked and no usable signal is received.

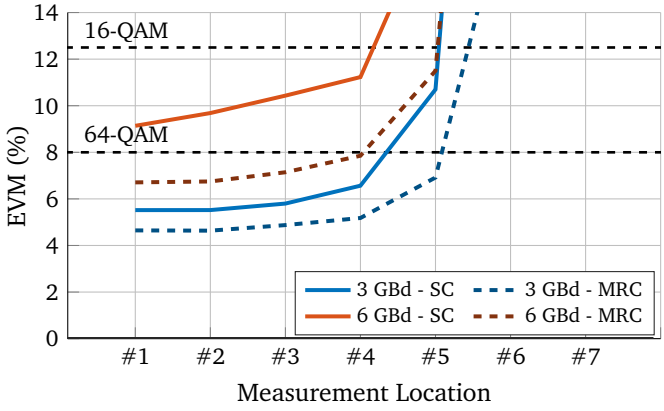

Figure 3.6: Selection combining (SC) and maximum ratio combining (MRC) in a realistic environment (Figure 3.5).

In Figure 3.7, the complementary link quality is also shown (dashed line) for the UE moving from location #7 to #1 when only RAU 2 is active and SC is applied. Notice that this indeed allows switching between RAUs in case of blocking and, hence, increasing reliability and providing a stable link of 18 Gbps and 24 Gbps for symbol rates of 3 GBd and 6 GBd, respectively.

Additionally, when the UE is located in a region where both RAUs provide a good link, such as in location #4, DMIMO techniques can be exploited to increase the total system throughput. In the measurement, both RAUs simultaneously transmit a signal with a different PRBS data stream. Part of

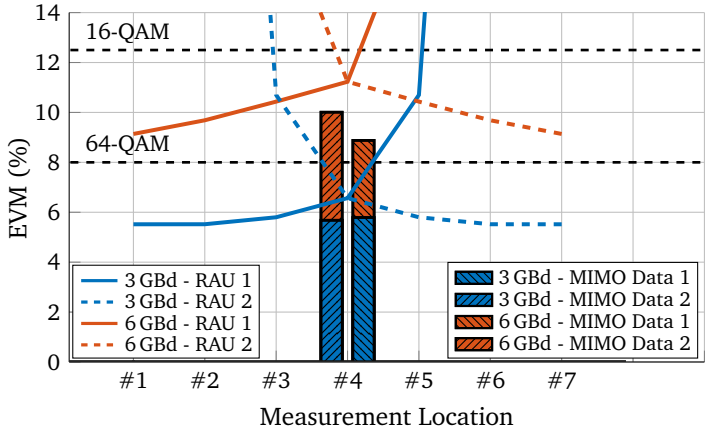

Figure 3.7: At location #4, where both remote antenna units (RAUs) have line-of-sight, double throughput is achieved leveraging distributed MIMO techniques.

both streams consists of known pilot symbols, which allows the UE to separate the signals coming from RAU 1 and RAU 2. Both streams are well below the 3GPP threshold for both 3 GBd and 6 GBd. Due to the distribution of RAUs and the spatial diversity created at the UE, the mmWave-over-fiber DAS realizes a double throughput of 36 Gbps and 48 Gbps for symbol rates of 3 GBd and 6 GBd, respectively.

3.5 Conclusion

This contribution described a measurement setup for a mmWave-over-fiber distributed antenna system. First, the baseline performance of a single fiber-wireless link is characterized, yielding a fiber-wireless data rate of 24 Gbps. This is achieved by leveraging the highly efficient air-filled substrate-integrated-waveguide antenna platform, previously published in [6], and the custom co-designed photoreceiver and low noise amplifier. To solve the inherent self-blocking problem in Industry 5.0 applications, combining methods, such as selection combining and maximum ratio combining, are exploited. Finally, two remote antenna units (RAUs) are deployed to form a mmWave-over-fiber distributed antenna system in combination with multiple antennas at the user equipment (UE). This experiment in a harsh real-life

environment showed that combining methods and switching between RAUs can resolve self-blocking and other non-line-of-sight problems. In case both links have a stable connection to the UE, the channel capacity can be increased by leveraging distributed MIMO. Future research will focus on increasing the number of RAUs and UEs. In the process, we will explore optimal placement of the RAUs, and optimal number of antenna elements per RAU. This will eventually pave the way towards the practical realization of a large intelligent surface.

References

[1] Q. Wu and R. Zhang, "Towards Smart and Reconfigurable Environment: Intelligent Reflecting Surface Aided Wireless Network", *IEEE Communications Magazine*, vol. 58, no. 1, pp. 106–112, 2020.

[2] S. Hu, F. Rusek, and O. Edfors, "Beyond Massive MIMO: The Potential of Data Transmission With Large Intelligent Surfaces", *IEEE Transactions on Signal Processing*, vol. 66, no. 10, pp. 2746–2758, 2018.

[3] A. Moerman, J. Van Kerrebrouck, O. Caytan, *et al.*, "Beyond 5G Without Obstacles: mmWave-over-Fiber Distributed Antenna Systems", *IEEE Communications Magazine*, vol. 60, no. 1, pp. 27–33, 2022.

[4] L. Breyne, G. Torfs, X. Yin, P. Demeester, and J. Bauwelinck, "Comparison Between Analog Radio-Over-Fiber and Sigma Delta Modulated Radio-Over-Fiber", *IEEE Photon. Technol. Lett.*, vol. 29, no. 21, pp. 1808–1811, Nov. 2017.

[5] L. Bogaert, J. Van Kerrebrouck, H. Li, *et al.*, "SiPhotonics/GaAs 28-GHz Transceiver With Reflective EAM for Laser-Less mmWave-Over-Fiber", *J. Lightw. Technol.*, vol. 39, no. 3, pp. 779–786, 2021.

[6] I. Lima de Paula, S. Lemey, D. Bosman, *et al.*, "Cost-effective high-performance air-filled SIW antenna array for the global 5G 26 GHz and 28 GHz bands", *IEEE Antennas Wireless Propag. Lett.*, vol. 20, no. 2, pp. 194–198, Feb. 2021.

4

System-Level Simulation Suite for the Design of mmWave-over-Fiber-based Distributed Antenna Systems

Based on "System-Level Simulation Suite for the design of mmWave-over-Fiber-based Distributed Antenna Systems" by Arno Moerman, Olivier Caytan, Laura Van Messem, Joris Van Kerrebrouck, Guy Torfs, Piet Demeester, Hendrik Rogier and Sam Lemey, as submitted in Transactions on Microwave Theory and Technique.

Although challenging propagation conditions reduce its reliability, the mmWave spectrum is considered a cornerstone of (beyond-)5G networks. Recently, distributed antenna systems (DASs) surrounding the mobile users with multiple remote antenna units (RAUs) interconnected by mmWave-over-fiber technology were identified as a prime candidate to unlock high throughput and reliable coverage. This chapter proposes a dedicated simulation suite facilitating the deployment of such a mmWave-over-fiber-based DAS by accurately predicting system-level performance and enabling time-efficient optimization of the hardware configuration, including the RAUs, the central office (CO) and the signal processing units, towards the target application. It incorporates accurate models for the mmWave-over-fiber link and the amplifiers, including non-linear distortion and noise, full-wave electromagnetic models for the antenna front-ends, and analytical models for the wireless channel. The simulation suite is validated by a measurement campaign, not only focusing on a single mobile user served by a fixed-beam RAU, but also considering a multi-beam RAU serving two users simultaneously by means of two independent mmWave-over-fiber links. The model accurately predicts up- and downlink quality over a wide range of user positions, different system parameters, and also accurately captures inter-user interference.

4.1 Introduction

The coming generations of mobile networks aim to realize the Internet of Everything (IoE), providing a large number of users and devices high-performance wireless access well beyond the capabilities of current 5G networks [1] in terms of throughput, latency and reliability. In combination with the congestion of the sub-6 GHz band, these ambitious performance requirements are the driving forces behind the ongoing trend towards the mmWave ((30–300) GHz) and Terahertz ((0.1–10) THz) frequency bands, where there is still an abundance of unexploited spectrum. Yet, this shift directly entails a more challenging propagation environment due to more pronounced shadowing, higher penetration losses, and increased path loss. Fortunately, by integrating multiple antennas in an array, the aforementioned obstacles can be mitigated by adopting adaptive beamforming techniques. Additionally, the accompanying increase in directivity enables more stable wireless channels by filtering out multipath components. Yet, a conventional co-located antenna array approach is still susceptible to non-line-of-sight (NLoS) blockage [2] when a static or dynamic blocker is in the direct path between base station and the user equipment (UE).

Recently, several innovative concepts have been proposed to maintain high-data-rate wireless connectivity in challenging NLoS situations. One approach consists in distributing active, intentional reflectors in the UE's environment to intelligently scatter the incident fields [3]–[5] around the obstacle. These reflectors can either be phased-array-based relays [3], which retransmit an amplified version of the signal, or intelligent reflective surfaces (IRS) [5], which alter the propagation direction of the incident wave. Another solution [2] leverages a distributed antenna system (DAS) where several remote antenna units (RAUs) are strategically deployed in the environment of the UE. Even with a limited number of RAUs, the probability of maintaining a line-of-sight (LoS) path between the UE and the DAS increases significantly [6], [7]. By massively increasing the number of radiating elements, the UE can be located in the near-field of the entire system, approaching the concept of a large intelligent surface (LIS) [8], enabling unprecedented energy focusing in a confined volume and minimizing inter-user interference. In [2], [9], a mmWave DAS is proposed that leverages mmWave-over-fiber to efficiently exchange broadband mmWave signals between the CO and distributed RAUs. In contrast to intermediate-frequency-over-fiber (IFoF) [10], which distributes the intermediate-frequency signal and a local oscillator (LO) signal, mmWave-over-fiber directly distributes the mmWave signals,

thereby simplifying the RAU's architecture by omitting mixers, at the cost of needing high-speed electro-optic components. Moreover, mmWave-over-fiber ensures tight synchronization between all mixer-free RAUs, paving the way for distributed beamforming and distributed MIMO (DMIMO) [6], [11]. An extensive measurement campaign has proven that such a mmWave-over-fiber DAS is able to achieve reliable communication with data rates up to 48 Gbps in a harsh realistic indoor environment with NLoS conditions [2]. However, [2], [9], [12] also showed that a mmWave-over-fiber DAS requires custom tailoring to the deployment environment, including judicious optimization of the required amplification level at various nodes in the opto-electronic transmit/receive (TRX) chain to obtain maximum wireless performance.

Despite many measurements [2], [9], [12] and models [13]–[18] can be found in literature, a system-level model for the evaluation and design of mmWave-over-fiber-based fiber-wireless (FiWi) down- and uplinks has so far been missing, making accurate and complete analysis very challenging and hindering the deployment on a large scale. Dedicated models in literature either focus on the radio equipment [13], or on the optical components [15]–[18]. In [15], a rigorous expression for an analog radio-over-fiber link is presented to study the amplitude and phase of the detected signal's fundamental frequency and its harmonics for different optical modulation formats. Furthermore, [16] analyzes the fundamental limits of intrinsic mmWave-over-fiber links and compares state-of-the-art opto-electric components with these limits to acquire insight into the limitations of the fiber link in a mmWave-over-fiber-based DAS. [18] combines an analytical model with simulations in VPI transmission maker for a mmWave-over-fiber link between CO and RAU to study the signal quality for different received powers at the RAU. [19] studies the signal quality of a WiMax signal in a mmWave-over-fiber wireless downlink and verifies the measurement results with simulations in VPI Photonics. Although it is very important to keep these limitations in mind when designing the mmWave-over-fiber wireless link, it is also of major importance to incorporate the mmWave wireless channel and the imperfections of additional active front-end components, essential to combat the high propagation losses. This is also confirmed in [20], pinpointing the mmWave radio as the main source of degradation, rather than the optical link, after in-depth characterization of the non-linear behavior of a single fiber-wireless end-to-end link.

In this chapter, we propose a versatile and time-efficient system-level simulation suite to accurately predict and optimize the down- and uplink signal quality of a mmWave-over-fiber-based DAS. It includes the non-linear behavior

of all the active electronic components and opto-electronic transducers, while also incorporating antenna system imperfections and the wireless channel between RAU and UE. Moreover, the simulation suite allows to study the influence of several active components on the link quality. The proposed model enables fast optimization of the mmWave-over-fiber wireless link between CO and UE while providing more insight into the system's bottlenecks and the signal quality at different stages in the link.

This chapter is organized as follows. Section 4.2.1 and 4.2.2 introduce the concept of a mmWave DAS and elaborate on a mmWave-over-fiber wireless link, respectively. Section 4.2.3 introduces the proposed simulation suite by outlining its architecture and defining its interfaces, and describes a representative fiber-wireless link to illustrate how our simulation suite can be used. Sections 4.3 and 4.4 both validate the simulation suite with an extensive measurement campaign. The former examines the case where a fixed-beam 1×4 antenna array with corporate feed is deployed at the RAU, while the latter focuses on a multi-beam four-element antenna array Butler matrix serving two UEs. Section 4.5 concludes the chapter.

4.2 Distributed Antenna System

4.2.1 System Overview

To alleviate the challenging propagation environment at mmWave frequencies, the use of a mmWave-over-fiber-based DAS is advocated in [2]. Whereas the DAS ensures reliable mmWave wireless communication, the mmWave-over-fiber architecture provides a low-loss and broadband connection between a CO and several RAUs. Additionally, synchronization between different RAUs is ensured owing to the up- and downconversion of the mmWave signals at the CO, while the optical-fiber-based routing ensures immunity to electromagnetic interference (EMI) issues.

Figure 4.1 provides a schematic overview of a general mmWave DAS architecture with its main components, being the CO, RAUs and UE. All signal processing is centralized at the CO, which also houses the mmWave-over-fiber transceivers, each consisting of an electro-optical (E/O) converter for the wireless downlink, and an opto-electrical (O/E) converter for the wireless uplink. The RAUs are distributed in the UEs' environment. Owing to the mmWave-over-fiber scheme, the RAUs exhibit low hardware complexity and low power consumption. Therefore, they are highly cost-effective

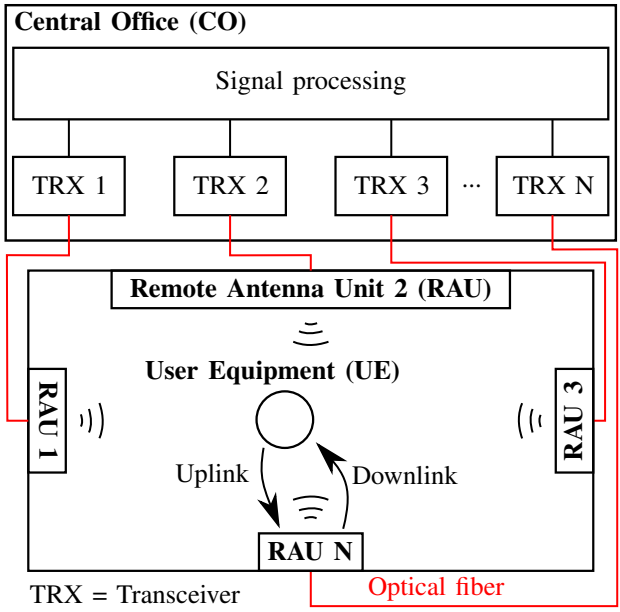

Figure 4.1: Schematic overview of a mmWave-over-fiber distributed antenna system (DAS). The central office (CO) implements all signal processing and mmWave-over-fiber transceivers. Strategic distribution of remote antenna units (RAUs) in the user equipment's (UE's) environment ensures line-of-sight communication, while their tight synchronization enables distributed MIMO (DMIMO) schemes.

when compared to RAUs tailored towards other optical signal distribution techniques, such as DRoF and IFoF [21]. In particular, the RAU only entails O/E and E/O conversion with corresponding electrical amplification, and incorporation of a suitable multi-antenna system with optional local beamforming. Recently, several high-performance antenna arrays have been proposed in literature that are suitable for integration within a RAU [22]–[24]. Additionally, since the broadband RF signals are optically distributed to the RAUs, the mmWave-over-fiber architecture facilitates the application of optical beamforming networks, offering significant advantages over classical electronic beamforming in terms of insertion loss, bandwidth and EMI-immunity [23], [25] at the expense of more O/E and E/O transducers. To guarantee high-throughput mmWave coverage for the UEs in presence of

mobile blockers, several strategies can be adopted, varying in degree of signal processing complexity. First of all, the system can either switch to the RAU with the best link, allowing maximum hardware re-use [9]. Furthermore, leveraging the inherent synchronization between the RAUs, the DAS can also apply DMIMO, or even holographic beamforming when the number of RAUs is large enough [8]. The latter enables unprecedented energy focusing in a confined volume while also lowering interference to other UEs. Finally, a hybrid approach is also possible.

It can be concluded that, in order to obtain maximum performance, the number of RAUs, their antenna configuration, the signal processing strategy, and the hardware at the CO require careful tailoring towards the targeted application, the wireless propagation environment, and the number of expected UEs. A simulation suite predicting system-level performance is therefore an indispensable tool in rolling out such a DAS.

4.2.2 mmWave-over-Fiber Wireless Link

High-performance mmWave-over-fiber wireless links are vital to the operation of the DAS. Figure 4.2(a) shows a representative downlink implementation of such a mmWave-over-fiber wireless link. For every downlink in the system, the mmWave signals are generated and converted to the optical domain at the CO. To this end, a polarization-dependent Mach-Zehnder modulator (MZM), an accompanying polarization controller, and a laser source are used. The MZM is quadrature-biased, where the electrical field of the light carrier is then modulated by the mmWave signals as [26], [27]:

$$E_{opt,out} = E_{opt,in} \cdot cos\left(\frac{\pi}{2} \cdot \frac{V_{mmWave}}{V_{\pi}} - \frac{\pi}{4}\right), \tag{4.1}$$

with $E_{opt,out}$ and $E_{opt,in}$ being the outgoing and incident optical fields of the MZM, respectively, V_{π} being the device-specific switching voltage, and V_{mmWave} being the differential voltage driving the MZM. The E/O conversion in the MZM generates a double sideband (DSB) signal around the light carrier [10]. This signal arrives at the RAU after propagation through a single-mode fiber. Due to inevitable fiber chromatic dispersion and the optical DSB modulation, the fiber is limited in length to avoid signal degradation [28]. Nevertheless, this limitation can be overcome to a large extent by adopting optical SSB (OSSB) modulation [12]. At the RAU, a photodiode performs O/E conversion, generating a photocurrent I_{PD} that only depends on the incident optical power

$P_{opt,PD}$ and the photodiode's responsivity R_{PD}:

$$I_{PD} = R_{PD} \cdot P_{opt,PD}. \tag{4.2}$$

The combination of the MZM biased at quadrature and the photodiode ensures a linear electric back-to-back conversion when the MZM's peak driving voltage is small enough in comparison to the switching voltage V_π of the MZM. As discussed in more detail in [16], notice that the electrical back-to-back conversion can have a positive or a negative gain, depending on the laser power and switching voltage V_π, amongst others [16]. In this chapter, the same convention is used where a negative gain corresponds to loss. After the optical link, amplifiers are used to increase the signal level and directly drive a beamforming network (BFN), which applies the correct phases and amplitudes to the antenna array elements. Finally, after propagation over the wireless channel, the UE amplifies the received signal again before further processing.

The architecture and system-level model of a potential mmWave-over-fiber wireless uplink implementation are shown in Figure 4.2(d) and (e), respectively. Now, the uplink signal is generated at the UE and processed in the CO. Furthermore, the MZM and the photodiode are placed at the RAU and the CO, respectively. Moreover, the MZM is now driven by a single-ended amplifier. Additionally, the laser remains at the CO to further ensure centralization of all expensive hardware [29], and two fibers are used. One fiber transports the optical carrier from CO to RAU, while another fiber returns the modulated light to the CO. While Figure 4.2(a) and (d) present the general concept of a mmWave-over-fiber wireless link, depending on the practical implementation, a single fiber might suffice for both up- and downlink in a time division duplex scheme [12].

4.2.3 Simulation Suite

Figure 4.3 shows a schematic overview of the system-level simulation suite to analyze mmWave-over-fiber-based DASs, leveraging component-level models implemented in MATLAB, Keysight SystemVue, CST Microwave Studio, and the Keysight PathWave 89600 VSA software. A main MATLAB script orchestrates the simulation suite by controlling the different software packages and interfacing them, handling the different in- and outputs of the different blocks in the simulation suite. At the heart of the simulation suite, Keysight SystemVue is used to generate the waveforms at CO and UEs, and to

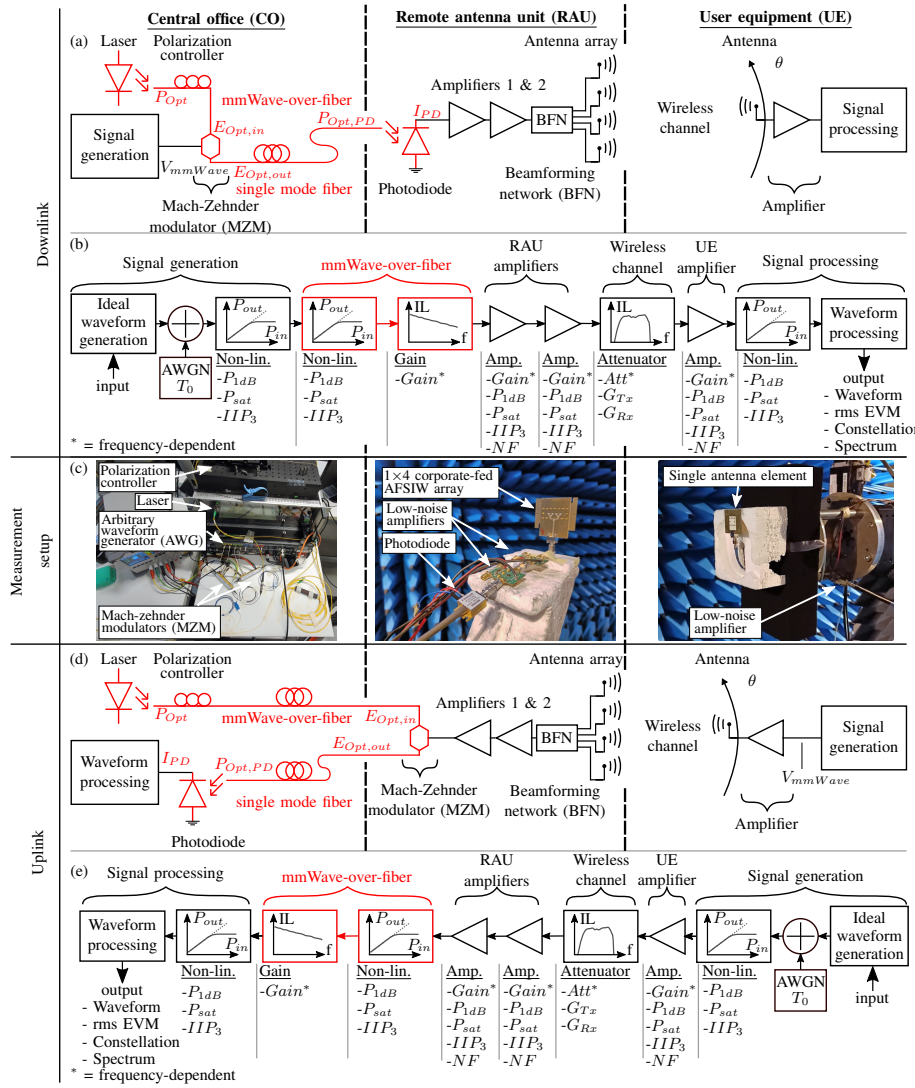

Figure 4.2: mmWave-over-fiber wireless down- and uplink consisting of the central office (CO, left), the remote antenna unit (RAU, middle), and the user equipment (UE, right). For downlink communication, a Mach-Zehnder modulator (MZM) performs electro-optical (E/O) conversion at the CO, directly modulating the optical carrier with the mmWave signal. After propagation through a single-mode fiber, the signal is converted back to the electrical domain by a photodiode and is amplified to directly drive a beamforming network (BFN) with integrated antenna array. The antenna system at the UE receives the signal and amplifies it before processing. Architecture of downlink (a) and uplink (d), system-level model overview of downlink (b) and uplink (e), and measurement setup (c).

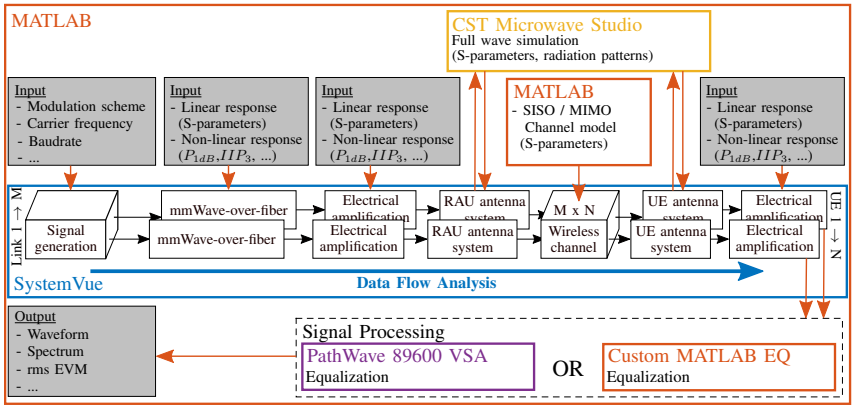

Figure 4.3: Schematic overview of the system-level simulation suite: MATLAB dynamically links all software packages and controls the inputs of SystemVue, which simulates the implemented mmWave-over-Fiber distributed antenna system. The antenna systems at the remote antenna unit and user equipment are simulated using CST Microwave Studio. A channel model is implemented in MATLAB. Alternatively, measured radiation patterns/channels, and other channel models (e.g. obtained via a raytracing tool) can also be imported. SystemVue's Data Flow Analysis calculates the received signals, which can be equalized by either a custom equalizer in MATLAB, or PathWave VSA 89500 software.

flexibly model a mmWave-over-fiber-based wireless system architecture. The software's Data Flow Analysis performs a time-domain simulation of the generated waveforms through the model. In the case of a mmWave-over-fiber DAS, this architecture consists of M mmWave-over-fiber links connecting to the M RAUs, N UEs, and a wireless channel describing the propagation environment between the M RAUs and the N UEs. For the signal generation, MATLAB provides several inputs to SystemVue, including the modulation scheme, carrier frequency, baudrate, and the matched filter roll-off factor. Furthermore, it is also possible to incorporate custom (precoded) data to simulate a MIMO system. The other building blocks are characterized by either a linear response (consisting of scattering parameters), a non-linear response (consisting of e.g. P_{sat}, P_{1dB}, IIP_3) or a noise figure, or, in most cases, a combination of these three. A more detailed description of each of the building blocks and their configuration is given below when describing a representative fiber-wireless architecture (Figure 4.2) as an application example. These parameters can be found in the datasheet of the component, or

obtained via measurements/simulations. In particular, to accurately describe the antenna system at the RAUs and UEs, MATLAB initiates CST Microwave Studio's full wave solver (if these results are not already present) to obtain their realized gain patterns and S-parameters. Alternatively, when desired, the antenna systems at the RAUs and UE can be modeled by means of measurement data.

The latter are then combined in MATLAB with an appropriate channel model, and provided to SystemVue as a scattering parameter matrix. Alternatively, a measured channel, including antenna effects, could be used. Subsequently, the Data Flow Analysis calculates the signals at the output of each of the UEs, after which they are equalized by either PathWave's VSA 89600 software or a custom equalizer implemented in MATLAB. Finally, based on these equalized waveforms, all relevant output parameters can be derived, such as the received spectrum, the root-mean-square (rms) error vector magnitude (EVM), ... By adopting such a modular approach, the simulation suite can be used for a wide variety of use cases, such as the optimization of individual components, while studying their impact on the fiber-wireless link, investigating the performance gain by adopting a co-design approach instead of a more conventional diakoptic approach, analyzing the impact of different local beam steering techniques [23], [24], [30], and testing/verifying different signal algorithms. When combining the proposed simulation suite with appropriate ray-tracing software in the future, it could even be used to optimize the placement of RAUs in a real-life scenario.

Figure 4.2(a) shows a representative example of a fiber-wireless downlink, consisting of a RAU serving a single mobile user by means of a beamforming antenna array. The corresponding system-level model in our simulation suite is shown in Figure 4.2(b) and consists of a chain of several components, subdivided into different submodels, being the signal generation stage, the mmWave-over-fiber link, the RAU amplifier chain, the wireless channel, the UE amplifier chain, and the signal processing stage. Apart from the signal generation and processing stages, all components either introduce non-linear distortion, add white gaussian noise, or introduce frequency-dependent gain/attenuation. Non-linear distortion is specified by the input 1-dB compression point (IIP_{1dB}), the input saturation power (IP_{sat}), and the input third-order intercept point (IIP_3). The amplifiers combine several of these behaviors, introducing non-linear distortion referred to the output power ($OP_{1dB}/OP_{sat}/OIP_3$), applying frequency-dependent gain, and also adding white gaussian noise, specified by its noise figure (NF). In the signal generation submodel, the ideal mmWave signal is combined with additive

white gaussian noise (AWGN), which is characterized by a noise temperature T_0 and serves as an equivalent noise source, aggregating several other noise sources present in the fiber-wireless link. These include not only electronic noise contributions introduced by non-ideal signal generation (quantization noise, and clock jitter), but also the optical noise sources, such as the shot noise of the photodiode. When using a single mode laser with a low relaxation frequency and directly driving a MZM, the optical link noise is dominated by the shot noise of the photodiode [31], and the relative intensity noise (RIN) of the laser can be neglected, as in [31]. Yet, if needed, the RIN noise could be incorporated in our simulation suite by adequately modifying the equivalent AWGN noise source (Figure 4.2(b) and (e)). Finally, non-linear distortion is applied to the noisy mmWave signal, modeling imperfections related to the signal generation with practical digital-to-analog converters (DACs) [32].

The next submodel represents the mmWave-over-fiber link, which consists of the biased MZM, the optical fiber and the photodiode. The linear behavior of such a unilateral electrical two-port can be described by an $S_{21,opt}$ scattering parameter, taking into account several frequency-dependent effects such as optical loss and device parasitics. Furthermore, the link's $S_{21,opt}$ parameter description can either be acquired through simulations or measurements. It depends on several parameters, including the employed optical power, influencing the MZM's slope efficiency [16], the MZM's bias voltage [26] and the photodetector's responsivity. Finally, the mmWave-over-fiber submodel also includes the non-linear distortion introduced by the MZM's electro-optical conversion, as described by Eq. 4.1.

Next, the model in Figure 4.2(b) includes a cascade of components representing the RAU's transmit amplifier chain, the wireless channel, and the UE's receive amplifier chain. Similar to the mmWave-over-fiber link, the wireless channel, which also includes the antenna array and BFN at the RAU and the receive antenna at the UE, is modeled by an S_{21} scattering parameter. Again, the exact description can either be generated through numerical/analytical models or measurements, and depends on several parameters, being the propagation environment, the RAU's BFN implementation and configuration, and the positions, orientations and realized gain patterns G_{RAU} and G_{UE} of the antennas at the RAU and UE.

At the final signal processing stage, a non-linear distortion component accounts for the imperfections arising from measurement equipment based on practical analog-to-digital converters (ADCs). The waveform processing demodulates and potentially equalizes the received signal, and calculates the rms EVM as a

figure of merit, which is a metric for the difference between the received and the ideal constellation points. Based on criteria by 3GPP, EVM values below 17.5 %, 12.5 %, and 8 %, allow transmission of QPSK, 16-QAM, or 64-QAM symbols, respectively, giving an indication of achievable data rates [33].

Similarly, a representative model for the uplink is shown in Figure 4.2(e), consisting of similar submodels, yet in a different order, showing the flexibility of the proposed simulation suite.

4.3 Antenna Array with Corporate Feed

As a validation of the proposed model, we consider the case of a DAS with a single RAU based on the antenna array with corporate feed proposed in [22]. First of all, the influence of several system parameters on the signal quality, quantified in terms of the rms EVM, will be investigated and compared to measurements. The studied parameters are the RF power, optical power and the symbol rate. In addition, the downlink EVM is predicted as a function of UE position in the room. For a given cross-section in this room, the result of the model is compared to measurements for both the downlink and the uplink. Moreover, a two-ray ground-reflection propagation channel model is implemented in MATLAB to show the versatility of the simulation suite. In this case, the measured received spectrum and constellation at the UE is compared to the simulation suite's predictions.

4.3.1 Measurement Setup and System-Level Model Parameters

In Figure 4.2(c), an annotated picture is shown of the CO, RAU, and UE of the deployed DAS. In the setup, a fixed-beam 1×4 air-filled substrate-integrated-waveguide (AFSIW) antenna array with corporate feed [22] is used at the RAU, while a single AFSIW antenna element is used at the UE. The individual antennas exhibit a peak gain of 7.4 dBi and an efficiency of at least 85% in the [24.25-29.5] GHz band. The 1×4 array features a peak gain of 10.1 dBi. Unless mentioned otherwise, an arbitrary waveform generator (AWG) (92 GSps Keysight M8196a) is used as signal generator to directly generate a modulated 2 GBd QPSK signal with a root-raised cosine transmit filter with a roll-off factor of 0.35 at a carrier frequency of 28 GHz with a peak signal amplitude of $V_{mmWave,p}$. This signal is taken to showcase the ability of mmWave-over-fiber to distribute a broadband signal that fits in the

n257 5G band. Furthermore, the laser (1550 nm BASIC NKT Photonics) output power equals P_{opt}. The MZM (Fujitsu FTM7937EZ $LiNbO_3$,V_π = 3.5 V) is biased at its quadrature with a benchtop power supply to ensure linear electro-optic conversion. In the current setup, the DC bias is manually adjusted to minimize drift due to RF heating. Yet, in a practical setup, this can automatically be realized by a feedback loop [34]. The MZM is driven in a push (uplink) or push-pull (downlink) configuration to implement optical double sideband modulation. A single-mode optical fiber (with standard dispersion of 17 ps/(nm km)) is used to interconnect RAU to CO. Its length of 20 m is well below the first chromatic-dispersion-induced extinction dip at around 4 km for a single-carrier (30 GHz) DSB-modulated signal around a 1550 nm light carrier [28]. A commercial photodiode (Finisar XPDV2120R-VF-FA) with a reverse bias voltage of 2 V is employed. All the amplifiers in the setup are low-noise amplifiers (Analog Devices HMC1040). Moreover, the RAU and the UE of the setup are installed in an anechoic chamber mimicking free-space conditions, with a separation distance of 2.2 m. The signal, received by the UE's antenna, is amplified and directly sampled by a real-time oscilloscope (RTO) (80 Gsps Keysight DSAZ634a), which also runs the Keysight PathWave VSA 89600 software for fair comparison.

As a starting point, the input parameters of the system-level model, annotated in Figure 4.2(b) and Figure 4.2(e), are determined by either consulting the component's datasheet, performing measurements or full-wave simulations. The frequency-dependent amplifier gain is measured by using a Keysight N5247B PNA-X vector network analyzer (VNA), while its non-linear distortion parameters are taken from the datasheet. For the mmWave-over-fiber link, the electrical back-to-back scattering parameters and its non-linear distortion are measured with the VNA for an optical power at the input of the MZM of 13.5 dBm. Simulating this gain at different optical powers is implemented by correcting the measured $|S_{21}|$ as [16]:

$$\left|S_{21,corr}\right| = |S_{21}| + 2 \cdot \left(P_{opt} - 13.5\,\text{dBm}\right), \tag{4.3}$$

with $\left|S_{21,corr}\right|$ being the corrected electrical gain at optical power P_{opt}. Using an external modulator limits the frequency chirp with respect to a directly modulated laser. Owing to the DC extinction ratio $\geq$ 20 dB of the adopted Fujitsu laser, the effect of the remaining frequency chirp can be modeled as an additional loss to the dispersion penalty [35]. For our setup, this additional loss is included in the "Gain" building block of the mmWave-over-fiber submodel (Figure 4.2(b) and (e)). Since the optical link varies between up- and downlink in the measurements, this corrected insertion loss can differ by an offset factor.

Next, the wireless channel is constructed by simulating the realized gain of the RAU front-end (feeding network with corporate feed and antenna array), and the single element in CST Microwave Studio's frequency domain solver. Using these realized gain patterns, a wireless channel model is implemented in MATLAB using the Friis power transmission equations, since all measurements are performed in a (semi-)anechoic environment.

Table 4.1: System-level model parameters for a mmWave-over-fiber wireless link in case an antenna array with corporate feed is employed at the RAU.

Amplification: HMC1040	
$Gain^*$ at 28 GHz	23.8 dB
OP_{1dB}	8.5 dBm
OP_{sat}	10.5 dBm
OIP_3	18.5 dBm
NF	2.2 dB
Optical Link	
Att^* at 28 GHz	25.9 dB
IP_{1dB}	5 dBm
IP_{sat}	8 dBm
IIP_3	18.4 dBm
Wireless channel	
Att^* at 28 GHz	55.7 dB
Non-linearity: AWG	
IP_{1dB}	-11 dBm
IP_{sat}	-8 dBm
IIP_3	-3 dBm
Non-linearity: RTO	
IP_{1dB}	-11 dBm
IP_{sat}	-8 dBm
IIP_3	-3.5 dBm
Overall parameters	
T_0	300 K
*: Frequency-dependent	

Owing to the modular nature of the simulation suite, more advanced wireless channel models/measurements can be incorporated in the future to optimize RAU placement in real-life environments. Additionally, a two-tone measurement is performed to determine the distortion introduced by the

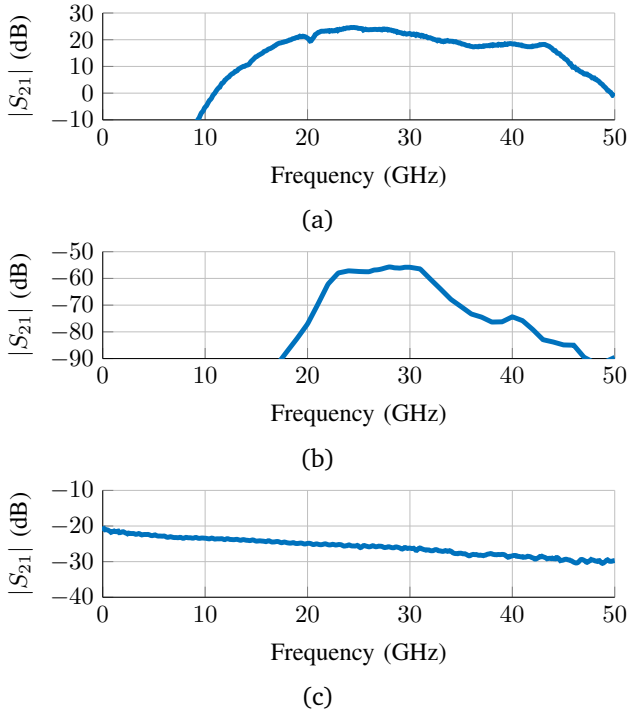

Figure 4.4: The frequency-dependent model parameters as a function of the frequency: (a) the amplifier (HMC1040) gain, (b) the wireless channel loss and (c) the optical link loss.

AWG and RTO. As initial value for the noise temperature, 290 K is taken. The parameters are then simultaneously optimized for the up- and downlink to account for additional losses in the link, originating from the use of evaluation boards instead of integrated ICs, interconnects, and cables. They are given in Table 4.1. As the table only lists the frequency-dependent parameters at the center frequency of 28 GHz, Figure 4.4 shows the amplifier gain, optical link loss, and the wireless channel attenuation as a function of frequency.

4.3.2 First Validation of the Model

Figs. 4.5, 4.6 and 4.7 show the rms EVM as a function of the mmWave-over-fiber link's optical power, peak signal amplitude, and baud

rate, respectively, comparing simulation and measurement as a validation of the model. These results also illustrate the behavior of the link and explain the choice of these parameters in the remainder of the experiments. More specifically, Figure 4.5 shows the rms EVM as a function of optical laser power for two different AWG output amplitudes ($V_{mmWave,p}$), equal to 100 mV and 200 mV. For both values of $V_{mmWave,p}$, the simulations (lines) and measurements (dots) indicate an initial decrease in EVM for increasing optical power and show excellent agreement with a maximum error in EVM of only 0.8 % and 2.4 % for the 100 mV and 200 mV traces, respectively. This increase in signal quality is expected since the increased light power does not influence the modulation depth and, therefore, does not increase the MZM-induced non-linear distortion (Eq. 4.1), but only the total modulated power. In our measurement setup, the optical power is limited by the employed CO laser's maximum output power of 15 dBm, but in principle, the laser power can be further increased, improving the slope efficiency of the optical modulator [16], and hence decreasing the overall losses in the intrinsic analog radio-over-fiber link. Yet, when predicting the EVM for optical powers beyond 15 dBm, the simulation suite shows that the RAU's amplifiers are driven in compression, giving rise to non-linear effects and deteriorating signal quality beyond the optimal value. Moreover, comparing the minimum EVM values of both curves reveals that the optimal value for the 100 mV curve is slightly (0.5 %) higher than for the 200 mV curve. This is because a higher optical power gives rise to increased shot noise. Yet, care should be taken that the optical fiber's field intensity remains sufficiently low such that non-linear effects including Raman scattering remain negligible [36], and the laser's RIN remains sufficiently low [16].

In addition, Figure 4.6 depicts the influence of the RF signal power on the UE's signal quality for an optical power of 12 dBm and 15 dBm. The simulation results (lines) agree well with the measurements (dots) with an overall maximum deviation of 1.3 % between both. At lower RF power (such as for a peak signal amplitude 100 mV), the received signal is mainly noise-limited, whereas at higher RF power (beyond peak signal amplitude ≈500 mV), non-linear distortion limits the performance of the system. As also shown in Figure 4.6, there is an optimal value for the RF signal power with an optimal trade-off between noise and non-linear distortion, which leads to minimum EVM and maximum link performance. The main contributors to the non-linear distortion at higher RF powers in this setup are the second amplifier in the RAU's optical receive chain, and the signal generation in the AWG since its spur-free dynamic range (SFDR) decreases significantly near

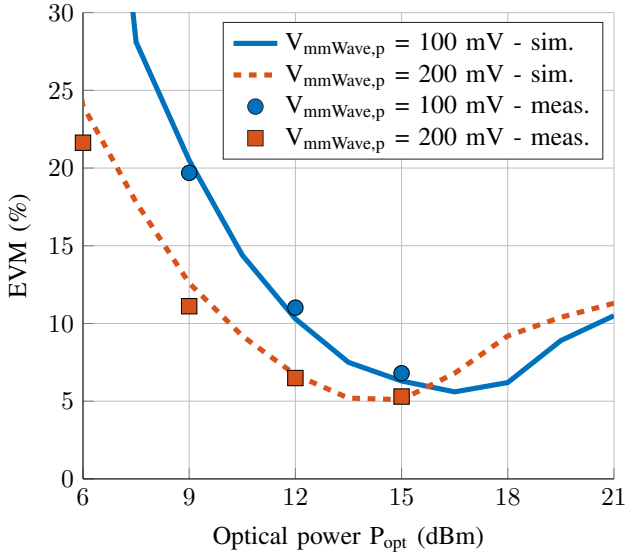

Figure 4.5: Measured and simulated root-mean-square (rms) error vector magnitude (EVM) as a function of the laser output power.

its Nyquist rate and overall bandwidth. Although the previous experiment showed that a higher optical power generally results in a better signal quality, this analysis shows that a decrease in optical power can be compensated for to a certain degree by an increase in RF power. Since the photocurrent I_{PD} scales linearly with the optical power P_{opt} (Eq. 4.2), the photodiode's electrical output power scales quadratically with the optical power. The reduced optical power can be compensated by a quadratic increase in RF power, at the penalty of introducing more non-linearities in the MZM. Indeed, it can be observed in Figure 4.6 that, as the laser power decreases by 3 dB, the optimum signal amplitude approximately doubles (400 mV vs 200 mV).

Finally, Figure 4.7 shows the simulated and measured EVM for different symbol rates at a carrier frequency of 28 GHz for a peak signal amplitude of 200 mV and a laser power of 15 dBm. Again, a good agreement between simulation and measurement can be observed, indicating a similar trend. A maximum deviation of only 2.4 % is observed for baud rates above 4 Gbd. This deviation can be mainly attributed to the non-ideal behavior of the AWG as a mmWave source and the RTO, both operating close to their operational limits in terms

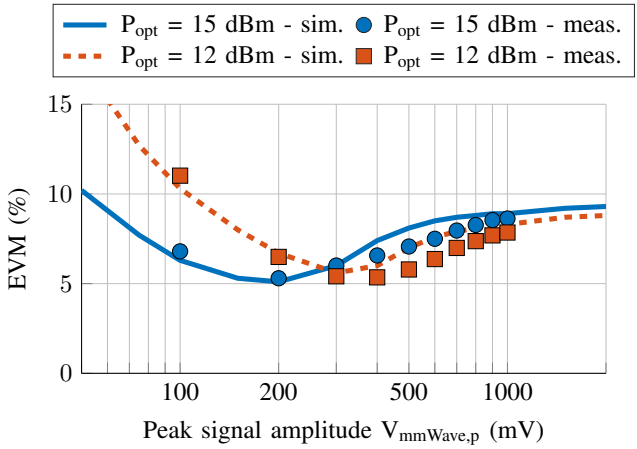

Figure 4.6: Simulated and measured root-mean-square (RMS) error vector magnitude (EVM) as a function of the peak of the mmWave signal ($V_{mmWave,p}$) driving the Mach Zehnder modulator (MZM).

of DAC/ADC sampling rate and analog bandwidth.

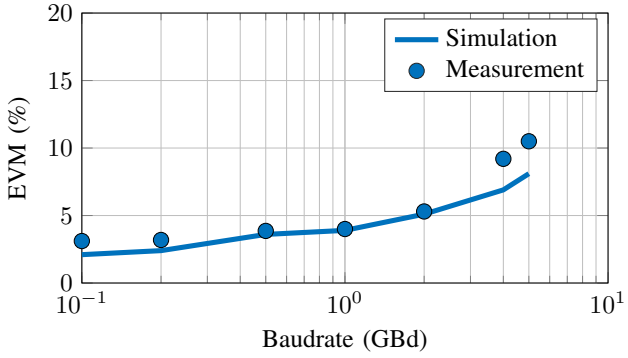

Figure 4.7: Simulated and measured link quality as a function of symbol rate.

These experiments (Figs. 4.5 to 4.7) validate the proposed system-level model of the mmWave-over-fiber wireless link, accurately predicting the measured signal quality when tuning a variety of parameters such as the RF power, optical laser power and the baudrate without reoptimization of the model.

Additionally, the model also correctly predicts the most optimal operating

point, being a laser power of 15 dBm and a signal amplitude of 200 mV, which will be used in the remainder of the experiments.

4.3.3 Uplink vs. Downlink

In this subsection, the downlink and uplink signal quality is studied for a UE located at different locations in an anechoic environment. This allows validating the model for significantly different magnitudes of wireless channel losses, and allows predicting the coverage area of a RAU.

In this setup, the RAU and UE are deployed inside an anechoic chamber with a wireless propagation distance of 2.2 m. The RAU is mounted on a rotational stage of an NSI-MI spherical near-field antenna measurement system. By rotating the RAU, the position of the UE with respect to the RAU is varied while keeping the propagation distance constant.

Figure 4.8(a) shows the simulated downlink signal quality for a UE positioned at different locations with coordinates (X,Y) in an anechoic room with dimensions 5 m by 10 m. As expected for a free-space environment, the best signal quality is obtained when the UE is located in the main lobe direction, gradually decreasing as the wireless propagation distance (the path loss) increases. The red area indicates the locations where, according to 3GPP, a data rate of 12 Gbps (2 GBd with 64-QAM symbols) in the n257 5G band can be achieved.

Figure 4.8(b) depicts the measured and simulated rms EVM as a function of the UE angle θ (defined as the angle between the UE and RAU), for a fixed wireless propagation distance of 2.2 m between RAU and UE, as annotated by the white dotted line on Figure 4.8(a). A good agreement between simulation and measurement is observed and good signal qualities are achieved in the array's main lobe for the downlink. Although a slightly worse measured rms EVM of 5.7 % is achieved in the uplink (versus 5.4 % in the downlink), simulation and measurement again agree well. Nevertheless, in both cases, a discrepancy in signal quality is observed in the sidelobes around θ ±45°. This can be attributed to the difference in sidelobe level (SLL) between the simulated and the actual antenna array gain in the mmWave-over-fiber setup. While the RAU's antenna array is simulated in free-space stand-alone conditions, the vicinity of the amplifiers and cables at the array's backside in the mmWave-over-fiber wireless link measurement setup (Figure 4.2(c)) gives rise to an increased SLL. Indeed, when an increase in SLL by only 2.5 dB is taken into account in the model, there is a good agreement between

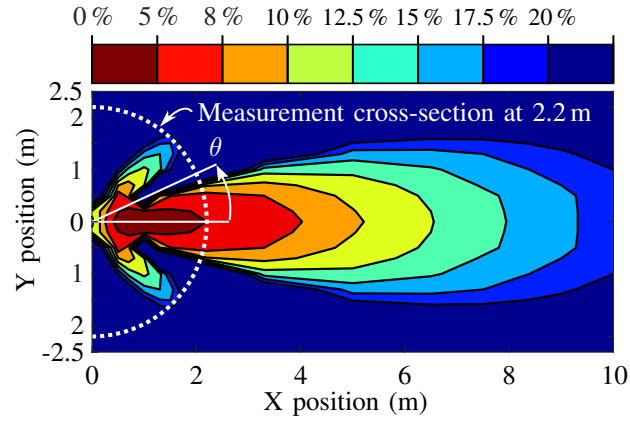

(a)

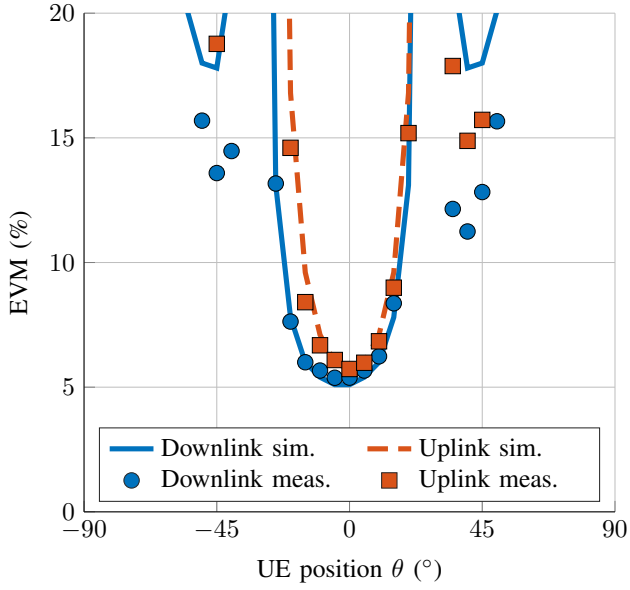

(b)

Figure 4.8: (a) Simulation of the downlink root-mean-square (rms) error vector magnitude (EVM) for a user equipment (UE) positioned at different locations in an anechoic room (dimensions: 5 m by 10 m). (b) Comparison between simulated and measured up- and downlink quality for the indicated cross-section (white half-circle in Figure 4.8(a)) at a distance 2.2 m.

simulated and measured EVM values for all UE positions. To minimize the impact of the integration platform/measurement setup on system-level performance, a higher level of integration should be pursued by integrating all RAU components at the antenna backside and by adopting an antenna array topology with higher front-to-back ratio, as in [23].

After simulating the RAU and UE antenna system in CST Microwave Studio, the simulation suite requires less than 7 minutes to generate the downlink curve in Figure 4.8(b) with a resolution of 5 degrees, assuming a 5 µs-long 2-GBd QPSK signal (Dell Latitude 5590, CPU: i7-8650U, RAM: 16 GB).

4.3.4 Two-Ray Propagation Channel

Next, we focus on the semi-anechoic environment shown in Figure 4.9(a). This is realized by deploying a copper sheet in between the RAU and CO to introduce a well-defined ground reflection. The setup can be accurately described by a two-ray channel model. The RAU and UE antenna system are separated by a distance of 2.28 m, both at a height of 0.43 m above the copper plate. As in Section 4.3.2, the mmWave-over-fiber downlink is operated in its optimal working point with a peak voltage amplitude $V_{mmWave,p}$ of 200 mV and a laser power of 15 dBm.

Figure 4.9(b) compares the measured and simulated spectra at the UE when a 500-ns-long 2-GBd QPSK signal is transmitted. An excellent agreement is observed, with the model not only predicting the frequency at which the direct and ground-reflected waves interfere destructively, but also accurately capturing the signal strength of both paths. The figure also compares the simulated and measured constellation plots (4000 symbols). As a result of the multipath propagation, the QPSK symbols deviate from their ideal constellation points (black dots in inset of Figure 4.9(b)) and each point splits up into four distinct point clouds. This behavior is again successfully predicted by the model, providing a first validation of the simulation suite for multipath environments.

4.4 Multi-Beam Antenna Array

The proposed model is further validated by considering an alternative measurement scenario involving a multi-beam RAU implementing local beamforming. The setup is identical to the setup as shown in Figure 4.1,

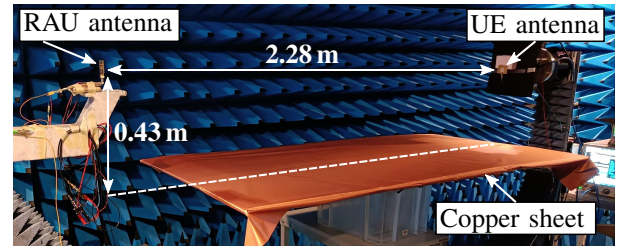

(a)

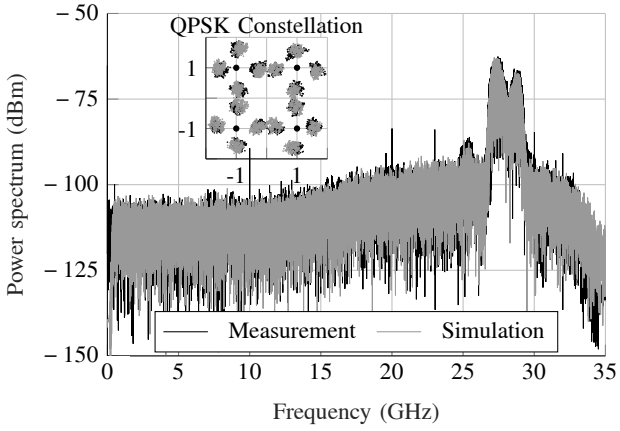

(b)

Figure 4.9: (a) Measurement setup: a large copper sheet deployed inside the anechoic chamber creates a propagation environment that is well described by the two-ray channel model (b) comparison between simulated and measured spectrum of a 2 GBd QPSK signal for a two-ray ground-reflection propagation channel. The inset depicts the simulated and measured constellation plot.

except that the RAU is now based on a 1×4 AFSIW antenna array which is compactly integrated with a low-loss and broadband 4×4 Butler matrix implemented in grounded-coplanar waveguide technology [24]. Through four different connectorized ports, the integrated beamforming array is able to generate four beams in four different discrete directions. The operational frequency band ranges from 23.75 GHz to 31 GHz and the maximal measured gain equals 12.3 dB.

First, we validate the model by focusing on the case where a single beam is switched to several discrete directions, in the meantime also demonstrating the

potential of local beamforming to extend system coverage in a cost-effective way. Next, a multi-beam scenario is considered, where the RAU simultaneously serves two UEs in two distinct directions to analyze the influence of residual inter-user interference.

4.4.1 Single Beam

Figure 4.10 shows the downlink EVM for each of the four input ports of the multi-beam RAU as a function of the angle between RAU an UE when the UE is positioned at different locations at a fixed distance of 2.2 m with respect to the RAU. When comparing the simulations (solid lines) with the measurements (dots), a good agreement is noticed, especially along the main beams. A small discrepancy can be observed between simulated and measured beamwidth. Again, the simulated signal quality in the sidelobes is slightly lower than observed during the measurements. This is again due to the difference between the full-wave simulation of the co-designed BFN with antennas, and the realized antenna array. Comparing the results of the fixed-beam-based RAU and the multi-beam RAU, an identical signal quality is observed when the UE is illuminated by the RAU's main beam, proving both BFNs have comparable insertion losses. Moreover, when comparing the angular sectors covered at an EVM below 8 % by the two RAU implementations, it is immediately clear that the multi-beam RAU covers a four times larger angular sector, at the cost of requiring an additional RF switch.

4.4.2 Impact of Multiple Active Beams

Finally, the model is employed to predict the change in signal quality when simultaneously transmitting two beams rather than one, illustrating the capability of the model to incorporate inter-user interference.

This setup now involves two different mmWave-over-fiber links, each driving one of the input ports of the Butler matrix with a different 2-GBd signal (generated with a different length pseudo-random binary sequence (PRBS) generator polynomial to distinguish between both beams at the receiver by leveraging a custom zero-forcing equalizer in MATLAB). The maximum laser power is now split over the two optical links and the amplitude of the generated signals is 400 mV and 500 mV for Butler matrix ports 3 and 4, respectively. While in this setup, the two mmWave-over-fiber links are used to exchange two distinct signals to a multi-beam RAU, they could also be used to serve two RAUs. In the latter case, wavelength division multiplexing

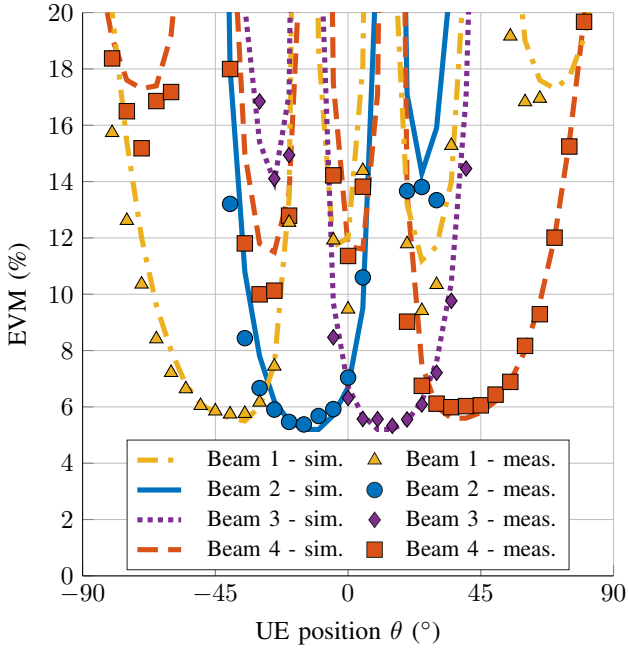

Figure 4.10: Simulated (solid) and measured (dots) root-mean-square (rms) error vector magnitude (EVM) of a mmWave-over-fiber wireless downlink as a function of UE position in case a switched-beam RAU is used.

could be used to support multiple beams per RAU [37]. The model includes this second mmWave-over-fiber link and takes into account the different MZM driving voltages employed during the measurements, resulting from slight variations in the mmWave-over-fiber links' equipment. Additionally, the full-wave simulation of antenna array with integrated BFN incorporates the BFN's imperfections, such as electromagnetic coupling and insertion losses.

First, the simulated and measured signal qualities are compared when only one of both links is active. This comparison is shown in Figure 4.11(a). These results are comparable to the switched-beam RAU case in Figure 4.10. Yet, a slight increase in EVM (0.8 % for beam 1 and 1.8 % for beam 3 in measurements) is observed as the available laser power per input port is reduced by 3 dB. At broadside, a good agreement is obtained between measurements and the simulation suite prediction, with a maximum deviation of only 0.3 %.

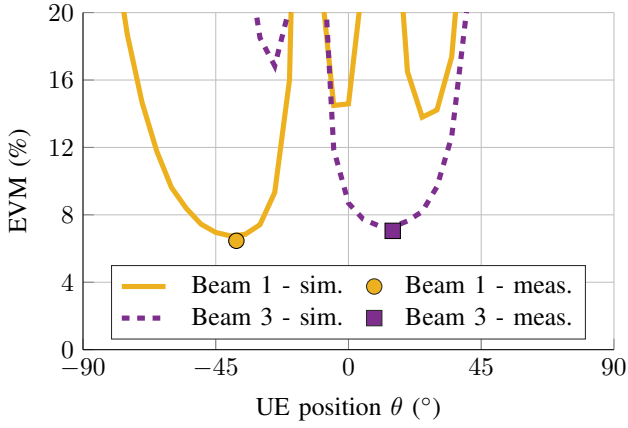

(a)

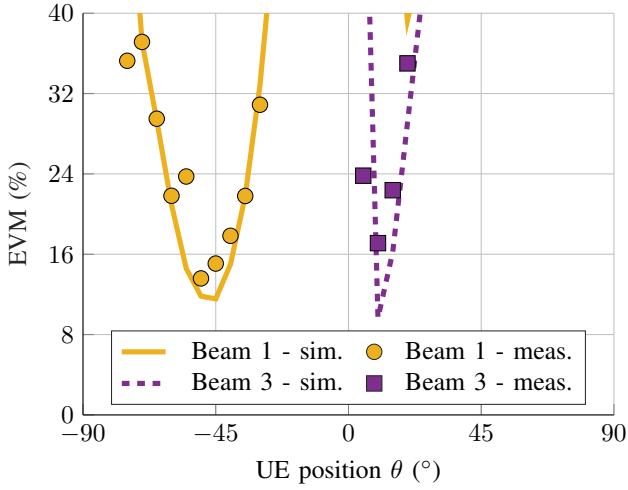

(b)

Figure 4.11: Simulated (solid) and measured (dashed) root-mean-square (rms) error vector magnitude (EVM) as a function of UE position for downlink communication with a multi-beam RAU when (a) beam 1 and beam 3 are individually activated and when (b) beam 1 and beam 3 are simultaneously activated.

Figure 4.11(b) shows the measured and simulated rms EVM values when two

beams (beam 1 and 3) are transmitted simultaneously. Again, the measured EVM is predicted well by our simulation suite. Minor deviations can be attributed to the difference in simulated and actual SLL of the multi-beam RAU, and to minor phase errors in the manufactured Butler matrix, introducing a shift in the beam pattern nulls. Comparing to Figure 4.11(a) reveals that the signal quality deteriorates due to inter-beam interference. In particular, the best EVM is worse when two beams are active and the angular range over which the EVM remains below 17.5 % (3GPP criterium for QPSK transmission) is smaller. The latter effect is more pronounced for beam 3 as the side lobes of beam 1 are higher within the half-power beamwidth of beam 3 (as seen in Figure 4.11(a)).

The time required by the simulation suite to calculate the EVM for all UE positions in Figure 4.11(b) (with a resolution of 5°) remains below 12 minutes for two simultaneous mmWave-over-fiber wireless links, assuming a transmitted 5 µs-long 2-GBd QPSK signal (compared to 7 minutes for a single mmWave-over-fiber link in Section 4.3; Dell Latitude 5590, CPU: i7-8650U, RAM: 16 GB).

4.5 Conclusion

We have proposed a dedicated simulation suite to predict the system-level performance of mmWave-over-fiber-based distributed antenna systems (DASs). Specifically, the simulation suite incorporates accurate models for the mmWave-over-fiber link and the electronic amplifiers, including non-linear distortion and noise, full-wave models for the antenna front-ends, capturing the most important electromagnetic effects, and analytical wireless channel models, accounting for the high propagation losses encountered at mmWave frequencies

A thorough validation was performed by means of an extensive measurement campaign on a representative fiber-wireless link, supporting both up- and downlink communication. First of all, we have focused on a single mobile user served by a fixed-beam remote antenna unit (RAU), interconnected to the central office (CO) by means of a single mmWave-over-fiber link, in free-space conditions. The up/downlink's rms error-vector-magnitude (EVM) was accurately predicted over a wide range of user positions and system parameters. Additionally, the impact of a two-ray ground-reflection channel on signal quality was analyzed to prove the simulation suite's versatility. Next, a more complex scenario was considered where a multi-beam RAU simultaneously

serves two mobile users by means of two independent mmWave-over-fiber links. Again, good agreement between simulation and measurement was obtained, proving that inter-user interference is accurately captured.

In the future, the simulation suite can be further extended with more advanced channel models, by, for instance, also including ray-tracing-based simulators, and it may be further validated by larger multi-RAU measurement campaigns. Additionally, the proposed model can be used to test various calibration and channel estimation algorithms, as well as taking a step towards dynamic link budgeting, thereby becoming a very powerful tool in planning the deployment of a DAS and optimizing the configuration of its RAUs, the CO architecture, and the signal processing towards the target application, the wireless propagation environment, and the number of expected users.

References

[1] M. Giordani, M. Polese, M. Mezzavilla, S. Rangan, and M. Zorzi, "Toward 6G networks: Use cases and technologies", *IEEE communications magazine*, vol. 58, no. 3, pp. 55–61, 2020.

[2] A. Moerman, J. Van Kerrebrouck, O. Caytan, *et al.*, "Beyond 5G Without Obstacles: mmWave-over-Fiber Distributed Antenna Systems", *IEEE Communications Magazine*, vol. 60, no. 1, pp. 27–33, 2022.

[3] E. Björnson, Ö. Özdogan, and E. G. Larsson, "Reconfigurable intelligent surfaces: Three myths and two critical questions", *IEEE Commun. Mag.*, vol. 58, no. 12, pp. 90–96, Dec. 2020.

[4] J. Rao, Y. Zhang, S. Tang, *et al.*, "A Novel Reconfigurable Intelligent Surface for Wide-Angle Passive Beamforming", *IEEE Trans. Microw. Theory Techn.*, vol. 70, no. 12, pp. 5427–5439, Dec. 2022.

[5] M. Di Renzo, A. Zappone, M. Debbah, *et al.*, "Smart Radio Environments Empowered by Reconfigurable Intelligent Surfaces: How It Works, State of Research, and The Road Ahead", *IEEE J. Sel. Areas Commun.*, vol. 38, no. 11, pp. 2450–2525, Nov. 2020.

[6] I. C. Sezgin, M. Dahlgren, T. Eriksson, *et al.*, "A Low-Complexity Distributed-MIMO Testbed Based on High-Speed Sigma–Delta-Over-Fiber", *IEEE Trans. Microw. Theory Techn.*, vol. 67, no. 7, pp. 2861–2872, Jul. 2019.

[7] H. Q. Ngo, A. Ashikhmin, H. Yang, E. G. Larsson, and T. L. Marzetta, "Cell-free massive mimo versus small cells", *IEEE Transactions on Wireless Communications*, vol. 16, no. 3, pp. 1834–1850, 2017.

[8] S. Hu, F. Rusek, and O. Edfors, "Beyond Massive MIMO: The Potential of Data Transmission With Large Intelligent Surfaces", *IEEE Transactions on Signal Processing*, vol. 66, no. 10, pp. 2746–2758, 2018.

[9] A. Moerman, J. Van Kerrebrouck, O. Caytan, *et al.*, "mmWave-over-Fiber Distributed Antenna Systems for Reliable multi-Gbps Wireless Communication", in *URSI AT-AP-RASC*, Gran Canaria, Spain, 2022, pp. 1–4.

[10] C. Lim, A. Nirmalathas, M. Bakaul, *et al.*, "Fiber-Wireless Networks and Subsystem Technologies", *J. Lightw. Technol.*, vol. 28, no. 4, pp. 390–405, Feb. 2010.

[11] C.-Y. Wu, H. Li, J. Van Kerrebrouck, *et al.*, "Distributed antenna system using sigma-delta intermediate-frequency-over-fiber for frequency bands above 24 GHz", *J. Lightw. Technol.*, vol. 38, no. 10, pp. 2765–2773, May 2020.

[12] L. Bogaert, J. Van Kerrebrouck, H. Li, *et al.*, "SiPhotonics/GaAs 28-GHz Transceiver With Reflective EAM for Laser-Less mmWave-Over-Fiber", *J. Lightw. Technol.*, vol. 39, no. 3, pp. 779–786, 2021.

[13] C. Fager, T. Eriksson, F. Barradas, K. Hausmair, T. Cunha, and J. C. Pedro, "Linearity and efficiency in 5G transmitters: New techniques for analyzing efficiency, linearity, and linearization in a 5G active antenna transmitter context", *IEEE Microw. Mag.*, vol. 20, no. 5, pp. 35–49, May 2019.

[14] C.-X. Wang, J. Bian, J. Sun, W. Zhang, and M. Zhang, "A survey of 5G channel measurements and models", *IEEE Commun. Surveys Tuts.*, vol. 20, no. 4, pp. 3142–3168, Aug. 2018.

[15] J. L. Corral, J. Marti, and J. M. Fuster, "General expressions for IM/DD dispersive analog optical links with external modulation or optical up-conversion in a Mach-Zehnder electrooptical modulator", *IEEE Trans. Microw. Theory Techn.*, vol. 49, no. 10, pp. 1968–1976, Oct. 2001.

[16] C. H. Cox, E. I. Ackerman, G. E. Betts, and J. L. Prince, "Limits on the performance of RF-over-fiber links and their impact on device design", *IEEE Trans. Microw. Theory Techn.*, vol. 54, no. 2, pp. 906–920, Feb. 2006.

[17] M. U. Hadi, H. Jung, S. Ghaffar, P. A. Traverso, and G. Tartarini, "Optimized digital radio over fiber system for medium range communication", *Opt. Commun.*, vol. 443, pp. 177–185, Mar. 2019.

[18] Y. Tian, K.-L. Lee, C. Lim, and A. Nirmalathas, "60 GHz analog radio-over-fiber fronthaul investigations", *J. Lightw. Technol.*, vol. 35, no. 19, pp. 4304–4310, Oct. 2017.

[19] J. James, P. Shen, A. Nkansah, X. Liang, and N. J. Gomes, "Nonlinearity and noise effects in multi-level signal millimeter-wave over fiber transmission using single and dual wavelength modulation", *IEEE Trans. Microw. Theory Techn.*, vol. 58, no. 11, pp. 3189–3198, Nov. 2010.

[20] C. Vagionas, E. Ruggeri, A. Tsakyridis, *et al.*, "Linearity Measurements on a 5G mmWave Fiber Wireless IFoF Fronthaul Link with analog RF beamforming and 120 degrees steering", *IEEE Commun. Lett.*, vol. 24, no. 12, pp. 2839–2843, Dec. 2020.

[21] L. Breyne, G. Torfs, X. Yin, P. Demeester, and J. Bauwelinck, "Comparison Between Analog Radio-Over-Fiber and Sigma Delta Modulated Radio-Over-Fiber", *IEEE Photon. Technol. Lett.*, vol. 29, no. 21, pp. 1808–1811, Nov. 2017.

[22] I. Lima de Paula, S. Lemey, D. Bosman, *et al.*, "Cost-effective high-performance air-filled SIW antenna array for the global 5G 26 GHz and 28 GHz bands", *IEEE Antennas Wireless Propag. Lett.*, vol. 20, no. 2, pp. 194–198, Feb. 2021.

[23] I. Lima de Paula, L. Bogaert, O. Caytan, *et al.*, "Air-Filled SIW Remote Antenna Unit With True Time Delay Optical Beamforming for mmWave-Over-Fiber Systems", *Journal of Lightwave Technology*, vol. 40, no. 20, pp. 6961–6975, 2022.

[24] L. Van Messem, A. Moerman, O. Caytan, *et al.*, "A 4 × 4 Millimeterwave-Frequency Butler Matrix in Grounded Co-Planar Waveguide Technology for Compact Integration With 5G Antenna Arrays", *IEEE Transactions on Microwave Theory and Techniques*, vol. 71, no. 1, pp. 122–134, 2023.

[25] Q. Zhang, J. Ji, Q. Cheng, *et al.*, "Two-dimensional phased-array receiver based on integrated silicon true time delay lines", *IEEE Trans. Microw. Theory Techn.*, early access. doi: 10.1109/TMTT.2022.3214482.

[26] U. Gliese, K. Colladay, A. S. Hastings, D. A. Tulchinsky, V. J. Urick, and K. J. Williams, "RF Power Conversion Efficiency of Photodiodes Driven by Mach–Zehnder Modulators", *IEEE Trans. Microw. Theory Techn.*, vol. 58, no. 11, pp. 3359–3371, Nov. 2010.

[27] T. Young, J. Conradi, and W. Tinga, "Generation and transmission of FM and $\pi/4$ DQPSK signals at microwave frequencies using harmonic generation and optoelectronic mixing in Mach-Zehnder modulators", *IEEE Trans. Microw. Theory Techn.*, vol. 44, no. 3, pp. 446–453, Mar. 1996.

[28] U. Gliese, S. Norskov, and T. Nielsen, "Chromatic dispersion in fiber-optic microwave and millimeter-wave links", *IEEE Trans. Microw. Theory Techn.*, vol. 44, no. 10, pp. 1716–1724, Oct. 1996.

[29] H. Shams, P. M. Anandarajah, P. Perry, and L. P. Barry, "Optical generation of modulated millimeter waves based on a gain-switched laser", *IEEE Trans. Microw. Theory Techn.*, vol. 58, no. 11, pp. 3372–3380, Mar. 2010.

[30] K. Yavuz Kapusuz, A. Vanden Berghe, S. Lemey, and H. Rogier, "Partially Filled Half-Mode Substrate Integrated Waveguide Leaky-Wave Antenna for 24 GHz Automotive Radar", *IEEE Antennas Wireless Propag. Lett.*, vol. 20, no. 1, pp. 33–37, Jan. 2021.

[31] C. H. Cox, "Noise in links", in *Analog Optical Links: Theory and Practice*, Cambridge, UK: Cambridge University Press, 2004, ch. 5, sec. 2, pp. 160-168.

[32] Y. Yang, C. Lim, and A. Nirmalathas, "Multichannel Digitized RF-Over-Fiber Transmission Based on Bandpass Sampling and FPGA", *IEEE Trans. Microw. Theory Techn.*, vol. 58, no. 11, pp. 3181–3188, Nov. 2010.

[33] 3GPP, *LTE; Evolved Universal Terrestrial Radio Access (E-UTRA); Base Station (BS) radio transmission and reception - Release 15 - v 15.3.0*, Tech. Rep. TR 36.104, Jan. 2021. [Online]. Available: `https://www.3gpp.org/dynareport/36-series.htm`.

[34] Y. Li, Y. Zhang, and Y. Huang, "Any Bias Point Control Technique for Mach–Zehnder Modulator", *IEEE Photon. Technol. Lett.*, vol. 25, no. 24, pp. 2412–2415, Dec. 2013.

[35] S. Walklin and J. Conradi, "Effect of Mach-Zehnder modulator DC extinction ratio on residual chirp-induced dispersion in 10-Gb/s binary and AM-PSK duobinary lightwave systems", *IEEE Photon. Technol. Lett.*, vol. 9, no. 10, pp. 1400–1402, Oct. 1997.

[36] R. H. Stolen, "Nonlinearity in fiber transmission", *Proc. IEEE*, vol. 68, no. 10, pp. 1232–1236, Oct. 1980.

[37] E. Ruggeri, A. Tsakyridis, C. Vagionas, *et al.*, "A 5G Fiber Wireless 4Gb/s WDM Fronthaul for Flexible 360º Coverage in V-Band massive MIMO Small Cells", *J. Lightw. Technol.*, vol. 39, no. 4, pp. 1081–1088, Feb. 2021.

5

mmWave Distributed Antenna Systems for Interactive VR: Resolving Blockage Loss, Reducing Exposure, Antenna System Design

Based on "mmWave Distributed Antenna Systems for Interactive VR: Reducing Blockage and Exposure, Enhancing Robustness with (AF)SIW Antennas" by Arno Moerman, Olivier Caytan, Hendrik Rogier and Sam Lemey, as submitted to the bioelectromagnetics column from Antennas & Propagation Magazine.

In this chapter, mmWave-over-fiber-based distributed antenna systems are showcased to realize reliable high-datarate wireless links for demanding applications such as interactive virtual reality where line-of-sight blockage due to the presence of the users' own body and external (human) blockers frequently occurs. Distributed architectures, such as distributed antenna systems (DASs) pose a good solution to alleviate these losses, while keeping the background exposure low. Additionally, (air-filled) substrate integrated waveguide antenna topologies are compared to dipole and patch antennas and found to be more robust in close proximity to the body, both in terms of bio-electromagnetic effects and communication performance. Finally, a practical demonstration of the mmWave DAS with headmount user equipment exhibits reliable 12 Gbps wireless links in the n257 band under full rotation and head-tilting of the user. By leveraging DMIMO techniques, the throughput can even be raised to 24 Gbps.

5.1 Introduction

Future wireless systems will perform joint communication and sensing functions [1]. Both services are pushing towards higher frequency bands, such as the sub-millimeter (7 GHz–30 GHz) and mmWave frequency spectrum (30 GHz–300 GHz), since, on the one hand, the larger available bandwidths provide higher resolution to radar technology. On the other hand, from a communication perspective, this unoccupied spectrum allows serving a massive amount of users with high-datarate ultra-reliable low-latency communication (URLLC), enabling the Internet of Everything. Mainly tactile applications require those URLLC high-throughput wireless links with integrated sensing for fast and accurate feedback. They are mainly deployed indoor and comprise holographic telepresence, remote surgery, remote control of heavy machinery, or applications with more users such as extended reality, virtual reality, or augmented reality (XR/VR/AR) [2], [3]. They rely on total air-interface latencies below 100 µs and per user data-rates in the order of giga-bits per second (Gbps) [3], to avoid motion sickness with headmount devices (HMDs).

The exploitation of higher frequency bands, however, brings forth higher penetration losses and more adverse propagation conditions. In combination with indoor environments with abundant furniture and applications involving many simultaneous users, frequent non-line-of-sight events can seriously deteriorate the wireless link. Promising solutions, such as reconfigurable intelligent surfaces (RIS) [4], mmWave distributed antenna systems (DAS) [5], and large intelligent surfaces (LIS) [6], [7] have been proposed to tackle these harsh propagation conditions. Yet, there is no clear overview of the pitfalls and advantages attributed to these systems from a bio-electromagnetic perspective. In applications such as mobile phones for communication, wearable vital sign monitoring sensors, body area networks with smart glasses, and head-mounted devices with integrated communication and sensing, the device's antennas are in close proximity to the body [8]. Several studies focus on these body-centric antenna applications, with most concentrating on antenna topologies that maintain their characteristics for good communication in close proximity to a human [8], [9]. Other studies do consider bio-electromagnetic metrics, examining whether exposure limits the effective isotropic radiated power of antennas [10], [11]. However, body-centric communication systems are inherently multidisciplinary and should be studied accordingly.

In this chapter, DASs are rigorously analyzed to overcome the blockage loss at mmWave frequencies induced by other human users. The practical

roll-out of a mmWave-over-fiber-based DAS is approached from both a bio-electromagnetic and communication perspective in a tutorial-like fashion. First, in Section 5.2, a concise, but thorough investigation is performed to quantify blockage loss caused by the users' own body and external blockers. Different solutions to these problems mentioned in literature are compared to state-of-the-art solutions, often encountered in beyond-5G literature. Next, Section 5.3 compares two air-filled substrate integrated waveguide antennas with standard patch and dipole antennas to identify suitable antenna topologies for body-centric communication. To achieve this, a new metric is proposed that merges both communication-related criteria and bio-EM perspectives. For this, not solely bio-EM and communication related criteria are considered. Instead, a metric is proposed that combines both the communication and bio-EM perspectives. The analyses performed in the previous sections are then linked to higher-level system specifications, such as error-vector magnitude (EVM) in Section 5.4, where a practical DAS is realized in an AR/VR scenario, deploying an HMD user equipment (UE). A DAS, combined with a distributed array at the UE, is proposed to overcome aforementioned blockage problems and to realize a stable, high-throughput wireless system. Finally, Section 5.5 concludes the chapter.

5.2 Distributed Antenna Systems Countering Blocking Problems at mmWave Frequencies

The shift to mmWave frequencies offers abundant bandwidth for high-data-rate communication and enhanced-resolution sensing. However, it faces significant challenges due to harsh propagation conditions, including increased path loss, higher penetration loss, and more severe shadowing regions. This is even more pronounced for body-centric wireless systems, where shadowing zones over the receiving antennas are caused by both external obstacles, and self-blocking due to the human body. In this section, the severity of this blockage loss is quantified based on a literature review. Furthermore, several solutions are discussed and compared for deployment in future beyond-5G networks. Included in this comparison is the mmWave-over-fiber DAS proposed in [5], providing a promising pathway for the practical realization of these solutions.

Table 5.1: Measured maximum body blockage losses reported in literature for indoor environments at mmWave frequencies.

5G NR Bands	Reference	Frequency Band	Environment	# of Blockers	HPBW (Azimuth)		Max. Blockage Loss
					BS	UE	
n257 n258 n261	[12]	26 GHz	Indoor	1–3	10°	10°	28 dB
	[13]	27 GHz	Indoor	1–4	10°*	360°	16 dB
	[14]	28 GHz	Anechoic	1	360°	10°	20 dB
	[15]	28 GHz	Indoor	1	/	/	20-30 dB
	[16]	30 GHz	Indoor	1–3	30°	30°	30 dB
n259 n260	[12]	39.5 GHz	Indoor	1–3	10°	360°	34 dB
n263	[14]	60 GHz	Anechoic	1	360°	10°	24 dB
	[17]	60 GHz	Indoor	1–3	20°**	20°**	32 dB
	[18]	60 GHz	Indoor	1–7	12°	12°	40 dB

* The channel is obtained by averaging over 3 spatially diverse channels.
** Estimated based on the phased array topology and size.
*** Half-power beamwidth (HPBW), base station (BS), user equipment (UE)

5.2.1 Blockage Loss at mmWave Frequencies

In recent years, significant research efforts have been devoted to the theoretical analysis of radiowave propagation and channel measurements at mmWave frequencies [19], [20]. This study gives an overview of channel measurement campaigns in indoor environments at mmWave frequencies (24.25 GHz–74.52 GHz), where one or more human blockers are present in between base station (BS) and UE, with the aim of quantifying these body blocking problems. The maximum blockage loss is defined as the additional channel loss introduced by blockage. Table 5.1 provides an overview of these studies and lists the maximum measured blockage loss, clearly proving the severity of human-induced wireless link blockage. The studies were performed in different mmWave frequency regions of interest, being the 5G n257, n258 and n261 bands spanning the 24.25 GHz–29.5 GHz frequency range, the n260 band covering the 37 GHz–43.5 GHz range, the n263 band extending over 57 GHz–71 GHz, and the 60 GHz 802.11ay Wi-Fi standard spanning over 57.24 GHz–74.52 GHz. As listed, other important factors that impact the blockage loss include the number of introduced blockers and the half-power beamwidth (HPBW) of the antennas at BS and UE. [14], [16] also fit models based on the performed measurements to expand the blockage models in the TS 38.901 3GPP specification [21].

Based on these measurement campaigns, following additional observations were made. In [14], the blockage loss is measured for different orientations of various users to demonstrate how variations in human morphology affect this loss. The study concludes that the blockage loss depends on the width, height and thickness of the blocker, with losses increasing when test persons with larger cross-sections obstruct the wireless link. The measured blockage loss at 60 GHz was up to 13 dB higher for a person with an average body width of 0.51 m compared to a person with an average body width of 0.41 m. Depending on whether the blockers are orientated sideways or frontal, the excess blockage loss also varies up to 5 dB at 28 GHz.

Additionally, Table 5.1 shows that the blockage loss generally increases with frequency from [16 dB–30 dB] at 28 GHz [13] to [24 dB–40 dB] at 60 GHz [18]. Yet, by increasing frequency, the cross section of the first Fresnel zone is reduced in size, resulting in a blockage loss reduction of more than 10 dB at 28 GHz by increasing the BS antenna height [14].

Most measurements yield a large maximum blockage loss due to the use of directive antenna systems [12], [16], [18]. While these are typically used in mmWave setups to mitigate higher path loss, they also make the

link more prone to line-of-sight blockages. In contrast, the authors of [13] use an omnidirectional UE antenna and observe that non-line-of-sight multipath components limit the blockage loss, resulting in a maximum excess loss of 16 dB. While deploying omnidirectional antennas at mmWave frequencies reduces maximum blockage loss, it also diminishes the wireless link budget in line-of-sight scenarios. Moreover, the wireless link becomes more vulnerable to signal quality degradation in multipath environments, as multipath components are not filtered out as they are with directional antenna systems. This leads to higher delay spread and potential wireless channel fading or inter-symbol interference [22].

In terms of position of the human blockers with respect to the BS or UE, it is found that the maximum blockage loss is higher when the blocker is closer to the BS or UE [16]. This is confirmed by [15], where the UE is positioned as a handheld device on a user. In this case, an excess blockage loss of 20-30 dB is measured at 28 GHz.

Finally, in [18], also the temporal channel data are gathered, and 90 % of blockage events with less than 4 blockers last longer than 340 ms increasing to 470 ms for at least 4 users.

Overall, this study highlights that the link budget may be severely impacted when maximum blockage loss occurs, potentially rendering the link unusable. Even in cases of smaller blockage losses caused by partial obstructions, the reliability of high-data-rate mmWave wireless communication remains at risk, posing significant challenges for future applications, such as AR/VR/XR.

5.2.2 Solutions to Overcome Blockage Problem

To mitigate the impact of blockages, multiple solutions were proposed in literature [4], [6], [7], [14], [23]–[27]. Two, albeit suboptimal, solutions that are relatively easy to implement include using flexible bandwidth-time allocations in software (also known as flexible numerology in 5G new radio) and increasing the height of the access point [14], [24], [25]. Using flexible numerology for different blockage conditions achieves small throughput gains when tweaked accordingly, but does intrinsically not overcome the shadowing problem [23]. Increasing the access point height lowers the blockage loss as confirmed by measurements in [14] and by theoretical models in [24] and [25]. Yet, in indoor environments, there is a practical limit on the access point height.

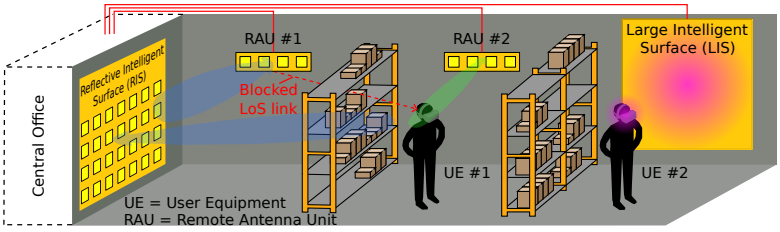

Figure 5.1: Introduction of macro diversity in wireless systems to avoid signal loss by external blockers between central office and user equipment (UE). (Left) Line-of-sight blocked from access point/Remote Antenna Unit (RAU) #1 to UE #1, with reconfigurable intelligent surface (RIS) redirecting the signal towards the UE. (middle) Installing multiple access points/RAUs also restores line-of-sight path to UE #1. Depending on the environment, both concepts can be combined to realize a distributed MIMO (DMIMO) system. (right) A contiguous radiating surface (called large intelligent surface (LIS)) is able to perform holographic beamforming, focusing the energy in a confined region around UE #2.

However, the most promising solution encountered in these studies is macro diversity, which includes an increase in base station density to counter blockages [24]. The macro diversity solution also aligns with recent advancements in future networks, such as the fifth and sixth generation (5G/6G) network, and can be implemented in three different ways: (1) reconfigurable intelligent surfaces [4], (2) cell-free or distributed MIMO (DMIMO) systems [26], [27], and (3) large intelligent surfaces [6], [7]. These are illustrated in Figure 5.1, showing a realistic indoor environment rich of blockers and two users with an HMD. The remote antenna unit (RAU) #1 on the left suffers from a line-of-sight blockage to UE #1. However, a RIS, consisting of a large number of tunable reflectors, is able to overcome the shadowing problem by scattering the incoming beam towards the UE. Alternatively, a distributed antenna system (DAS), implementing cell-free MIMO or DMIMO, solves the line-of-sight blockage by switching to RAU #2, capable of setting up a link with better quality. Additionally, when multiple RAUs offer a good link to the UE, MIMO techniques may be used to further increase reliability and/or throughput of the system. On the right side, a LIS is shown, being a large contiguous radiating surface performing holographic beamforming by realizing a 3-dimensional interference pattern to focus the energy in a confined 3D hotspot around UE #2 by meticulously tuning the phases and amplitudes of the radiating elements. All three solutions require

tight control to either switch between RAUs, or to calculate and apply the correct phase and/or amplitudes to the signals. A DAS and LIS also require coherent distribution of the mmWave signals. This is performed in a central office (CO), indicated on the far left of the figure.

These three concepts can also be compared from a communication and exposure point of view, even though literature on the latter is still sparse. An advantage of installing RISs in the UE's environment is that they do not require a wired mmWave connection, making their deployment a more cost-effective densification strategy compared to adding additional base stations. To achieve comparable signal-to-noise ratios, however, they need to be larger than more traditional direct-and-forward antenna array relays [28]. In [29], a scheme is proposed for a RIS that reduces the combined normalized exposure by 20 %. The ETSI standardization committee states that compliance with electromagnetic fields (EMF) requirements should be checked when a RIS is involved in the environment [30]. Yet, no definitive guidelines regarding EMF when deploying a RIS have been formulated. Overall, not many studies investigate the exposure and background EMF for a RIS-based architecture, leaving lots of room for further exploration. In general, distributed approaches, such as a DAS, implementing DMIMO, allow for increased data rates and more efficient energy usage, while limiting inter-user interference and mitigating signal attenuation at cell edges, when compared to co-located approaches [27], [31]. In a distributed setup, switching to the RAU with the best link quality reduces background exposure owing to the smaller average user-RAU distance, allowing lower transmit powers. Additionally, when multiple RAUs collaborate in a synchronized manner by applying DMIMO techniques, it is found that distributed approaches yield more compact, accurate and consistent hotspots, while also reducing the background EMF [32].

Because of the favorable communication and exposure characteristics of a distributed system, the remainder of this study focuses on a mmWave-over-fiber DAS [5], as a solution to implement a DMIMO system in a realistic deployment scenario. When rolled out on a large scale, this setup could even approach a LIS. The key to realize this system is the low-loss distribution of high-frequency signals from CO to RAUs via a mmWave-over-fiber architecture, as shown in Figure 5.2. In this approach, a mmWave signal is directly modulated on a light carrier using an electro-optical modulator. The modulated light signal propagates through a fiber with very low losses, after which it is converted back to the electrical domain. The electrical signal is then amplified by low-noise amplifiers and power amplifiers to drive an antenna. The mmWave-over-fiber architecture is chosen since

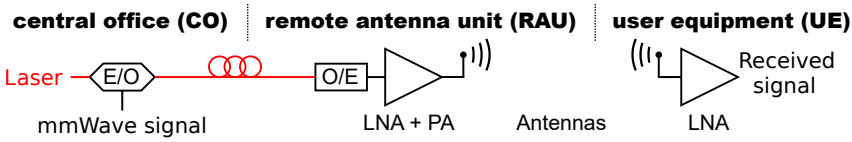

Figure 5.2: mmWave-over-fiber wireless link: mmWave signals are modulated on the laser carrier by electro-optical (E/O) modulators. The optical signal is transformed back to the electrical domain by an opto-electrical (O/E) converter. Low-noise and power amplifiers (LNAs/PAs) amplify the signal before wireless transmission. At the user equipment (UE), the wireless signal is amplified and demodulated.

it inherently offers more bandwidth and a simpler RAU architecture over sigma-delta-over-fiber and digitized-radio-over-fiber [33], paving the way to a large-scale roll-out for reliable high-datarate DASs. More details of the mmWave-over-fiber architecture are described in [34].

5.3 mmWave Antennas for Body-Centric Communication

In the design and analysis of mmWave wireless systems, antenna front-ends are crucial for ensuring an efficient and reliable connection with adequate bandwidth. Moreover, when targeting body-centric applications, such as wireless body area networks with vital sign monitoring, or head-mounted devices with integrated communication and sensing, additional challenges arise. An antenna for communication and sensing must perform well near the human body despite a degraded realized gain pattern, caused by challenges like impedance detuning, radiation efficiency degradation, and directivity pattern deformation. From a bio-EM perspective, the antenna should also minimize exposure to the body. Combining both antenna and bio-EM perspectives, it is crucial to ensure antenna exposure stays within safety limits, particularly given the high transmit power needed to compensate the increased path loss in future mmWave networks.

While plenty of literature discusses body-centric antennas at mmWave frequencies, their focus is mostly on these sub-problems, whereas a multi-disciplinary approach is required. Most papers [8], [9] concentrate on antenna design from a communications point of view, conceiving antenna topologies that maintain performance when operated in close proximity to

the body. In [8], several state-of-the-art antenna arrays are compared in terms of wireless communication and user comfort perspective. When the focus is more on EM exposure due to on-body antennas, often idealized antennas, such as dipoles, or patch antennas [35], [36] are used as EMF source. These idealized antennas often appear to be the perfect solution from a bio-EM point of view, yet when considering communication, they bring along several disadvantages. A single resonator patch typically does not offer enough bandwidth to cover most commercial mmWave bands and idealized patch-based topologies often have uninterrupted ground planes [8], [36], restricting the interfacing to front-end ICs. In [37], it is shown that the feeding technique of patch antennas has a large influence on the exposure, resulting in a reduced average exposure level of uninterrupted ground planes by a factor of 8. Additionally, these topologies also suffer from the lossy dielectric materials encountered at mmWave frequencies. In [10], [11], the authors verify whether the exposure restrictions pose a limitation on the EIRP for slot, notch and patch antenna arrays. However, a holistic approach tackling both communication and exposure perspectives remains unexplored.

In the remainder of this section, four different antenna topologies are compared based on different criteria as a function of the body-to-antenna distance d. Both communication and bio-EM criteria are studied by comparing antenna performance and exposure when the antenna is in close proximity to the body. Additionally, their combined effect on system-level parameters is compared, since this is of great importance to implement a reliable and high-datarate wireless link. More in particular, the patch with an uninterrupted, but finite ground plane, and the dipole without ground plane are compared to two antennas implemented in air-filled substrate-integrated-waveguide (AFSIW), also known as empty substrate-integrated-waveguide, technology [38]–[42]. The latter antennas have been selected as they possess great potential to address several of the aforementioned problems. By replacing the dielectric substrate by an air cavity, they achieve near-100% radiation efficiency. Moreover, by confining the fields to judiciously designed air-filled cavities, compact arrays with low mutual coupling can be realized, thereby achieving near platform-independent operation [38], [40]. Finally, large bandwidth operation can be achieved through the use of an air substrate and multi-mode bandwidth enhancement techniques [38], [41], [42]. All four antennas are designed to operate in the n257 FR2 frequency band ((26.5–29.5) GHz) and to fit in the same near-half-wavelength footprint of $7\times7\,\text{mm}^2$ ($0.65\,\lambda\times0.65\,\lambda$ at 28 GHz), to ensure fair comparison. The latter also guarantees optimal array performance

with a grating-lobe-free steering range of ±32° at 28 GHz. Although flexible counterparts of the patch and dipole antennas exist [8], all antennas were simulated on a rigid PCB substrate for fair comparison. The conclusions from the current analysis also apply to their flexible counterparts, with the exception of additional challenges, such as bending and wrinkling [8]. Figure 5.3 shows a top and side view of each studied antenna together with their front-to-back ratio (FTBR) and maximum directivity in the back hemisphere (D_{rear}) at 28 GHz. The patch and the omnidirectional dipole antenna are both designed on a 0.508 mm-thick low-loss RO4350B substrate. The first AFSIW antenna consists of an aperture-fed patch with an air-cavity in between. The aperture feeding is realized using a grounded coplanar waveguide transmission line. The antenna dimensions are taken exactly from [41]. The second AFSIW antenna uses a dielectric-filled SIW feed to improve the front-to-back ratio (FTBR) from 12 dB to 20.4 dB at 28 GHz. This topology is copied exactly from [42]. The SIW feed transitions to a grounded coplanar waveguide transmission line by using a magnetic dipole, serving as an interface to ICs. In this contribution, the first and second AFSIW antenna are referred to as low-FTBR AFSIW and high-FTBR AFSIW, respectively, for that reason.

All four antennas, including a $5\times5\,cm^2$ 3-layer skin model, are simulated using CST Microwave Studio's Frequency Solver [35]. The antennas are placed at a distance d from the body model. The employed simulation setup and the relevant parameters are shown in Figure 5.4.

5.3.1 Robustness to Body Proximity

A crucial factor in evaluating antennas for communication and sensing purposes is their realized gain pattern $G_{realized}(\theta,\phi)$ [43]. It is a measure scaling their directivity pattern $D(\theta,\phi)$ with their mismatch factor $(1-|S_{11}|^2)$ and their radiation efficiency (η):

$$G_{realized}(\theta,\phi) = (1-|S_{11}|^2)\cdot\eta\cdot D(\theta,\phi). \tag{5.1}$$

In the remainder, these three characteristics are examined in more detail when deployed on the 3-layer skin model [35].

Figure 5.5 presents the simulated reflection coefficient $|S_{11}|$ for the different antenna topologies deployed at various distances d from the three-layer skin model. Owing to its uninterupted ground plane, the patch antenna features

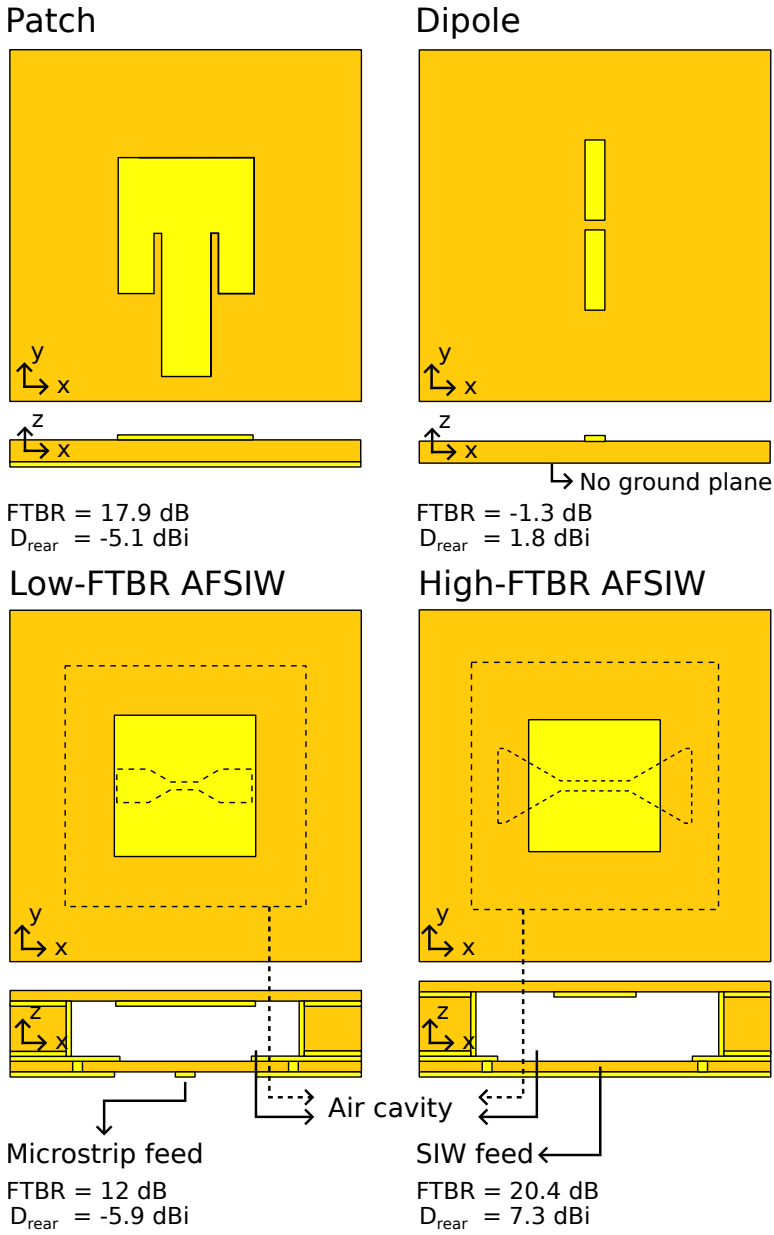

Figure 5.3: Four different antenna topologies with equal footprint of $7\times7\,\mathrm{mm}^2$ ($0.65\,\lambda\times0.65\,\lambda$ at 28 GHz) are studied: A conventional inset-fed patch and dipole as typically considered in most bio-EM exposure-related research, and two air-filled substrate-integrated-waveguide (SIW) antennas as state-of-the-art solutions [41], [42], featuring a large bandwidth, and near-100% radiation efficiency.

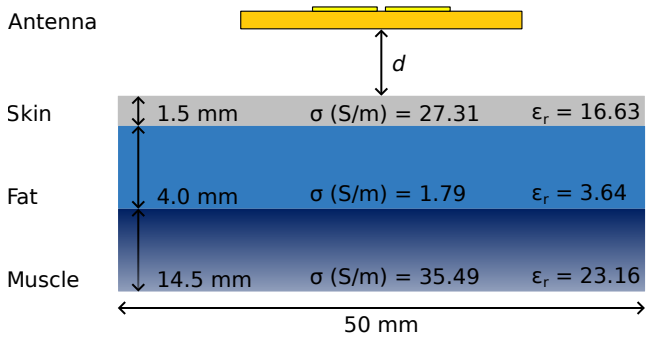

Figure 5.4: Simulation setup to assess the absorbed power density S_{ab}. The antenna ($7\times7\,mm^2$) is deployed at distance d from a 3-layer skin model ($50\times50\,mm^2$) [35]. Dielectric properties for the 3-layer skin model assumed to be constant in the n257 band for this study.

stable matching. Yet, it does not cover the entire frequency band. Both the omnidirectional dipole antenna and the low-FTBR AFSIW antenna (FTBR = 12 dB) cover the full band initially, but fail to meet the -10 dB matching criterion at distances d below 0.5 mm due to their lower FTBR. The high-FTBR AFSIW antenna (FTBR = 20.4 dB) remains stable across different distances while covering the target band. Overall, the high-FTBR AFSIW antenna performs best, with all antennas detuning more easily when deployed closer to the body.

Figure 5.6 depicts the radiation efficiency at 28 GHz, as a function of distance d to the body. A decreasing distance to the body results in a reduced radiation efficiency. Since the loss mechanics in the antennas do not change when the antenna gets closer to its integration platform, a decrease in radiation efficiency represents an increase in total power absorbed by the body. Yet, Figure 5.6 also shows that each topology is characterized by a distance above which the radiation efficiency remains constant. This distance seems to be larger for a decreasing FTBR of the topology. The low losses of the high-FTBR AFSIW antenna in stand-alone conditions in combination with its good FTBR result in an excellent robustness of the radiation efficiency in proximity of the body.

Finally, Figure 5.7 provides the directivity patterns of the antennas in the XZ-plane at 28 GHz when deployed on the body model as in Figure 5.4. Now, however, an interference pattern can arise between the direct and

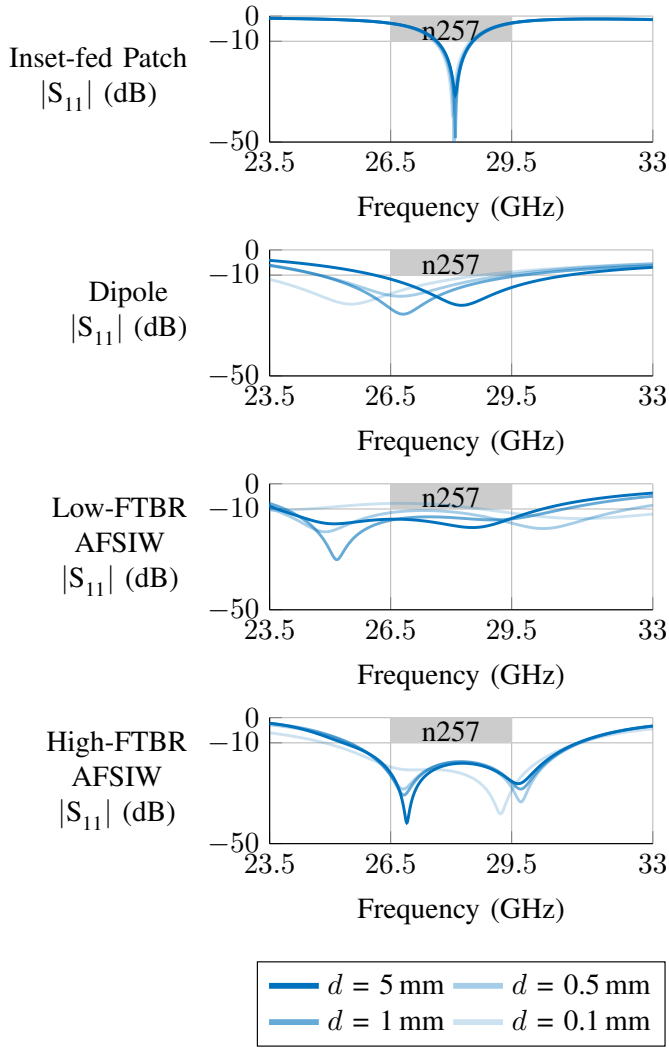

Figure 5.5: Detuning of the different antenna elements for different distances d between antenna and body.

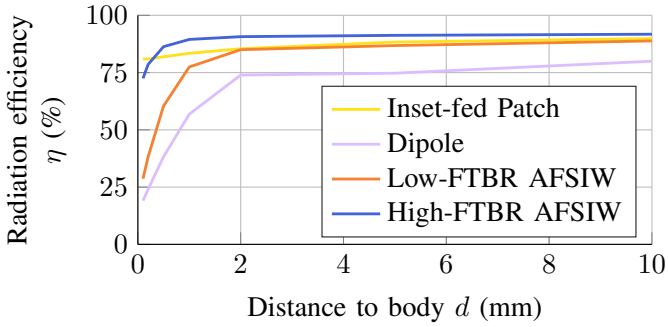

Figure 5.6: Effect of human body on radiation efficiency at 28 GHz. Antennas with a lower front-to-back ratio (FTBR) suffer more from radiation efficiency degradation.

scattered wave. As such, it is important to check the maximum radiated power by the stand-alone antenna in the back hemisphere D_{rear} to estimate the susceptibility to directivity pattern deformation. It is found that antennas that radiate more in the back hemisphere suffer more from a degraded directivity pattern when used in close proximity to the human body. In this regard, an omnidirectional antenna, such as a dipole antenna, is not suited. The patch antenna follows with a maximum back directivity in free space of -5.1 dBi. Both AFSIW antennas perform best with a maximum back directivity of -5.9 dBi and -7.3 dBi at 28 GHz, for the low-FTBR and high-FTBR variant, respectively.

While the 3-layer human body model provides a solid indication of the performance of antennas deployed on an average test subject, variations in human body morphology and curvature must also be considered. Yet, as we have shown, antenna topologies with a high antenna-to-human-body isolation may be adopted [44]. The FTBR and D_{rear} are reliable indicators of the isolation between the antenna and the human body. A higher FTBR and a lower D_{rear} indicate improved isolation, resulting in reduced susceptibility of the antenna's directivity pattern, mismatch factor, and radiation efficiency to (variations in) body morphology.

5.3.2 Absorbed Power Density

In 2020, the International Commission on Non-Ionizing Radiation Protection (ICNIRP) updated their exposure guidelines for frequencies above 6 GHz, to prevent adverse health effects on humans [45]. The ICNIRP guidelines

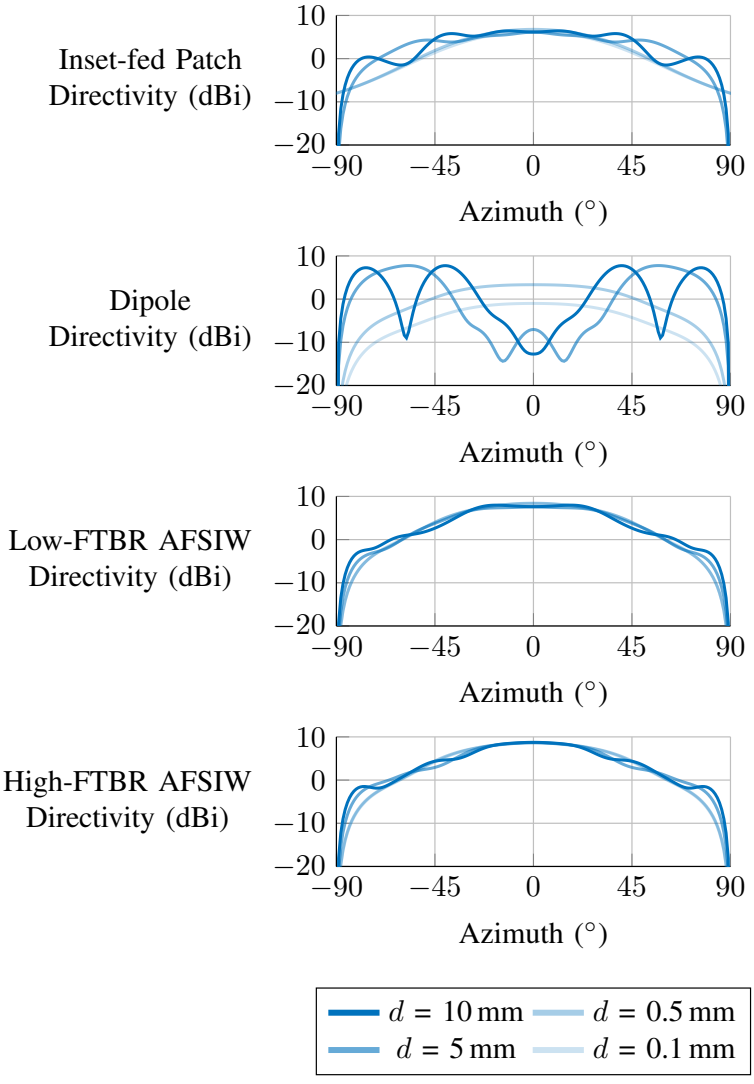

Figure 5.7: Deformation of the directivity patterns at 28 GHz, for different antenna elements and different distances d to the body.

introduce "basic restrictions" on exposure levels, based on the relation between primary exposure effects (such as heating) and adverse health effects (such as pain), including safety margins to take into account biological variation in the population and uncertainty associated with the health science, among others. Since energy above 6 GHz is predominantly absorbed in the superficial tissue of the body (with the penetration depth at 30 GHz being approximately 0.92 mm [45]), the absorbed power density S_{ab}, expressed in W/m^2 is considered. The basic restrictions limit the absorbed power density to $20\,W/m^2$, averaged over a square area of $4\,cm^2$, since this has a good correlation with the local maximum temperature rise, which is the primary effect due to exposure at these frequencies. However, an additional restriction is imposed above 30 GHz, where the absorbed power density should be limited to $40\,W/m^2$, averaged over a reduced square area of $1\,cm^2$, due to the potential use of pencil beams, producing very small focusing areas.

Since these basic restrictions are physical quantities that are not easily measured, "reference levels" are introduced, which are derived from the basic restrictions by applying additional safety factors, considering typical variations between different test persons, such as the influence of clothing [46], [47], or differences in limb curvature [48], where a small radius with respect to the wavelength could increase the total exposure of that limb [48]. The reference level to be restricted concerns the incident power density S_{inc} in both the far-field and the radiative near-field regions. Yet, in the near-field zone, basic restrictions still need to be checked instead. Above 2 GHz, this incident power density should not exceed $10\,W/m^2$ for the general public. It should be noted that, in the far-field region, the absorbed power density boils down to the incident power density compensated by the plane wave mismatch factor between free space and the body [45]. In the near-field, however, this can not be done. Given that, in body-centric communication, the exposure is studied when antennas are in very close proximity to the body, the basic restrictions will be assessed in the remainder of this section.

Figure 5.8 depicts the maximum absorbed power density S_{ab} in the n257 band, averaged over $4\,cm^2$, as a function of the antenna-to-body distance d for the different antenna types, when excited by an input power of 10 mW. As expected, the S_{ab} decreases monotonically for increasing distance. Moreover, the topology with the largest FTBR (20.4 dB at 28 GHz), being the high-FTBR AFSIW, performs slightly better than the patch antenna with an FTBR of 17.9 dB at 28 GHz. Both perform better than the AFSIW antenna with a lower FTBR, and much better than the omnidirectional dipole antenna. Due to the magnetic dipole's fringing fields in the High-FTBR AFSIW antenna, the

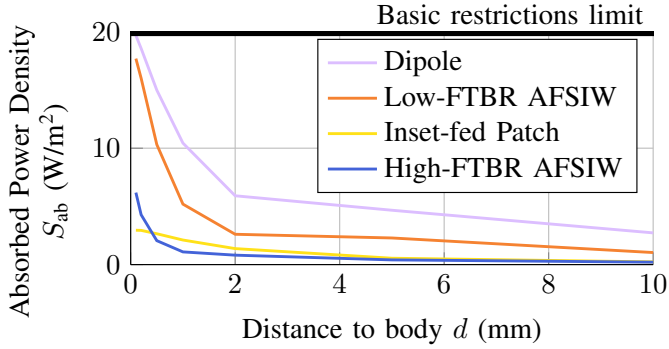

Figure 5.8: Simulation of the absorbed power density averaged over 4 cm^2, for a power input of 10 mW. The maximum absorbed power density value is taken over all frequencies in the n257 frequency band (26.5 GHz-29.5 GHz).

absorbed power density rises above the levels of the patch antenna at distances d below 0.2 mm. To further improve the high-FTBR AFSIW antenna, a stripline feed or substrate-integrated-coaxial-line feed [37], [49] could be considered to fully omit the fringing fields at its substrate-integrated waveguide transition.

5.3.3 Absorbed Power Density in Communication

From a communications perspective, a sufficiently high link budget is crucial to ensure reliable high-data-rate wireless data transfer. In its most strict power class, 3GPP specifies that the EIRP of Handheld UE devices should be between 22.4 dBm and 43 dBm, while the total transmitted power should stay below 23 dBm in the n257 band [50]. To differentiate from the current state of the art, the input power P_{in} is adapted such that the recommended minimum EIRP of 22.4 dBm is achieved. The absorbed power density is then compared for all four topologies to gather more insight into their differences while also taking into account the conclusions from previous subsections. Thereby, a fair comparison between the topologies is made while highlighting the holistic nature of body-centric communication at mmWave frequencies.

Figure 5.9(a) shows the maximum absorbed power density S_{ab} in the n257 band when the input power (Figure 5.9(b)) is set to achieve an EIRP of 22.4 dBm. This power density is averaged over 4 cm^2 and plotted as a function of the distance to the body for different antenna types. Due to the influence of the body on antenna performance, some interesting observations are made.

Overall, the absorbed power density is dominated by the deterioration of the radiation efficiency, which is worse close to the body. Yet, at larger distances, the ripple in the directivity patterns caused by the interference, imposes a lower bound on the absorbed power density since the maximum direction of radiation is not necessarily along broadside anymore, which explains the high absorbed power densities for the dipole at larger antenna-to-body distances. Both AFSIW antennas perform best at both large and smaller distances, with the high-FTBR AFSIW antenna performing slightly better when also considering the required input power to achieve the EIRP. The absorbed power density stays under the basic restrictions limit of $20\,\mathrm{W/m^2}$ for distances above 0.2 mm.

In conclusion to this section, the AFSIW antenna with high FTBR performs the best overall, according to the proposed metric where absorbed power density is studied when scaling the input power to achieve the desired EIRP value, taking both bio-EM and communication criteria into consideration. Moreover, the AFSIW antenna is a suitable candidate to implement body-centric communication owing to its suitability for integration in an antenna array, given its tight footprint of half a wavelength [42] and its high efficiency, even when deployed in close proximity to a human body. As we are now targeting integration into a rigid HMD, the small footprint of the rigid implementation does not impact user comfort. In the future, a flexible implementation of an (AF)SIW antenna, as in [51], [52], would offer even greater benefits, such as enabling the conformal integration of larger antenna arrays and/or the realization of flexible HMDs.

5.4 Practical Roll-out and Measurements

In previous sections, AFSIW technology was proposed as a promising candidate to realize high-performance on-body antennas (Section 5.3) and mmWave-over-fiber-based DASs were introduced to implement macro diversity and, hence, resolve high blockage losses (Section 5.2.2). In this section, we discuss the practical realization of a mmWave-over-fiber DAS and assess its ability to enable reliable, high-data-rate wireless communication with a body-worn HMD leveraging AFSIW antennas. In the case of a rigid body-worn HMD platform, rigid implementations of AFSIW antennas do not impose limitations on user comfort. Applications for a HMD include, but are not limited to, motion tracking in smart glasses or military helmets, communication in body area networks, and off-body communication for

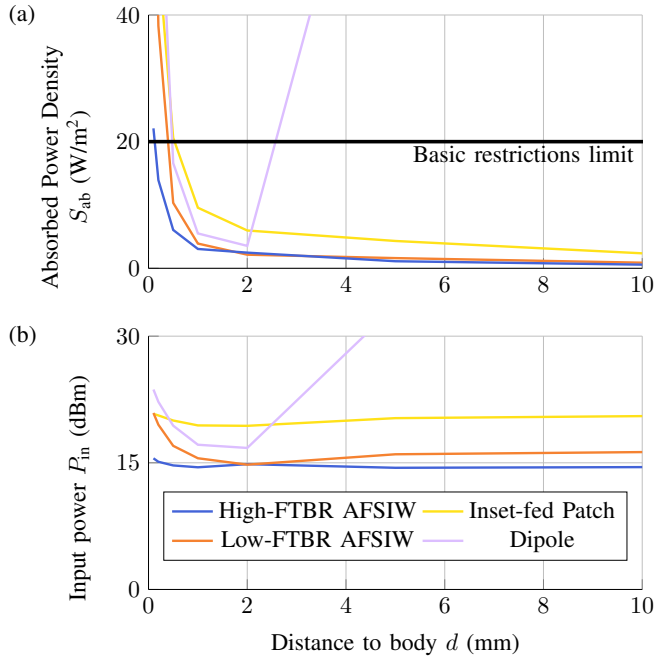

Figure 5.9: (a) Simulation of the absorbed power density averaged over 4 cm^2 when keeping a constant EIRP of 22.4 dBm at broadside. The maximum absorbed power density value is taken over all frequencies in the n257 frequency band. (b) Corresponding input power to achieve the EIRP. Due to their excellent antenna characteristics, AFSIW antennas have the lowest absorbed power density for a given EIRP.

AR/VR/XR. In addition to the resolved blockage loss, we also propose a solution to counter frequent signal degradation due to polarization mismatch when users tilt their heads and we demonstrate that mmWave-over-fiber-based DASs are excellently suited to further increase throughput by leveraging DMIMO techniques.

Figure 5.10 provides a schematic representation of the measurement setup and depicts the practical implementation of the DAS. At the UE side, a homogeneous anthropomorphic SPEAG mmW-HEAD-P10 head phantom for frequencies ranging from 3 GHz to 100 GHz [53] is placed on an NSI-MI phi-over-azimuth rotary positioner in an anechoic chamber. This controlled

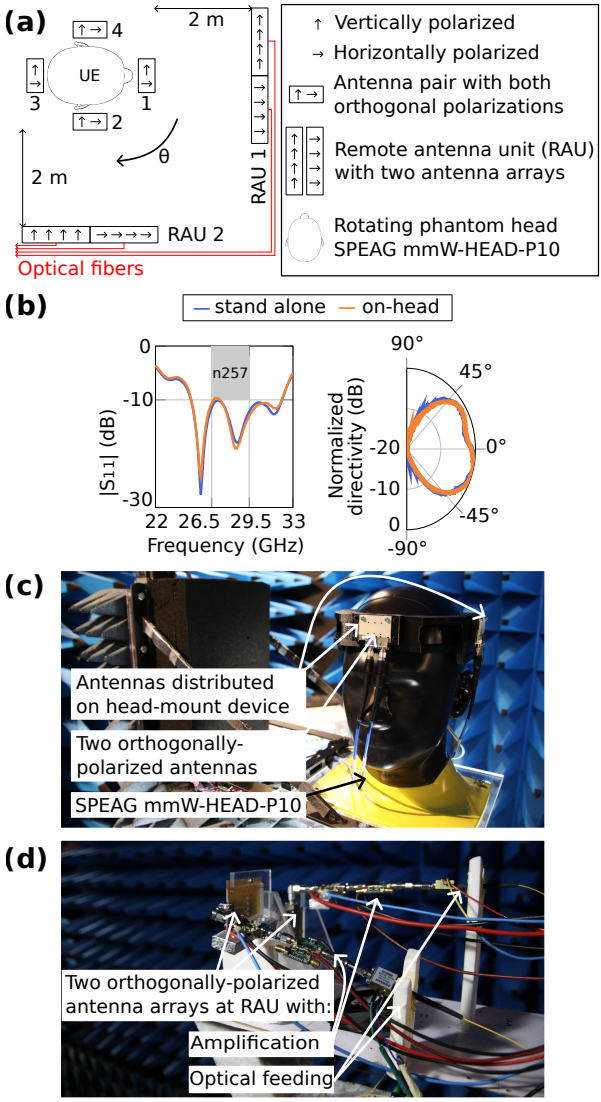

Figure 5.10: (a) Schematic representation of the measurement setup. (b) Influence of the SPEAG phantom head on the antenna's matching and directivity. (c) SPEAG mmW-HEAD-P10 at user equipment (UE) side with head-mount device equipped with orthogonally linearly-polarized antenna pairs, (d) two orthogonally polarized 1×4 antenna arrays at remote antenna unit (RAU) side.

environment enables us to study wireless link loss due to head rotation and tilting, causing self-blockage and polarization mismatch, without interference from external environmental factors such as multipath reflections, which we have previously shown to affect RAU-to-UE link quality in a DAS setup [54]. Sparse multipath channels can, however, in combination with multiple tightly synchronized RAUs enable distributed MIMO communication to increase the total wireless throughput [28]. A 3D-printed HMD is used to uniformly distribute four orthogonally linearly polarized [42] high-FTBR AFSIW antenna pairs on the head UE. Each pair is deployed 10 mm from the head to connect the measurement cables. Figure 5.10(b) shows the measured $|S_{11}|$ and normalized directivity patterns for the high-FTBR AFSIW antenna deployed in free-space stand-alone conditions and on the phantom head, showing that the antenna does not suffer from deployment near the phantom head, owing to its high platform independence. The RAUs, placed at 2 m distance of the HMD, are equipped with two co-located perpendicularly mounted 1×4 corporate-fed antenna arrays. Each array consists of four low-FTBR AFSIW antenna elements and operates in the n257 frequency band. They exhibit a peak gain of 10.1 dBi along broadside [41]. The four RAU antenna arrays are optically fed [5] by the mmWave-over-fiber architecture (Figure 5.2). At the RAU, a low-noise (Analog HMC1040) and power amplifier (Analog HMC943) are used, while at the UE, a general-purpose amplifier (Analog HMC7950) is applied. Additionally, a Mach-Zehnder modulator (Fujitsu FTM7937EZ) is exploited as E/O modulator, and a Finisar XPDV2120R-VF-FA performs the O/E conversion at the RAU.

To assess the system-level performance of the link, the root-mean-square (rms) EVM is used. The lower the rms EVM, the closer the received constallation points are to the ideal constellation, and the higher the signal to interference, distortion and noise ratio is. Additionally, 3GPP determined target rms EVM thresholds linking the signal quality to favorable constellations. For example, an rms EVM below 8 % allows for 64-QAM symbols (6 bits/symbol) to be transmitted [55]. The experiment leverages 2-Gbaud-signals with a root-raised-cosine filter having a roll-off coefficient of 0.35, centered around a 28 GHz carrier frequency to fit within the n257 frequency band.

5.4.1 Overcoming Self-Blockage Loss and Head-Tilting-Induced Polarization Mismatch

Figure 5.11 shows the channel gain $|S_{21}|$, measured between the connectorized UE antenna and RAU antenna array, and the signal quality as a function of

the HMD UE movement.

Figure 5.11(a) focuses on HMD UE rotation and shows that an EVM below 8 % can be guaranteed by switching to the UE antenna with the best signal quality. At $\theta = 0°$, Antenna Pair 1 clearly provides best signal quality as it is perfectly aligned with RAU 1, which is also visible in the wireless channel $|S_{21}|$. However, when the UE turns away from the 0° position towards -55°, the wireless channel $|S_{21}|$ shows that the signal quality is mainly reduced due to the increased wireless link losses caused by a combination of self-blocking and the antenna's directivity pattern. The HMD UE now switches to Antenna Pair 2, since it provides a better wireless link from this position onwards, to maintain the link's EVM below 8 %. Similarly, the HMD UE switches to Antenna Pair 3 at -175° and to Antenna Pair 4 at -295°, to fully mitigate self-blockage. Figure 5.11(b) focuses on the impact of head tilting and shows that polarization mismatch has a severe impact on the link quality. At $\phi = 0°$ (upright head), the vertically polarized UE Antenna Pair 2 experiences good signal quality maintains a good wireless channel with the RAU, resulting in good signal quality (EVM = 5.0 %). When tilting the head by 90°, the polarization mismatch causes the link quality to deteriorate, but by switching to the orthogonally, horizontally polarized Antenna Pair 2 at -40°, good link quality is guaranteed. Theoretically, the cross-over point occurs at -45°, as both polarizations incur a 3-dB penalty due to the mismatch factor. In practice, the cross-over point is indeed 3-dB lower than the maximum, but due to slight misalignments in the setup, this occurs at -40°. This misalignment also results in the minimum transmission strength (orthogonal position) aligning with -85° and 5°.

By comparing the wireless channel $|S_{21}|$ with the signal quality, we conclude that the loss is primarily determined by the increased link losses, and that the cross-over points are well predicted. This experiment shows that exploiting spatial and polarization diversity at the HMD is sufficient to achieve a reliable high-data-rate link. By switching to the UE's antenna with the best link quality, through selection combining, a total throughput of 12 Gbps can be maintained in the n257 frequency band for all realistic positions of the phantom head.

Introducing polarization and spatial diversity at the UE overcomes self-blockage and polarization mismatch. However, as demonstrated in Section 2.1, external blockers can still significantly degrade the link budget between a single RAU and the UE. To mitigate this, strategically deploying additional RAUs, as illustrated in Figure 10(a), enhances the system's resilience against external blockages. If a blocker compromises the link quality by obstructing

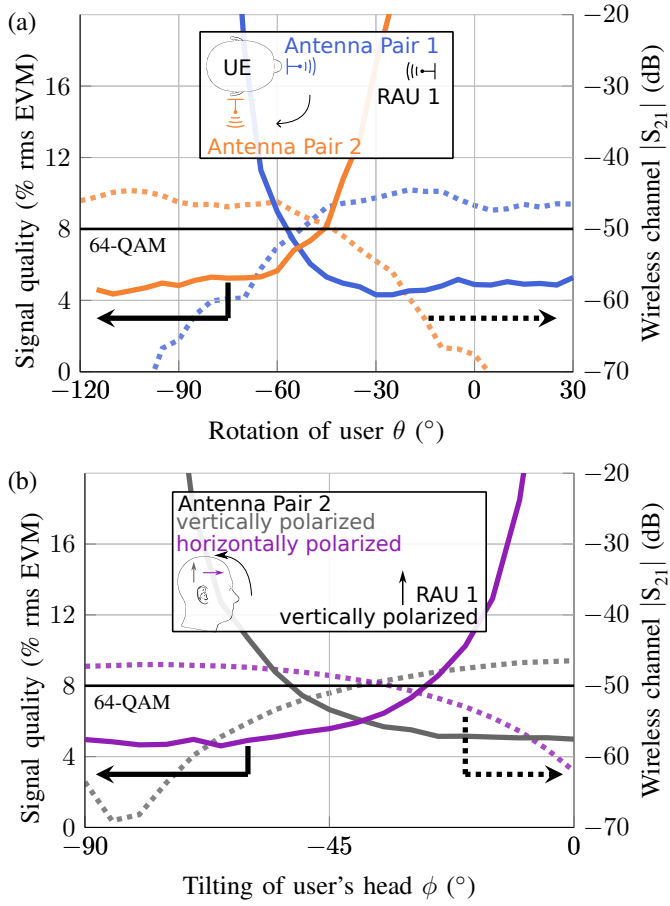

Figure 5.11: Signal quality (solid line) and channel gain (dotted line) of a vertically polarized remote antenna unit (RAU), transmitting signals to a head-mount device (HMD) user equipment (UE) with four orthogonally linearly polarized antenna pairs. Switching to the UE antenna with best signal quality mitigates the impact of self-blocking (a) and tilting of the head (b), guaranteeing a 12 Gbps link.

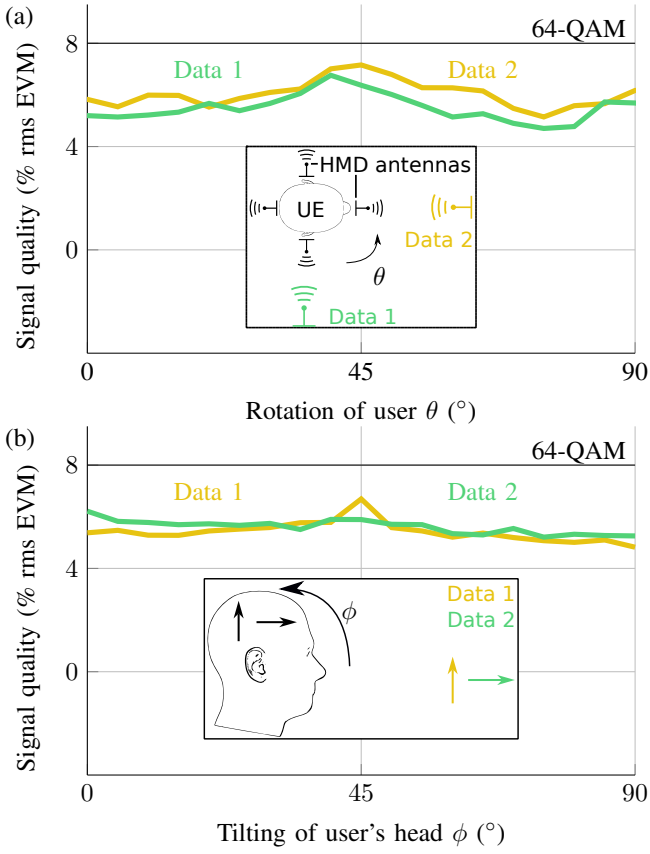

Figure 5.12: Two synchronized RAUs, simultaneously transmitting two distinct data streams, enables doubling the throughput by exploiting distributed MIMO (DMIMO) techniques, guaranteeing a reliable 24 Gbps wireless link even when rotating (a) and tilting (b) the user's head.

the path between a specific RAU and the UE, the system can seamlessly switch to the RAU offering the best link quality, a strategy previously explored in [5]. Moreover, data throughput can be further increased, as described in the next section.

5.4.2 Increasing Data Throughput

The macro diversity provided by strategically distributing RAUs in a DAS approach also allows leveraging DMIMO techniques to simultaneously increase reliability and throughput. Figure 5.12 shows the received signal quality when two data streams are simultaneously transmitted by two spatially separated RAUs to a rotating HMD UE (a) and by two orthogonally-polarized arrays co-located at RAU 1 to a HMD UE being tilted over an angle ϕ (b). In both cases, the use of DMIMO post-processing techniques (as in [5]) doubles the channel capacity and, hence, data rate to 24 Gbps, and this independent of the user's head rotation and tilt.

5.5 Conclusion

MmWave-over-fiber distributed antenna systems relying on air-filled substrate-integrated waveguide (AFSIW) antennas are proposed to realize reliable high-datarate links in challenging indoor environments where frequent line-of-sight blocking occurs. To back up this claim, the severity of the blockage problem was first studied in literature, showing blockage losses up to 30 dB in the n257, n258 and n261 5G frequency bands and up to 40 dB in the n263 band. Several solutions to these problems were then compared. It was found that a distributed approach overcomes the blockage problems while also keeping background exposure low. Different antenna topologies were then compared based on both bio-electromagnetic and communication criteria. It was found that AFSIW antennas are promising candidates for deployment in body-centric communication since they offer a practical antenna solution with low losses and a broad bandwidth, while also keeping the absorbed power density in the human body low, even in close proximity. Finally, a practical mmWave DAS with AFSIW antennas on a headmount user equipment was studied experimentally to demonstrate reliable high-data rate communication. The system was able to sustain a 12 Gbps link when the user turns or tilts its head. Using DMIMO in the system, the data rate was even increased to 24 Gbps.

References

[1] J. A. Zhang, M. L. Rahman, K. Wu, *et al.*, "Enabling joint communication and radar sensing in mobile networks—A survey", *IEEE Communications Surveys & Tutorials*, vol. 24, no. 1, pp. 306–345, 2021.

[2] M. Bennis, M. Debbah, and H. V. Poor, "Ultrareliable and low-latency wireless communication: Tail, risk, and scale", *Proceedings of the IEEE*, vol. 106, no. 10, pp. 1834–1853, 2018.

[3] M. Giordani, M. Polese, M. Mezzavilla, S. Rangan, and M. Zorzi, "Toward 6G networks: Use cases and technologies", *IEEE communications magazine*, vol. 58, no. 3, pp. 55–61, 2020.

[4] Q. Wu, S. Zhang, B. Zheng, C. You, and R. Zhang, "Intelligent reflecting surface-aided wireless communications: A tutorial", *IEEE transactions on communications*, vol. 69, no. 5, pp. 3313–3351, 2021.

[5] A. Moerman, J. Van Kerrebrouck, O. Caytan, *et al.*, "Beyond 5G Without Obstacles: mmWave-over-Fiber Distributed Antenna Systems", *IEEE Communications Magazine*, vol. 60, no. 1, pp. 27–33, 2022.

[6] S. Hu, F. Rusek, and O. Edfors, "Beyond Massive MIMO: The Potential of Data Transmission With Large Intelligent Surfaces", *IEEE Trans. Signal Process.*, vol. 66, no. 10, pp. 2746–2758, 2018.

[7] S. Hu, F. Rusek, and O. Edfors, "Beyond massive MIMO: The potential of positioning with large intelligent surfaces", *IEEE Transactions on Signal Processing*, vol. 66, no. 7, pp. 1761–1774, 2018.

[8] H. Herssens, W. Joseph, and A. Thielens, "A Survey of On-Body Antenna Arrays: Future improvements, new designs, and lessons learned [Bioelectromagnetics]", *IEEE Antennas and Propagation Magazine*, vol. 65, no. 3, pp. 86–96, 2023.

[9] A. Pellegrini, A. Brizzi, L. Zhang, *et al.*, "Antennas and Propagation for Body-Centric Wireless Communications at Millimeter-Wave Frequencies: A Review [Wireless Corner]", *IEEE Antennas and Propagation Magazine*, vol. 55, no. 4, pp. 262–287, 2013.

[10] B. Xu, K. Zhao, Z. Ying, D. Sjöberg, W. He, and S. He, "Analysis of impacts of expected RF EMF exposure restrictions on peak EIRP of 5G user equipment at 28 GHz and 39 GHz bands", *IEEE Access*, vol. 7, pp. 20 996–21 005, 2019.

[11] W. He, B. Xu, Y. Yao, D. Colombi, Z. Ying, and S. He, "Implications of incident power density limits on power and EIRP levels of 5G millimeter-wave user equipment", *IEEE Access*, vol. 8, pp. 148 214–148 225, 2020.

[12] X. Zhao, Q. Wang, S. Li, *et al.*, "Attenuation by human bodies at 26-and 39.5-GHz millimeter wavebands", *IEEE Antennas and Wireless Propagation Letters*, vol. 16, pp. 1229–1232, 2016.

[13] R. Schulpen, L. A. Bronckers, A. B. Smolders, and U. Johannsen, "Impact of Human Blockage on Dynamic Indoor Multipath Channels at 27 GHz", *IEEE Transactions on Antennas and Propagation*, vol. 70, no. 9, pp. 8291–8303, 2022.

[14] U. T. Virk and K. Haneda, "Modeling human blockage at 5G millimeter-wave frequencies", *IEEE Transactions on Antennas and Propagation*, vol. 68, no. 3, pp. 2256–2266, 2019.

[15] C. Ballesteros, L. Vähä-Savo, K. Haneda, C. Icheln, J. Romeu, and L. Jofre, "Assessment of mmWave handset arrays in the presence of the user body", *IEEE Antennas and Wireless Propagation Letters*, vol. 20, no. 9, pp. 1736–1740, 2021.

[16] D. Prado-Alvarez, S. Inca, D. Martín-Sacristán, and J. F. Monserrat, "Millimeter-wave human blockage model enhancements for directional antennas and multiple blockers", *IEEE Communications Letters*, vol. 25, no. 9, pp. 2776–2780, 2021.

[17] C. Slezak and S. Rangan, "Measurement-Based Indoor Millimeter Wave Blockage Models", *IEEE Transactions on Wireless Communications*, vol. 21, no. 8, pp. 6774–6786, 2022.

[18] L. A. Fierro, E. C. Maggi, A. A. Vazquez, and D. Schkolnik, "Empirical results for human-induced shadowing events for indoor 60 GHz wireless links", *IEEE Access*, vol. 8, pp. 44 522–44 533, 2020.

[19] C.-X. Wang, J. Bian, J. Sun, W. Zhang, and M. Zhang, "A survey of 5G channel measurements and models", *IEEE Commun. Surveys Tuts.*, vol. 20, no. 4, pp. 3142–3168, Aug. 2018.

[20] J. Huang, C.-X. Wang, R. Feng, J. Sun, W. Zhang, and Y. Yang, "Multi-frequency mmWave massive MIMO channel measurements and characterization for 5G wireless communication systems", *IEEE journal on selected areas in communications*, vol. 35, no. 7, pp. 1591–1605, 2017.

[21] 3GPP, “Study on channel model for frequencies from 0.5 to 100 GHz”, 3rd Generation Partnership Project (3GPP), Technical Specification (TS) 38.901, Jan. 2024, Version 17.1.0.

[22] J. Lee, M.-D. Kim, and J.-J. Park, “Empirical investigation of array beamforming effects on received power and delay spread characteristics based on 159 ghz measurements”, *IEEE Wireless Communications Letters*, 2024.

[23] F. Firyaguna, J. Kibilda, and N. Marchetti, “Application of flexible numerology to blockage mitigation in 5G-mmWave networks”, in *2019 IEEE Global Communications Conference (GLOBECOM)*, IEEE, 2019, pp. 1–6.

[24] I. K. Jain, R. Kumar, and S. Panwar, “Driven by capacity or blockage? A millimeter wave blockage analysis”, in *2018 30th International Teletraffic Congress (ITC 30)*, IEEE, vol. 1, 2018, pp. 153–159.

[25] M. Nitta, H. Suganuma, and F. Maehara, “Blockage mitigation method employing antenna height and user position in millimeter-wave communications”, in *2021 International Symposium on Intelligent Signal Processing and Communication Systems (ISPACS)*, IEEE, 2021, pp. 1–2.

[26] J. Zhang, S. Chen, Y. Lin, J. Zheng, B. Ai, and L. Hanzo, “Cell-free massive MIMO: A new next-generation paradigm”, *IEEE Access*, vol. 7, pp. 99 878–99 888, 2019.

[27] H. A. Ammar, R. Adve, S. Shahbazpanahi, G. Boudreau, and K. V. Srinivas, “User-centric cell-free massive MIMO networks: A survey of opportunities, challenges and solutions”, *IEEE Communications Surveys & Tutorials*, vol. 24, no. 1, pp. 611–652, 2021.

[28] E. Björnson, Ö. Özdogan, and E. G. Larsson, “Reconfigurable intelligent surfaces: Three myths and two critical questions”, *IEEE Commun. Mag.*, vol. 58, no. 12, pp. 90–96, Dec. 2020.

[29] H. Ibraiwish, A. Elzanaty, Y. H. Al-Badarneh, and M.-S. Alouini, “EMF-aware cellular networks in RIS-assisted environments”, *IEEE Communications Letters*, vol. 26, no. 1, pp. 123–127, 2021.

[30] ETSI, *ETSI GR RIS 003: Reconfigurable Intelligent Surfaces (RIS); Communication Models, Channel Models, Channel Estimation and Evaluation Methodology - v1.1.1*, Jun. 2023 Accessed: May. 2024. [Online]. Available: `https://www.etsi.org/deliver/etsi_gr/RIS/001_099/003/`.

[31] A. Minasian, R. S. Adve, S. Shahbazpanahi, and G. Boudreau, "On RRH placement for multi-user distributed massive MIMO systems", *IEEE Access*, vol. 6, pp. 70 597–70 614, 2018.

[32] S. Shikhantsov, A. Thielens, G. Vermeeren, P. Demeester, L. Martens, and W. Joseph, "Numerical Assessment of Human EMF Exposure to Collocated and Distributed Massive MIMO Deployments in an Industrial Indoor Environment", *IEEE Transactions on Electromagnetic Compatibility*, 2023.

[33] L. Breyne, G. Torfs, X. Yin, P. Demeester, and J. Bauwelinck, "Comparison Between Analog Radio-Over-Fiber and Sigma Delta Modulated Radio-Over-Fiber", *IEEE Photon. Technol. Lett.*, vol. 29, no. 21, pp. 1808–1811, Nov. 2017.

[34] A. Moerman, O. Caytan, L. Van Messem, *et al.*, "System-level model for mmwave-over-fiber distributed antenna systems", in *IEEE PAST*, Waltham, MA, USA, 2022, pp. 1–4.

[35] K. Li, S. Kodera, D. Poljak, *et al.*, "Calculated epithelial/absorbed power density for exposure from antennas at 10–90 GHz: Intercomparison study using a planar skin model", *IEEE access*, vol. 11, pp. 7420–7435, 2023.

[36] W. He, B. Xu, M. Gustafsson, Z. Ying, and S. He, "RF compliance study of temperature elevation in human head model around 28 GHz for 5G user equipment application: Simulation analysis", *IEEE Access*, vol. 6, pp. 830–838, 2017.

[37] C. Leduc and M. Zhadobov, "Impact of antenna topology and feeding technique on coupling with human body: application to 60-GHz antenna arrays", *IEEE Transactions on Antennas and Propagation*, vol. 65, no. 12, pp. 6779–6787, 2017.

[38] G.-J. Gordebeke, S. Lemey, O. Caytan, *et al.*, "Time-Domain-Optimized Antenna Array for High-Precision IR-UWB Localization in Harsh Urban Shipping Environments", *IEEE Sensors Journal*, vol. 24, no. 5, pp. 5561–5577, 2024.

[39] F. Parment, A. Ghiotto, T.-P. Vuong, J.-M. Duchamp, and K. Wu, "Air-filled substrate integrated waveguide for low-loss and high power-handling millimeter-wave substrate integrated circuits", *IEEE transactions on microwave theory and techniques*, vol. 63, no. 4, pp. 1228–1238, 2015.

[40] A. Belenguer, H. Esteban, and V. E. Boria, "Novel empty substrate integrated waveguide for high-performance microwave integrated circuits", *IEEE transactions on microwave theory and techniques*, vol. 62, no. 4, pp. 832–839, 2014.

[41] I. Lima de Paula, S. Lemey, D. Bosman, *et al.*, "Cost-effective high-performance air-filled SIW antenna array for the global 5G 26 GHz and 28 GHz bands", *IEEE Antennas Wireless Propag. Lett.*, vol. 20, no. 2, pp. 194–198, Feb. 2021.

[42] I. Lima de Paula, L. Bogaert, O. Caytan, *et al.*, "Air-Filled SIW Remote Antenna Unit With True Time Delay Optical Beamforming for mmWave-Over-Fiber Systems", *Journal of Lightwave Technology*, vol. 40, no. 20, pp. 6961–6975, 2022.

[43] "IEEE Standard for Definitions of Terms for Antennas", *IEEE Std 145-2013 (Revision of IEEE Std 145-1993)*, pp. 1–50, 2014.

[44] O. Caytan, I. L. De Paula, L. Bogaert, *et al.*, "Co-design strategies for afsiw-based remote antenna units for rfof", in *2023 17th European Conference on Antennas and Propagation (EuCAP)*, 2023, pp. 1–5.

[45] I. C. on Non-Ionizing Radiation Protection *et al.*, "Guidelines for limiting exposure to electromagnetic fields (100 kHz to 300 GHz)", *Health physics*, vol. 118, no. 5, pp. 483–524, 2020.

[46] G. Sacco, D. Nikolayev, R. Sauleau, and M. Zhadobov, "Antenna/human body coupling in 5G millimeter-wave bands: Do age and clothing matter?", *IEEE Journal of Microwaves*, vol. 1, no. 2, pp. 593–600, 2021.

[47] O. P. Gandhi and A. Riazi, "Absorption of millimeter waves by human beings and its biological implications", *IEEE Transactions on microwave theory and techniques*, vol. 34, no. 2, pp. 228–235, 1986.

[48] G. Sacco, Z. Haider, and M. Zhadobov, "Exposure levels induced in curved body parts at mmWaves", *IEEE Journal of Electromagnetics, RF and Microwaves in Medicine and Biology*, vol. 6, no. 3, pp. 413–419, 2022.

[49] L. Van Messem, A. Moerman, O. Caytan, *et al.*, "A 4 × 4 Millimeterwave-Frequency Butler Matrix in Grounded Co-Planar Waveguide Technology for Compact Integration With 5G Antenna Arrays", *IEEE Transactions on Microwave Theory and Techniques*, vol. 71, no. 1, pp. 122–134, 2023.

[50] 3GPP, *NR; User Equipment (UE) radio transmission and reception; Part 2: Range 2 Standalone - Release 15 - v38.101-2*, Accessed: Mar. 2024. [Online]. Available: https://www.3gpp.org/dynareport/38-series.htm.

[51] M. R. M. Hashemi, A. C. Fikes, M. Gal-Katziri, *et al.*, "A flexible phased array system with low areal mass density", *Nature electronics*, vol. 2, no. 5, pp. 195–205, 2019.

[52] M. Gal-Katziri, A. Fikes, and A. Hajimiri, "Flexible active antenna arrays", *npj Flexible Electronics*, vol. 6, no. 1, p. 85, 2022.

[53] speag, *HEAD-P10 and mmW-HEAD-P10*, Jan. 2024. [Online]. Available: https://speag.swiss/products/em-phantoms/phantoms-3/head-p10/.

[54] A. Moerman, O. Caytan, L. Van Messem, *et al.*, "System-Level Simulation Suite for the Design of mmWave-Over-Fiber-Based Distributed Antenna Systems", *IEEE Transactions on Microwave Theory and Techniques*, vol. 71, no. 12, pp. 5082–5094, 2023.

[55] 3GPP, *LTE; Evolved Universal Terrestrial Radio Access (E-UTRA); Base Station (BS) radio transmission and reception - Release 15 - v 15.3.0*, Tech. Rep. TR 36.104, Jan. 2021. [Online]. Available: https://www.3gpp.org/dynareport/36-series.htm.

6

Conclusions and Outlook

In this dissertation, we have explored the next generation of wireless networks, focusing on the Internet of Everything (IoE) and its transformative potential. The IoE envisions a world where diverse devices and systems communicate seamlessly, necessitating wireless networks that support multi-Gbps data speeds while meeting stringent reliability and latency requirements. The evolution beyond the fifth-generation (B5G) wireless network aims to enable innovative applications centered around multi-sensory feedback, such as holographic telepresence, augmented/virtual/extended reality with haptic feedback, and Industry 5.0 factories and machinery.

Several key enablers have been proposed in the literature to fully realize these applications. On the one hand, there is a move toward higher mmWave frequency bands with abundant available bandwidth. On the other hand, cell-free MIMO or DMIMO is presented as a technique to further increase wireless reliability and throughput beyond the limits of classic cell densification trends.

This research contributed to bridging the gap between theoretical studies on cell-free MIMO and DMIMO, and the lack of practical mmWave implementations suitable for large-scale deployment. Specifically, we introduced the first implementation of a realistic millimeter-wave (mmWave)-over-fiber distributed antenna system (DAS) capable of delivering multi-Gbps data rates in real-world environments. By employing a photonically-enabled architecture and leveraging air-filled substrate-integrated-waveguide (AFSIW) technology, a cost-effective and efficient solution is proposed that paves the way for mass deployment.

Our work demonstrated the system's effectiveness in various settings, ranging from well-controlled free-space conditions in an anechoic chamber to challenging Industry 5.0 environments. It was shown that the inherent

synchronization of the mmWave-over-fiber architecture enables DMIMO techniques, significantly improving data throughput and reliability, even in complex industrial scenarios, where line-of-sight blocking frequently occurs.

Additionally, we developed a comprehensive system-level framework for the optimization of mmWave-over-fiber DAS in an efficient manner, as practical deployment and optimization can be time consuming. This framework integrated commercial software with custom-developed code to accurately model and predict signal quality, including scenarios with various channel models and inter-user interference. A measurement campaign using a Butler matrix-based RAU validated the framework's predictions.

Finally, the dissertation addressed the bioelectromagnetic implications of deploying distributed antenna systems, particularly for AR and VR applications involving head-mounted devices. We compared DMIMO systems with emerging technologies such as reconfigurable and large intelligent surfaces, demonstrating that distributed systems offer superior spectral efficiency, lower exposure, and better energy usage. Our holistic approach, combining bioelectromagnetic and communication figures-of-merit, identified AFSIW topologies as particularly advantageous, offering high platform independence and low absorbed power density near the human body at the UE.

As demonstrated during this doctoral thesis, several critical challenges have been addressed to realize and roll out mmWave-over-fiber distributed antenna systems for next-generation communication systems. There are, however, a myriad of remaining challenges and opportunities waiting for further investigation. Below, a prospect is given into interesting opportunities for the next wave of innovations in microwave and RF design.

First, this PhD research primarily focused on the lower range of the FR2 frequency bands. While the inclusion of upper FR2 bands (centered around 47 GHz and 60 GHz) and sub-THz frequencies, such as the D band (110 GHz–170 GHz), in future 6G standards remains uncertain due to challenges like reduced output power and higher noise figures in active electronics, there is significant potential to scale mmWave-over-fiber distributed antenna systems to these frequencies, enabling future applications that demand extreme bandwidths. Both the FR2 and the higher mmWave frequency bands call for novel opto-electronic components, but the approach to realize a DAS in each frequency band differs. For the upper FR2 frequency bands, on the one hand, a similar architecture to that developed in this thesis can be employed, but there is a pressing need for optical modulators and photodetectors with sufficiently large RF bandwidths. These components

are not yet commercially available and require a multidisciplinary approach, combining expertise from photonics and microwave engineering. Designing highly efficient components, preferably co-designed with drivers and low-noise amplifiers, remains a significant challenge. However, this approach has its limits. Higher frequency bands, on the other hand, necessitate a different architecture involving photomixing, which relaxes the bandwidth constraints on the optical modulator. This architecture also requires custom microwave photonic designs to generate two frequency-locked lasers and the necessary filters to produce the beat frequency at the photodetector.

Another interesting path to extend the DAS functionality is the ability to operate simultaneously in multiple frequency bands. This area offers several promising research directions. Given that the mmWave-over-fiber link is intrinsically non-linear, careful consideration must be devoted to which combination of frequency bands minimizes and preferably prevents in-band mixing products. This also presents an interesting challenge for front-end design, where various approaches should be compared to achieve an efficient solution. Depending on the chosen frequency bands and desired specifications, dual-band antennas may be viable, or a highly efficient diplexer could be designed and incorporated to drive two separate (preferably steerable) antenna arrays.

Furthermore, full-duplex systems have long been an area of interest owing to their potential to double the channel capacity. Extending the DAS to operate in a full-duplex way is possible when focusing on interference cancellation in signal processing and in different analog parts of the link and it would benefit the data rates of the wireless system. Adapting sensing in a distributed antenna system improves angular resolution. Moreover, joint communication and sensing (JCAS) has garnered considerable research interest in recent years. In a DAS, integrating JCAS could enable applications such as vital sign monitoring and positioning, which could significantly aid beamforming algorithms. To achieve this, some present challenges ranging from design of new algorithms and novel signal processing techniques to the development of dedicated architectures and the design of advanced antenna front-ends remain.

Beyond these enhancements to distributed antenna systems, other exciting opportunities for exploration remain. Chapter 2 briefly touched on the potential of machine learning at every layer of the B5G wireless communication stack. In large-scale deployments of distributed or cell-free MIMO systems, massive amounts of data must be processed to optimize the

signal-to-interference-and-noise ratio for high-throughput links targeting a massive number of users. Exploring machine learning to assist with this complex equalization problem could be highly beneficial. In general, these surrogate models need vast amounts of data to be trained and the system-level framework from Chapter 4 could, in time, help to generate the data for various wireless channel states.

Moreover, the newly proposed metric for evaluating mmWave antenna topologies in terms of bioelectromagnetic and communication specifications opens up opportunities to conceive novel high-performance wearable mmWave multi-antenna systems. The AFSIW topology with a high front-to-back ratio that performed best in Chapter 5, still had an increase absorbed power ratio for very low antenna-to-skin distances due to its feedline and the transition from grounded coplanar waveguide to the SIW cavity. This raises the question of how much improvement could be achieved with a redesigned antenna featuring a buried feed, such as a substrate integrated coaxial line (SICL). Additionally, all single-element topologies were studied, but it would be interesting to compare these results with antenna arrays based on these topologies and evaluate their performance using the newly proposed metric.

Finally, while this research primarily addressed challenges in the lower physical layer (PHY), further efforts should be dedicated to studying the higher layers of a mmWave-over-fiber distributed antenna system to tackle challenges such as user mobility, dynamic blockages, and fluctuations in the number of active users. Although this work mainly utilized single-element antennas and corporate-fed antenna arrays, future deployments will rely on steerable antenna arrays at both the RAU and the UE side to further mitigate larger path losses and interference. However, these arrays require efficient (distributed) beamforming design within the DAS. Additionally, developing algorithms for optimal RAU (beam) and antenna (beam) selection at the UE will be essential to ensuring the best link quality. Furthermore, further research into resource allocation and distributed MIMO algorithms could significantly advance the practical deployment of these systems.